UC Berkeley
UC Berkeley Electronic Theses and Dissertations

Title
Simulating the Inelastic Seismic Behavior of Steel Braced Frames Including the Effects of Low-Cycle Fatigue

Permalink
https://escholarship.org/uc/item/3dr054cx

Author
Huang, Yuli

Publication Date
2009

Peer reviewed|Thesis/dissertation

eScholarship.org Powered by the California Digital Library
University of California

Simulating the Inelastic Seismic Behavior of Steel Braced Frames Including the Effects of Low-Cycle Fatigue

by

Yuli Huang

B.Eng. (Tsinghua University) 2002
M.Eng. (Tsinghua University) 2005

A dissertation submitted in partial satisfaction of the
requirements for the degree of
Doctor of Philosophy

in

Engineering — Civil and Environmental Engineering

in the

GRADUATE DIVISION
of the
UNIVERSITY OF CALIFORNIA, BERKELEY

Committee in charge:
Professor Stephen A. Mahin, Chair
Professor Božidar Stojadinović
Professor Jon Wilkening

Fall 2009

Simulating the Inelastic Seismic Behavior of Steel Braced Frames Including the Effects of Low-Cycle Fatigue

Copyright 2009

by

Yuli Huang

Abstract

Simulating the Inelastic Seismic Behavior of Steel Braced Frames

Including the Effects of Low-Cycle Fatigue

by

Yuli Huang

Doctor of Philosophy in Engineering — Civil and Environmental Engineering

University of California, Berkeley

Professor Stephen A. Mahin, Chair

The research in this dissertation describes simulations of the inelastic seismic behavior of steel braced frames including the effects of low-cycle fatigue. Various types of nonlinear behavior are considered: material inelasticity, low-cycle fatigue, and local and global geometric nonlinearities. The effects of suddenly started, quasi-brittle fracture are not considered herein. For steel braced frames, braces, columns, beams, and connections subjected to significant axial loads and deformations, as well as bending moments and shear. Under these complex-loading conditions, a wide variety of behavior mechanisms and failure modes may occur for each type of member and connection. Thus, numerical models that assess the initiation and propagation of failure during cyclic loading need to account for multi-axial states of material nonlinearity,

local and global buckling, and the exhaustion of the ability of the material to deform inelastically caused by low-cycle fatigue.

Following a review of existing material models for simulating structural steel deterioration, a series of investigations are conducted using finite element modeling techniques. Finite element methods can directly account for complex states of stress and changes in deformed shape. And material models are critical for constitutive behavior at integration points of the finite element models. However, available material models tend to emphasize behavior associated with ideal ductile response or with failure occurring under monotonic loading conditions (*e.g.,* during metal-forming processes or vehicle collision). These models are not suitable for progressive collapse analysis under cyclic loading where the consequence of this adverse behavior on the subsequent response or integrity of the structure is of interest.

Therefore, a new, numerically efficient continuum damage mechanics material model capable of simulating inelastic behavior and deterioration of mechanical properties because of low-cycle fatigue has been devised and implemented in a finite element software LS-DYNA (LSTC 2007). Computational results obtained with this new material model correlate well with test results for several beam-to-column connections, individual braces, and braced frame subassemblies. These applications of the finite element model to realistic cases involving progressive collapse illustrate the importance of material deterioration and rupture. Unfortunately, the ability of the material model to predict ultimate behavior depends heavily on the material model-

ing properties specified. Recommendations for characterizing material properties for these types of analysis are developed and presented.

A series of analyses are presented that evaluate and refine several requirements for detailing and analyzing special concentrically braced steel frame buildings, demonstrating that the fatigue life capacity of braces is heavily dependent on width-thickness ratios and deformation histories. Member slenderness ratios are shown to have negligible effect on fatigue life capacity. Therefore, recommendations are presented for developing fatigue life demand or loading protocols for use in numerical and experimental investigations. Next, damage evolution in gusseted beam-to-column connections is evaluated and compared for different connection details, and improved connection details are recommended to reduce the damage accumulation. The position of lateral bracing members for beams in V-type and inverted V-type braced frames are also examined. More appropriate positions and methods to compensate for problems detected for currently recommended lateral bracing member positions are suggested and evaluated. Finally, for low-rise braced frames that respond inelastically during strong earthquake ground shaking, an alterative method to estimate interstory drift demands is suggested based on the Modal Pushover Analysis procedure.

Professor Stephen A. Mahin
Dissertation Committee Chair

To my parents and grandparents.

Contents

List of Figures

List of Tables

Acknowledgments

First and foremost, the author wishes to express his sincere gratitude to Professor Stephen Mahin for his invaluable guidance, deep insight, and brilliant ideas during the course of this research. The author wishes to thank Professors Božidar Stojadinović and Jon Wilkening for serving as members of the dissertation committee and for their effort reading and revising this dissertation, Professors Anil Chopra, Filippos Filippou, and Tarek Zohdi for serving as members of the qualifying exam committee. The author also wishes to thank all professors for their enlightenment in the courses taken at the University of California at Berkeley.

The work performed in this investigation was funded in part by the Consortium of Universities for Research in Earthquake Engineering, as part of the CUREE-Kajima Joint Research Program on Earthquake Engineering. The author gratefully acknowledges the funding for this project from the Kajima Corporation, and the leadership of the Joint Oversight Committee in helping define the direction and scope of the research efforts undertaken. Funding was also provided by the National Science Foundation under Grants CMS-0600625 and CMS-0619161, and by the University of California at Berkeley through the Byron and Elvira Nishkian Chair Professorship of Structural Engineering.

The author wishes to acknowledge the collaboration of Dr. Yoshikazu Sawamoto of Kajima Corporation, Japan on this work through sharing of test data, providing advice, and a thorough review of the models and results obtained. The assistance of

Dr. Patxi Uriz in providing data on braced frames and helping interpret prior test results is gratefully acknowledged. The author appreciates the assistance of Dr. John Hallquist, Dr. Leonard Schwer, and Mr. Jim Day of Livermore Software Technology Corporation, and Mr. Michael Willford, Mr. Eric Ko, and Ms. Caroline Field of Arup. Ms. Claire Johnson skillfully proofread the manuscript. Many thanks to her.

The findings, conclusions and observations contained herein are those of the author. They do not necessarily represent the policy, recommendations, or findings of the Consortium of Universities for Research in Earthquake Engineering, the Kajima Corporation, the National Science Foundation, or the University of California at Berkeley.

Preface

Part of the research presented in this dissertation was undertaken as a sub-project of the Phase VI CUREE/Kajima Collaborative Research Project on factors leading to the progressive collapse of structures. In this research, the cyclic behavior and modeling of steel structural elements and connections, with emphasis on those subjected to high axial loads, are examined as they approach and reach failure. This work complements parallel work at Stanford University under the supervision of Professor H. Krawinkler on steel and reinforced concrete elements and connections where axial loads do not dominate the expected mode of behavior (Lignos and Krawinkler, 2007), and work at the University of Buffalo under the supervision of Professor A. Reinhorn on large displacement analysis of structural systems (Sivaselvan *et al.,* 2007).

Chapter 1

Introduction

1.1 Background

Engineers frequently use various types of computer analysis to assess the safety of engineered structures. Simplified analysis methods are often employed in the design of standard structures. Modeling guidelines and acceptance criteria used in conjunction with such simplified methods are intended to provide acceptable conservatism relative to the safety and serviceability of the structure. In some cases, however, more refined analysis methods are required. Such refined analysis is used in situations where:

1. Existing structures are to be evaluated for loading or environmental conditions more severe than initially considered in design. Simplified analysis methods not directly related to the expected behavior of as-built structural elements may not be able to quantify adequately the true ability of a structure to withstand

more severe loading conditions, raising questions regarding the need to retrofit or upgrade a structure for the new criteria.

2. An existing structure is to be architecturally or functionally remodeled, requiring removal or shifting of structural members, changing the overall size of the building, or altering the type and configuration of the structural system.

3. New structural systems employ unusual features, details or configurations where simplified analysis methods may not be adequate or the incorporation of these new structural elements introduce significant uncertainties regarding the adequacy of the proposed design. Modern architecture often does not conform to past practices regarding gravity and lateral load resisting systems and tends to incorporate unusual details or member proportions.

4. A precise evaluation of the safety or performance of a structure is required for hypothetical man-made or natural hazards. Today, various stakeholders (owners, occupants, government officials, insurance companies, financial institutions, *etc.*) are requesting assessment of the safety and probable losses that might occur as a result of a variety of natural and man-made hazards.

In cases such as these, commonly used, simplified analysis methods may not be able to give a true picture of actual damage or losses. Thus, a more complex analysis is needed that can simulate the various behavior modes that can occur at the element and structure level and track the evolution of damage from onset to eventual member

and structural failure. Because several modes of behavior can potentially occur in all members and connections, the models must simulate to a fair degree of accuracy those modes, and correctly identify those modes that control behavior and ultimate failure.

Although this work focusses on the behavior of components, it is recognized that the local failure of a part of one member may not lead to the loss of structural integrity of that member or of the structure as a whole. Where collapse does occur, it may involve one or several local regions of the structure. In some cases, the failure of one element may be critical to the overall stability of the structure. The complete structure, or a substantial portion of the structure above (and below) the element or region that initially fails, may collapse. Situations where a local failure leads to disproportionate damage or collapse of large portions of a structure are known as "progressive collapse".

Predicting the onset of damage within a large and complex structure, and the consequence of such local damage on other elements and the structure as a whole, requires analytical models that simulate to a fair degree of accuracy the behavior of structural elements and systems undergoing large inelastic deformations. As such, available analysis procedures and models will be reviewed and evaluated to assess their ability to predict the behavior and failure of elements and structural systems.

For structures subjected to earthquakes, material models need to account for cyclic plasticity, including deterioration and eventual failure because of low-cycle fatigue.

The deterioration of a member may alter not only the distribution of forces and damage within a structural system, but also the response history. Because response history influences the degree of deterioration, accurate material and component models that predict the response of structures subjected to severe earthquake shaking or other transient dynamic excitations are critical.

In seismic-resistant design, equivalent static or dynamic analysis based on elastic representations of member properties are commonly employed, even though significant inelastic action is expected. Engineers are increasingly interested in predicting inelastic response using nonlinear static or nonlinear dynamic analysis procedures. For nonlinear static methods, a realistic structural model is subjected to a fixed distribution of lateral forces, which monotonically increase in intensity with time. Such static inelastic "pushover" analyses, fairly common in design practice, provide a design engineer with a general indication of the distribution of inelastic deformations (and internal forces) within the structure, the global load capacity of the structure, and the lateral displacement at which certain key events occur (initial yielding, initiation of member failure, loss of global stability, *etc.*). Nonlinear dynamic time history analysis are computationally more demanding, but provide a more realistic prediction of the response quantities of interest.

Nonlinear time history analysis of structures during design usually assume ideal ductile member behavior. The computer model estimates global response quantities (interstory drift, story shears, *etc.*) and locally required plastic deformation demands

(plastic hinge rotations, plastic strains, *etc.*) based on ideal ductile behavior. Although this assumption is quite broad, it is generally accepted because the elements and connections can subsequently be detailed to develop predicted inelastic demands, or if the resulting details, are objectionable or the structure does not meet acceptance criteria for the overall system behavior, the configuration, proportions and details of the structural system and elements can be changed.

Members and connections in new and especially existing structures have finite ductility capacities, however, and because a certain degree of deterioration of properties might be expected generally, infinitely ductile models may not be adequate for seismic or other abnormal loading conditions, as inelastic demands will likely lead to deterioration and possible failure of members. These weakened members will, in turn, influence dynamic response and overall system stability.

In order to assess behavior of an element or structure as it approaches failure under earthquake or other excitations, several types of nonlinear behavior need to be considered. These relate to material inelasticity, fracture, low-cycle fatigue, and local and global geometric nonlinearities.

Herein, the effects of suddenly started, quasi-brittle fracture are not considered. Where issues of fracture mechanics need to be taken into account, a large number of small sized finite elements are required. Such analysis models and methods do not lend themselves to the analysis of a complete structural system under dynamic loading. Thus, it is assumed herein that a separate fracture-mechanics-based analysis

should be carried out on individual fracture critical regions. Where behavior is found to be vulnerable to quasi-brittle or ductile fracture, this report assumes that: (1) a simplified material or damage model is devised that would mimic the mode of fracture detected; or (2) problematic details would be changed to mitigate the vulnerability. Regardless, the research presented herein includes scenarios where members rupture because of the materials reaching and exceeding their ability to develop further inelastic deformations, either under monotonic or cyclic loading. Such ruptures may appear similar to and have similar consequences as fracture, but they are different physical phenomena and require different analysis approaches.

Steel braced frames are the focus of this investigation is steel braced frames. For such structures (see the frame designated as a braced frame in Figure 1.1), lateral load resistance is, in large part, because of the braced frame acting as a vertically oriented truss. The braces, columns, beams, and connections are subjected to significant axial loads. Braces are generally expected to respond in the inelastic range during moderate and severe earthquakes. At displacement levels associated with brace yielding or buckling, significant bending and shear demands can also develop in all members and connections. Under these complex-loading conditions, a wide variety of behavior mechanisms and failure modes must be taken into account for each type member and connection. The particular behavior that occurs and the consequence of its occurrence depend on material properties, member proportions, local details, and the applied loading or deformations (which will depend not only on the externally applied

loads, but also on the behavior of adjacent members and connections). Thus, models that assess the potential for failure to propagate throughout the structure need to account for multi-axial states of material nonlinearity, local and global buckling, and low-cycle fatigue.

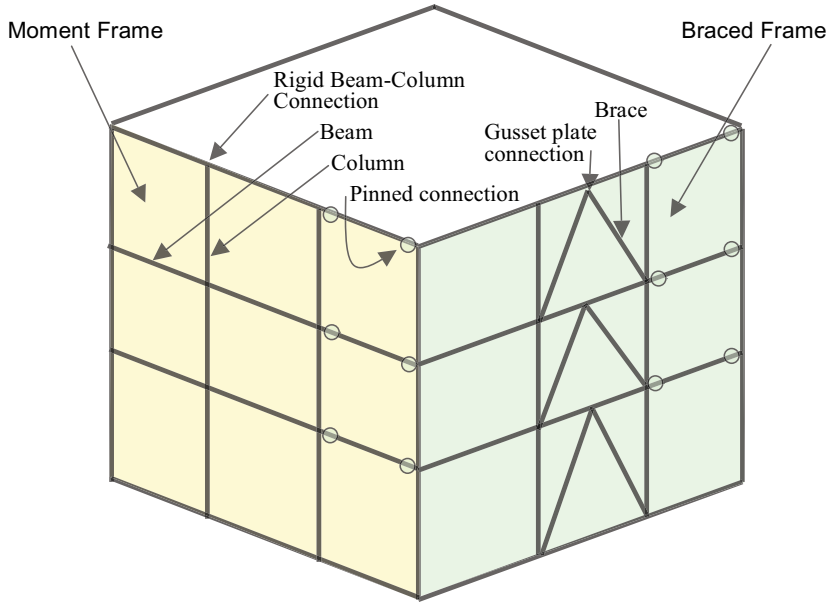

Figure 1.1: Schematic steel building comprising braced and moment-resisting frames

This investigation considers elements that make up typical concentrically braced steel frames. These include conventional bracing members that may buckle laterally and locally during loading in compression. Because braced frames are often used as part of a dual system, some attention will be given to the modeling of conventional steel beam-to-column connections. Additional Issues related to modeling and analysis in moment-resisting frame components and connections are the focus of a parallel study carried out at Stanford University (Lignos and Krawinkler, 2007).

Generally speaking, three basic approaches will be taken to modeling structural members of the type examined in this report. These are referred to herein as: (1) phenomenological models; (2) physical theory models; and (3) finite element models.

- **Phenomenological Models.** — Phenomenological models use a simplified physical representation of the member in question. For example, a phenomenological model for a brace usually consists of a simple uniaxial, pin ended truss element with a hysteretic axial force-axial deformation relation defined by a set of generic rules that simply mimic the hysteretic response observed for a brace. The user is responsible for inputting data that enables the generic brace model to represent the particular design being analyzed. In the case of a flexurally dominated beam, a common phenomenological model represents the member as an elastic beam connected at each end to the element's nodes by means of inelastic rotational springs. The rotational springs are simplified in terms of rules that define the hysteretic nature of the moment-rotation characteristics of the plastic hinge region at the end of the member. To model the effects of spalling of concrete, and yielding, buckling, and fracture of steel, more and more complex rules are employed. Generally, these rules do not depend on or attempt to track the actual occurrence of concrete spalling, or steel yielding, buckling, or fracture. These models depend on having an extensive database of experimental results with which the numerical modeling parameters can be identified. Where various behavior modes can occur (bending plus axial buckling, flexure

plus shear, or flexure plus axial loading) the rules become even more complex or are uncoupled, leading to questionable results.

- **Physical Theory Models.** — In many cases, member behavior can be well represented by certain established but simplified rules of mechanics. For example, in a beam with low axial load and shear, plastic hinges occur at easily identified locations. Outside of these regions, this beam will behave in a nearly elastic manner. Within the plastic hinge region, the material may yield and undergo various actions that will affect its properties. In such cases, it may be acceptable to make certain assumptions regarding the distribution of strains across a section and the distribution of curvatures along the member, and track the actual stress-strain history in individual material fibers located across the section. In this way, certain types of physical behavior can be tracked automatically in the analysis, so that complex empirically calibrated rules are not needed. As shown later, this can be applied to a variety of beams, columns, and braces; however, some of the assumptions may not be valid, as the typical fiber-based model incorporates only unidirectional material properties. Consequently, multi-axial stress states and three-dimensional phenomena [such as local buckling, section warping, or distortion (because of shear or torsion), bar pull out, *etc.*] cannot be easily represented.

- **Finite Element Models.** — Although phenomenological and physical the-

ory models described above are special forms of finite elements, the more general case, where a member and structure is divided up into a variety of small shell or solid elements, allows the response of the structure in various modes to be simulated. Such finite element formulations can account for multi-axial stress states, nonlinear material properties, and changes in geometry that occur during loading. Because of the large number of elements and the absence of simplifying assumptions, these models are often computationally expensive and time-consuming to develop and execute; however, they usually produce results close to those expected of real structures. Nevertheless, these models cannot reproduce behavior that is not incorporated in the model (*e.g.,* buckling because of large displacements, material failure, *etc.*), and they put much more reliance on having well-defined multi-directional material property models. As such, careful calibration of these models to test results is needed, and the degree of improvement in response prediction compared to the increased level of effort to perform these models should be carefully considered.

This investigation studies the ability of finite element formulations to simulate accurately the behavior modes of interest in braces, beams, beam-to-column connections and braced frame subassemblies. Compared to phenomenological models, these models require more computational effort, but incorporate more realistic physical representations of members and materials, including the initiation and evolution of damage up to and including complete failure.

1.2 Objectives and scope of research

The objectives of the research presented in this dissertation are as follows: (1) to review available information on the behavior and analysis of members and subassemblies from steel concentrically braced frames where elements are subjected to deterioration; (2) to develop improved numerical models that simulate adequately the behavior of a steel braced frames up to and including failure; (3) to use the improved models to evaluate and refine several requirements for detailing and analyzing special concentrically braced steel frame building.

The remaining chapters of this dissertation derive from the objectives listed above. Chapter 2 reviews existing experimental investigation. Chapter 3 reviews and evaluates material models on structural steel deterioration. Chapter 4 develops a improved cyclic damage plasticity model. Chapter 5 discusses calibration, validation and application of the new damage material model using test results from beam-to-column connections, individual braces, and braced frame subassemblies. Chapter 6 provides studies of steel braced frame behavior, including brace proportions, connection details, lateral bracing for beams, and estimate of interstory drift demands. Concluding remarks and recommendations are discussed in Chapter 7. An appendix includes constraint method developed in this research for pushover analysis and a discussion on instability of Newmark integrator.

Chapter 2

Review of Existing Experimental Investigations

This research is focussed on braces, beams, columns, and connections that are part of braced steel frames, where members are subjected to high axial loads alone or in combination with bending and shear. Some aspects of conventional moment frame construction will also be addressed as these elements may be used in combination with braced frames as a gravity load-resisting system or a backup lateral load-resisting system. Both static and dynamic loading situations will be considered, although, the focus will not be on cases where strain rate effects or where local inertial forces along the length of a member need to be considered. The analysis models considered will include the effects of material inelasticity, local and global buckling, and low-cycle fatigue on the behavior and failure of various elements and structural systems.

Thus experimental results that investigate such behavior are of interest. This chapter reviews experimental data from investigations of conventional braces, gusset plates, braced frame subassemblies, and beam-column connections.

2.1 Investigations of conventional braces

Tremblay (2002) compiled and interpreted the results of more than one hundred tests of steel braces available at that time. These tests include braces fabricated from square hollow structural section (HSS) sections, pipes, wide flange sections, double channels, single and double angles, and structural "T" sections. This compilation does not include recent tests by Tremblay *et al.* (2003), Elchalakani *et al.* (2003), Goggins *et al.* (2005), Yang and Mahin (2005), Fell *et al.* (2006), Han *et al.* (2007), Tremblay *et al.* (2008), and Lehman *et al.* (2008).

Tremblay (2002) used this database to assess several useful engineering relationships used in design. For example, the initial buckling load was compared for the braces in the database to theoretical predictions and to equations included in United States and Canadian building codes, demonstrating that code values are often conservative; they tend to underestimate the buckling capacity of braces, especially for slender braces.

Importantly, Tremblay also examined several other simplified relations that may be used to develop and interpret phenomenological models for braces. For example, relations exist that predict the out-of-plane displacement of buckling braces and the

deterioration of the compressive buckling capacity of braces. For this later case, a relation was developed between the compressive load capacities of braces that have been shortened by a displacement equal to five times the displacement at the onset of buckling. Similar relations were developed for lower and higher normalized displacements.

Tremblay also provided information on the cyclic ductility that a brace may develop as a function of loading history and brace slenderness. This ductility factor shows considerable variability and sensitivity to loading history. This variability must be considered when evaluating the ability of refined analysis models to predict member failure. The refined analysis may suggest a higher level of confidence in the predicted deformation capacities than those can be supported by test data.

Also of significance is that the ductility values presented by Tremblay are cyclic values, defined as the sum of the peak elongation displacement and compressive displacement divided by the displacement at first buckling. Thus, for a loading history where the amplitudes of displacement are equal in both tension and compression, the ductility values should be divided by two to estimate the maximum shortening of the brace prior to failure. The cyclic ductilities range from about 6 to more than 20, corresponding to unidirectional ductilities for symmetric cycles of about 3 to more than 10. Thus, the braces considered in the database are not too ductile, with the stockier braces having less ductility capacity.

A similar empirical investigation of a nearly identical database has examined the

energy dissipation capacity of braces and the deterioration of energy dissipation efficiency and compression capacity with cumulative plastic shortening as a function of member type and slenderness ratio (Lee and Bruneau, 2005). This research points out many difficulties in defining useful parameters for design or analysis purposes.

Earlier studies of brace test data by Lee and Goel (1987) and Ikeda *et al.* (1984) have produced specific recommendations for two different types of phenomenological model used for braces (Jain and Goel, 1978; Ikeda *et al.,* 1984). With parameters estimated empirically, hysteretic loops can be predicted using the analytical models. As noted previously, these loops do not directly account for any phenomena associated with yielding or buckling of the brace. They only follow the general shape of the hysteretic loops based on empirically derived parameters. Ikeda *et al.* (1984) suggested that the parameters are not well conditioned, however, and are, in fact, very sensitive to materials, section shape, loading history, *etc.* Ikeda and Mahin (1984) subsequently developed a physical theory model for brace buckling that was also calibrated to available test data. This model utilized a generalized axial load-bending moment plastic hinge based on classic plasticity at the center of the member and a large displacement formulation for the internal lateral displacements within the brace. It proved difficult to properly model the behavior of braces in the re-straightening phase from a previously buckled configuration, and a variety of empirical adjustments were imposed to improve accuracy.

Test data is need to evaluate existing brace models and calibrate new ones. Be-

cause of their availably at the beginning of this investigation, the primary experiment source of data used is a series of eight nearly identical Hollow Structural Section (HSS) braces tested at University of California at Berkeley (Yang and Mahin, 2004; Uriz, 2005). The braces (see Figure 2.1) consisted of square $6 \times 6 \times 3/8$ HSS sections fabricated from ASTM A500 Grade B steel having specified minimum strengths of $F_y = 46$ ksi and $F_u = 58$ ksi. Mill certificates showed that the specimens were considerably stronger, with $F_y = 60$ ksi and $F_u = 65$ ksi. The ends of the HSS sections were slotted and welded to gusset plates at each end. The framing members — to which the gusset plates were attached at both ends — were fixed against rotation, but axial elongation or shortening of the brace was permitted. Some specimens were reinforced locally near their ends where there was a reduction of the net area of the brace because of the slots used to fasten the braces to the gusset plates. The KL/r ratio for the braces, considering $K = 1$ and the length L extending between from the faces of the framing members to which the gusset plates were attached, was 51 for all specimens.

Three different types of axial displacement histories were imposed along the longitudinal axis of the brace. One of the loading protocols consisted of a cyclic displacement history based on a nonlinear analysis of a Special Concentrically Braced Frame (SCBF) that was subsequently tested (Uriz, 2005). This would facilitate comparison of hysteretic loops for individual braces and braces tested as part of a structure. A second loading protocol consisted of a near-fault type history, where there was a

modest cycle with compressive loading followed by a large excursion in tension, followed, in turn, by a series of smaller cycles about an offset position. A similar test was done where the signs of the displacement excursions was reversed (*i.e.,* the large displacement excursion was in compression). Finally, a third type of protocol was used where a series of symmetric, constant amplitude displacement cycles at several levels were imposed until the brace failed. These test results were previously used to assess damage accumulation models and the sensitivity of failure to the loading history (Uriz, 2005).

2.2 Investigations of gusset plates

A comprehensive three-year literature review on the behavior of gusset plates was completed in 2005 (Chambers and Ernst, 2005). Including more than 200 papers and reports, this review evaluates the results in terms the ability of modern codes and analysis methods to predict behavior. The conclusions state that the amount of information available on gusset plates for conditions similar to those found in current design practice, and for loads representative of seismic loading conditions, are too few to make an adequate assessment.

To help address this issue, a series of tests are currently underway at the University Washington, Seattle, under the supervision of Professors C. Roeder and D. Lehman (Roeder *et al.,* 2006; Lehman *et al.,* 2008). These tests place the braces along the diagonal of a single story, single bay frame. The braces include buckling restrained

braces as well as conventional braces that are allowed to buckle.

A variety of gusset plate details are used. Initially, gusset plate connections were designed by considering the conventional Whitmore section (effective width, Whitmore, 1952) and the Uniform Force Method (Thornton, 1991; AISC, 2005a), which are basically strength-based design methods and do not consider the inelastic deformation demands expected during seismic loading from brace buckling or frame rotations. Currently, the investigation has expended to include a number of configurations and alternative design methods for the gusset plates. Previous test results have shown that current gusset plate details tend to fail prematurely along the weld connecting the plate to the supporting beam and column, or initiate fracture into the beam or column. Representative damage observed in their tests is shown in Figure 2.2.

A series of simple gusset plate tests were carried out at University of California at Berkeley by Markarian and Mahin (2004). In these tests, only frame flexural deformations were imposed, with no axial tensile or compression loads. The beams to column connections were pinned, consisting of a simple shear tab connection from the beam to the column. The addition of the gusset plate resulted in considerable moment transfer and stress states that do not appear in typical design or analysis practices. These tests demonstrated a tendency for the beams and columns to exhibit complex states of stress, and for the connection to fail in a brittle fashion.

More recent tests have been conducted on gusset plate connection in buckling restrained braced frames (BRBF) system by Kishiki *et al.* (2008). In these tests,

interaction between framing components and the gusset plate was considered, but influence of bracing forces was ignored. Beam-column frame subassemblies with the gusset plate were subjected to cyclic lateral loading. It was found that effective length of the beam shortened by the presence of the gusset plate connections. It was indicating that the critical section of the beam was moved to the toe of the gusset plate. On the other hand, effective length of the column was hardly affected by the gusset-plate when a rectangular hollow section (RHS) was used for the column.

2.3 Investigations of braced frame subassemblies

Most tests of braced frames have used small-scale models or employed details that are not currently in use. Valuable data was obtained from Japanese pseudo-dynamic tests of a full-scale, six-story special concentrically braced frame and eccentrically braced frame. These tests were performed at the Building Research Institute, Tsukuba, Japan, in the mid-1980s (Midorikawa *et al.,* 1988; Foutch *et al.,* 1986). One-third scale models of the same structures were tested on the University of California at Berkeley shaking table (Whittaker *et al.,* 1989).

Relatively few recent tests have been conducted on multistory subassemblies of concentrically braced frames. One recent example was carried out by Uriz (2005). The frame is shown in Figure 2.3, and the displacement history imposed at the roof of the structure is shown in Figure 2.4. The frame suffered extensive damage to the braces in the lower level, the columns at the base of the building, and in the beam-to-column

connections at the first story level. A wide variety of behavior was observed, from yielding, local buckling, local tearing, brace fracture, and column local buckling and connection fracture (Uriz, 2005). Following brace buckling, the strength of the frame degraded significantly from cycle to cycle. This specimen provides a good test of the ability of various methods to predict behavior associated with members undergoing bending and axial load, lateral buckling, and local buckling.

Uriz (2005) reported that the distribution of lateral drift was nearly equal for the top and bottom stories at the beginning of test. Both levels developed slight amounts of buckling, but full lateral buckles formed in the lower level, with local buckling occurring almost immediately (Figure 2.5). Because of the reduced load capacity of the buckled braces, the forces in the upper (and lower) level decreased, and no further tendencies were observed for the upper level to buckle. This resulted in a weak-story response, with nearly all of the inelastic behavior and damage concentrated in the lower level. This led to the complete fracture of the braces during the first design level displacement excursion (Figure 2.6), with failure of the lower level beam to column connections occurring soon thereafter (Figure 2.7).

The hysteretic loop relating the roof lateral force versus base shear is shown in Figure 2.8. The points marked A, B, C, and D represent the initial tearing and final complete fracture of the braces in the lower story. Points E and F represent the fracture of the lower beam to column connection, first on one side of the structure and then on the other. The initial buckling of the braces is easily identified by the

sudden nonlinearity of the system, with slight negative post-buckling tangent stiffness. Substantial deterioration of the specimen load capacity, occurred upon cycling at the level that induced first buckling of the lower level braces. This buckling occurred at relatively small drifts compared to drifts considered for design purposes in the United States. The braces completely fractured during subsequent cycles at this drift level or during the first excursion to the design level.

A series of four full scale, 2-story, single bay braced frame tests were performed at the National Center for Research on Earthquake Engineering (NCREE) in Taiwan (Powell *et al.,* 2008). The first test was a braced frame with HSS tube braces in a multi-story X-brace configuration. It provided an experimental examination of the multi-story X-brace system and of the mid-span gusset plate connections. At the same time, it was a confirmation study for past research on corner gusset plate connections performed at the University of Washington.

Several tests of BRBFs have recently been carried out at University of California at Berkeley (Uriz, 2005). The tested subassemblies consist of portion of a seven-story BRBF. Two configurations of braces were considered. These included a chevron configuration with each unbonded brace having a single flat plate for the yielding core; in one brace the core was oriented horizontally and in the other it was oriented vertically. The second configuration utilized a single unbonded brace oriented across the diagonal of the frame. Two brace sizes were considered: one where the core was the same size as used for the chevron configuration and another where the area was

doubled (and the core was cruciform in shape).

The buckling restrained braces (BRBs) performed quite well in these tests compared to conventional braces; however, considerable yielding was noted throughout the surrounding frame. This included shear yielding of the column webs, yielding of the columns and gusset plates, and yielding of the beam to column connection regions. In addition, gusset plate buckling was noted. Interestingly, this buckling occurred when the attached brace was in tension. The buckling was a result of the kinematic distortion of the gusset plate that occurred as a result of frame action (the gusset plate is squeezed as the brace is loaded in tension). Eventually, fracture was noted in the beams adjacent to the gusset plate. This fracture appeared to be induced as a consequence of frame bending behavior.

A series of tests on BRBFs have been carried out at the NCREE in Taiwan (Tsai *et al.,* 2006). The basic differences between this test and the single diagonal brace test conducted by Uriz (2005) is as follows: (1) a different type of BRB is used; (2) a concrete-over-metal-deck floor system is used; and (3) the frame is subjected to two horizontal components of motion using the pseudo-dynamic test method, leading to bidirectional-bending effects in the columns. The specimen was able to undergo a substantial number of simulated earthquakes. During a moderate level test, a fracture in the welds of the gusset plate to the column was noted and required repair before conducting the subsequent tests. The NCREE has also tested BRBFs in a three-story configuration where the columns were concrete filled steel tubes (Tsai *et al.,* 2004).

2.4 Investigations of beam-column connections

The steel moment connection data used herein are from two sources. One is a series of welded steel beam-column connection tests (Tanaka *et al.,* 2000) conducted by Kajima Corporation, Japan. These tests incorporated box columns and beams with horizontally tapered haunches so that the beam flanges widened to conform to the width of the column. The columns were made of welded square tube section of $400 \times 400 \times 19$ (mm) and steel grade of SS400 (F_y = 280 MPa, F_u = 430 MPa). Beams were made of rolled wide-flange section of $500 \times 200 \times 10 \times 16$ (mm) and steel grade of SS400 (F_y = 270 MPa, F_u = 420 MPa). The distance from the column axis to the load point at beam is 2000 mm. Various forms of ductile behavior were observed with the specimens eventually developing fractures. Specimen BW10, which developed significant local buckling prior to terminating the test, is studied herein. Test setup for specimen BW10 is shown in Figure 2.9.

The other set of data used here is from Suita *et al.,* (2000), where a variety of Japanese style post-Kobe and United States style post-Northridge welded beam-to-column connections were tested. This experimental study compared beams having uniform sections and reduced beam sections in the plastic hinge region. Duplicate specimens fabricated by two manufacturers were tested to identify variability in performance with different heats of steel and manufacture. The beam-column connections with a uniform flange section and no weld access hole (NWAH) failed because of low-cycle fatigue. They are used in current research. The columns were made of

cold-formed square tube section of 350 × 350 × 12 (mm) and steel grade of BCR295 (F_y = 295 MPa, F_u = 400 MPa). And the beams were made of rolled wide-flange section of 500 × 200 × 10 × 16 (mm) and steel grade of SN400B (F_y = 235 MPa, F_u = 400 MPa). The distance from the column axis to the load point at beam is 3000 mm. Test setup for specimen N4 studied herein is shown in Figure 2.10.

An extensive database of results of steel beam-to-column connection tests has recently been compiled by Lignos and Krawinkler (2007).

2.5 Concluding remarks

Considerable experimental data exists on components such as conventional braces, beams, columns, and connections, and on subassemblies including these components. Some of this well-documented data will be used to calibrate or validate the numerical models developed in this research.

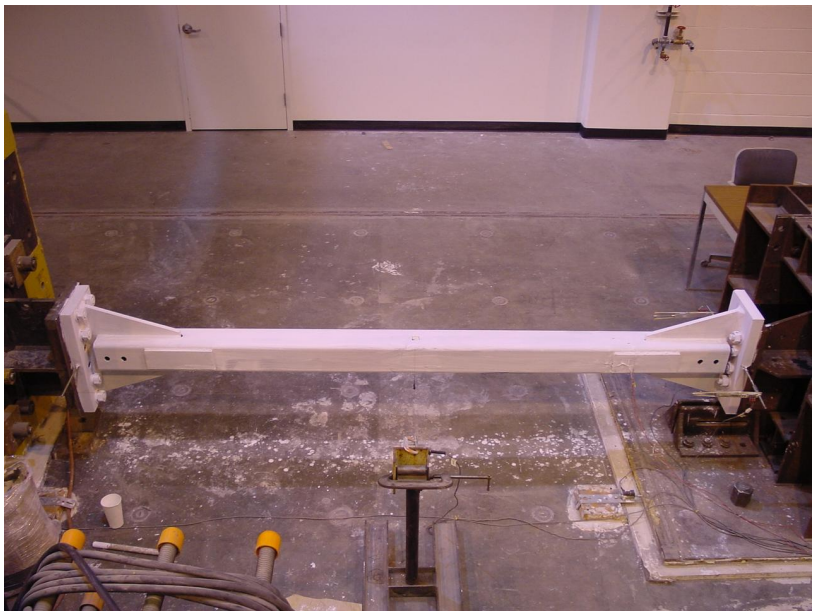

(a) Specimen

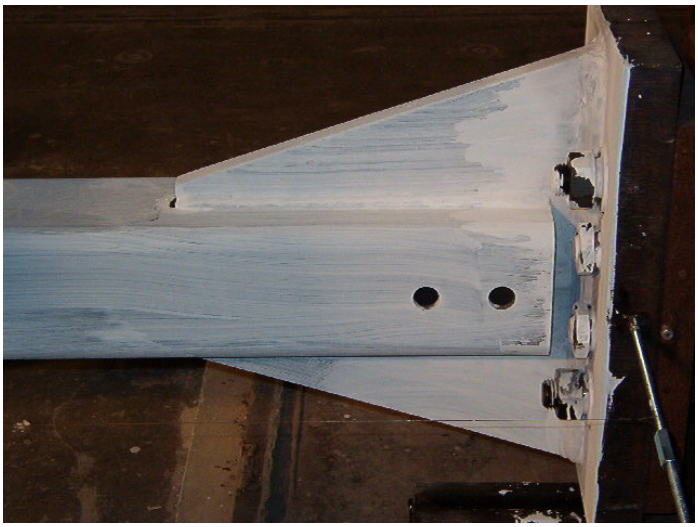

(b) End connection

Figure 2.1: Experimental setup for conventional brace test (Yang and Mahin, 2005)

(a) Crack initiation and propagation

(b) Complete rupture

Figure 2.2: Gusset plate damage (Roeder *et al.,* 2006)

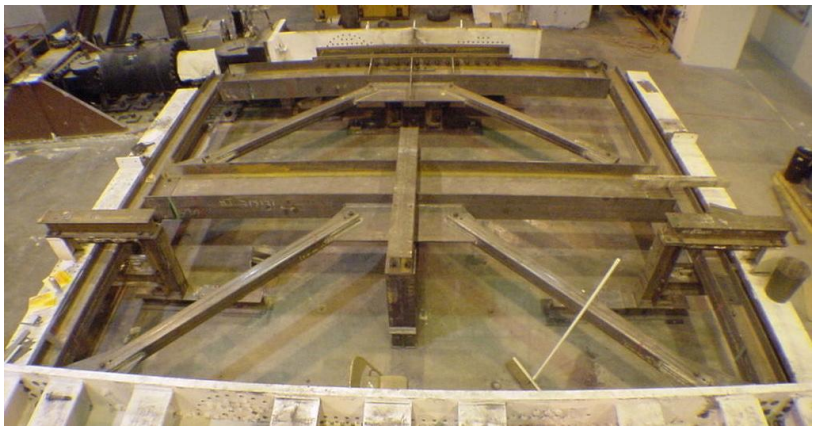

Figure 2.3: Test setup for SCBF (Uriz, 2005)

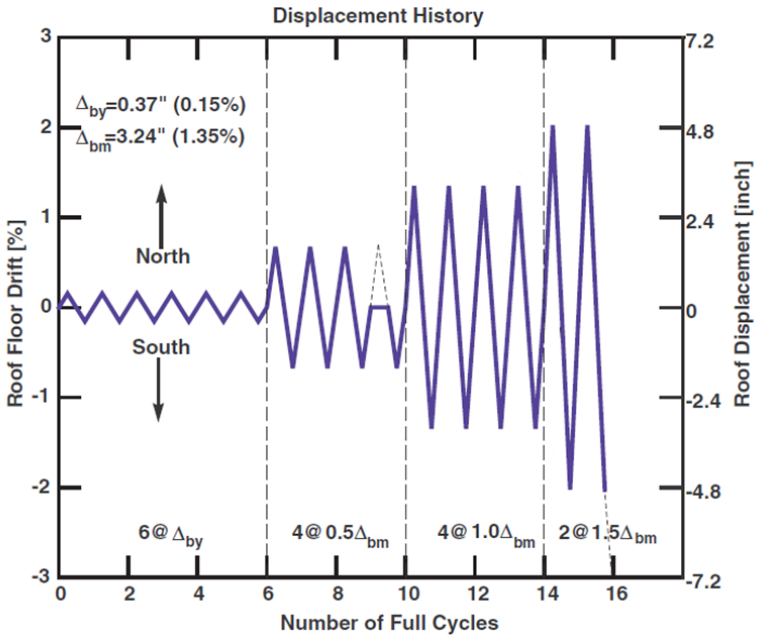

Figure 2.4: Target roof displacement history of SCBF test (Uriz, 2005)

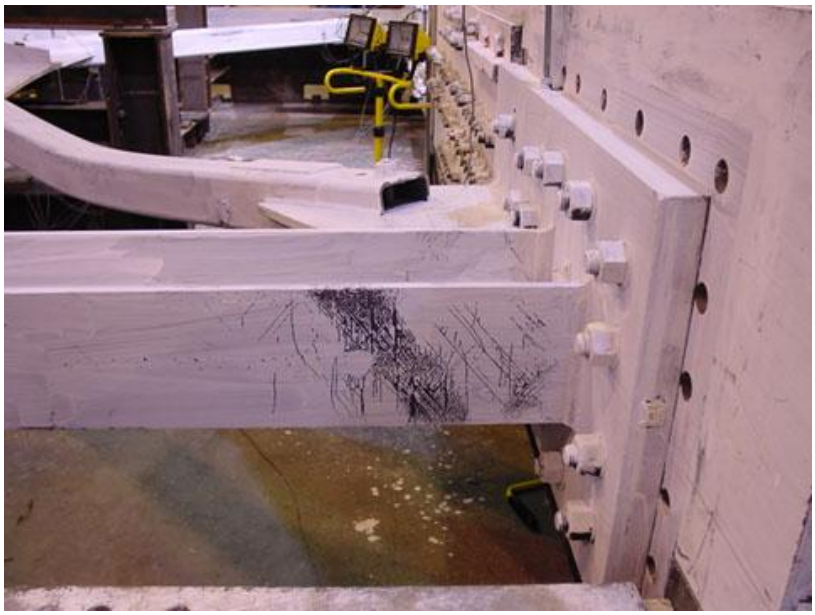

(a) Global buckling

(b) Local buckling

Figure 2.5: Brace buckling (Uriz, 2005)

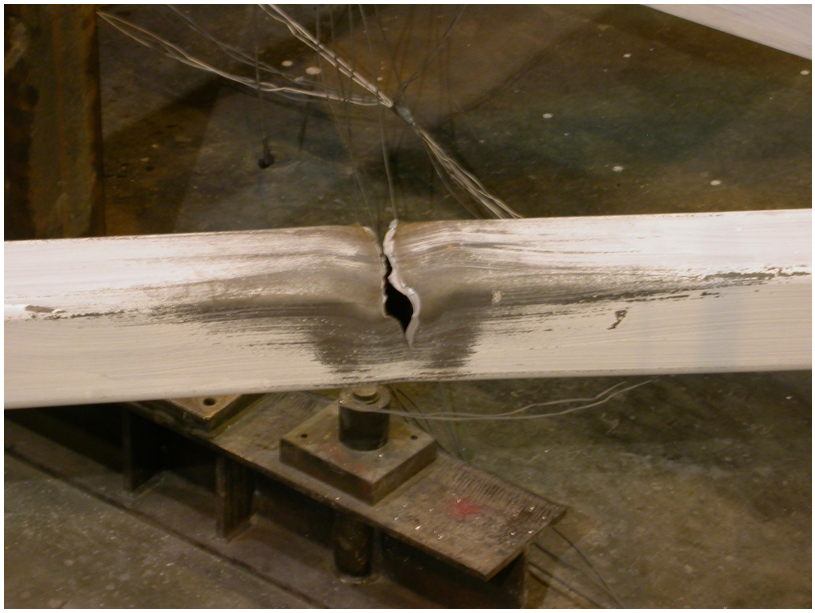

(a) Crack propagation

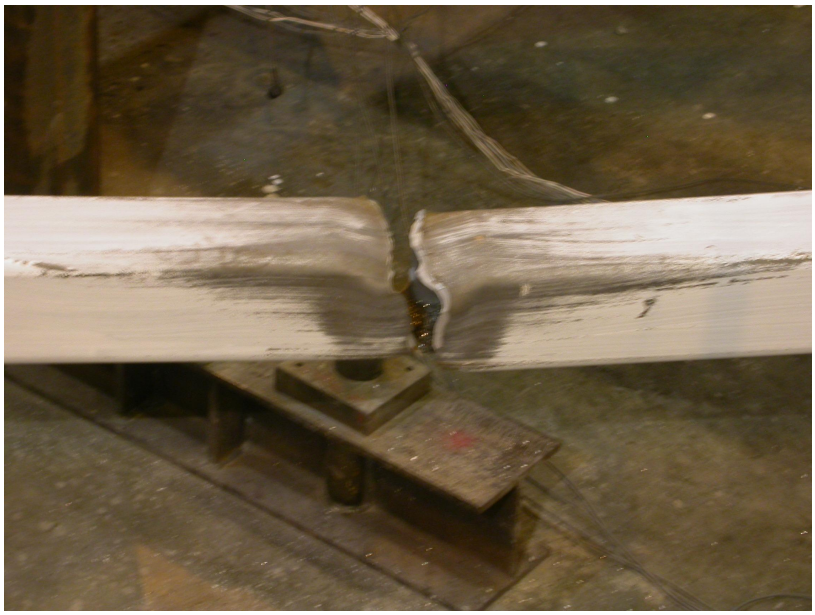

(b) Complete rupture

Figure 2.6: Brace failure (Uriz, 2005)

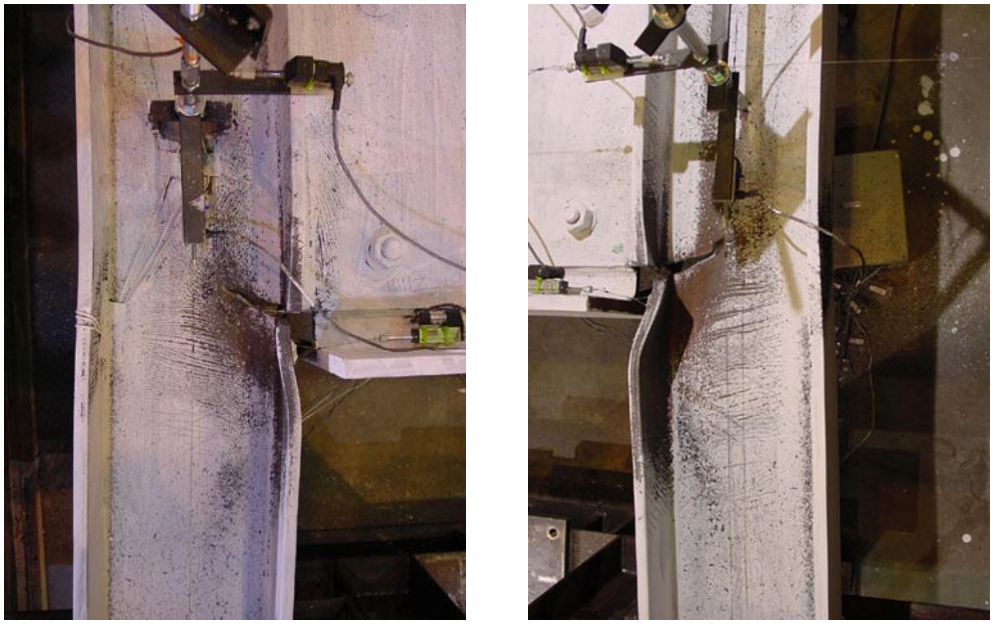

Figure 2.7: Beam-column connection failure (Uriz, 2005)

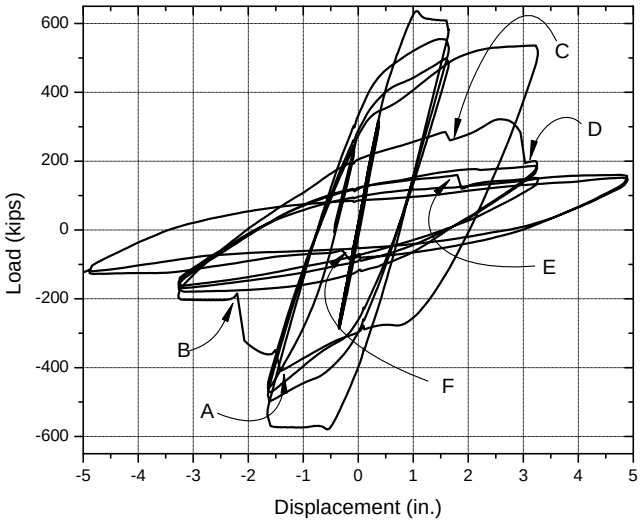

Figure 2.8: Base shear versus roof lateral displacement (Uriz, 2005)

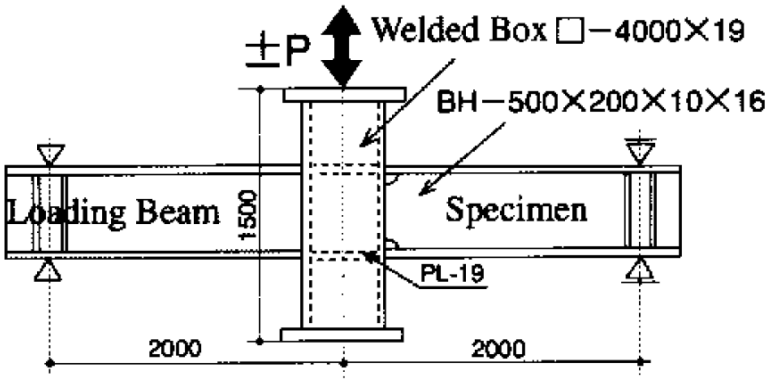

Figure 2.9: Test setup for BW10 beam-column connection (Tanaka *et al.,* 2000)

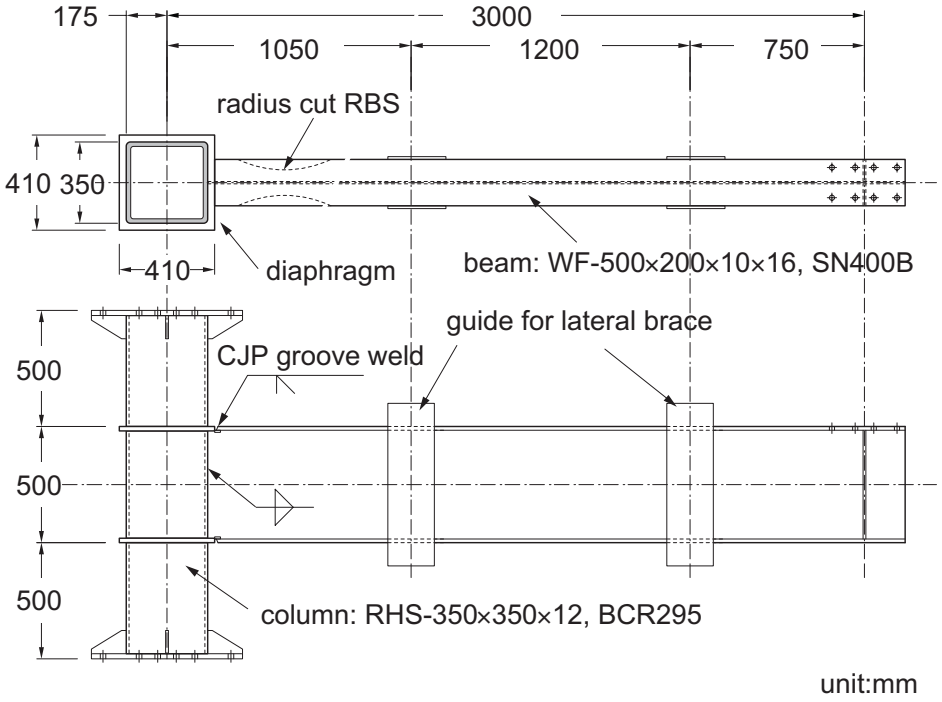

Figure 2.10: Test setup for N4 beam-column connection (Suita *et al.,* 2000)

Chapter 3

Structural Steel Deterioration

For structural steel subjected to a severe cyclic loading history, such as that experienced during a strong earthquake, several stages of behavior commonly exist during the course of material deterioration. Initially, it is assumed there are no macroscopic cracks or defects, thus no stress or strain singularities are associated with the material. The material is then loaded non-proportionally and cyclically into the inelastic regime under asymmetric stress and strain histories of varying amplitude. Deterioration then develops because of imposition of large plastic deformation, resulting in substantial energy dissipation. This causes progressive failure of the material volume through ductile damage and fracture associated with microvoid nucleation, growth, and coalescence. After complete failure of a local material volume, a macroscopic crack is initiated eventually.

Damage resulting from plastic deformation in ductile metals is mainly because of

the formation of microvoids, which initiate (nucleate) either as a result of fracturing or debonding of inclusions such as carbides and sulfides from the ductile matrix. The growth and coalescence of microvoids under increasing plastic strain progressively reduces the material's capability to carry loads and can result in complete failure. Figure 3.1 shows the section of a tensile specimen during the necking process [defined as a mode of tensile deformation where relatively large amounts of strain localize disproportionately in a small region of the material, in Bridgman (1952)], clearly demonstrating void accumulation at the specimen center (Puttick, 1959). Figure 3.2 schematically illustrates the nucleation, growth, and coalescence of such microvoids (Anderson, 1995). If the initial volume fraction of voids is low, each void can be assumed to grow independently; upon further growth, neighboring voids interact. Plastic strain eventually concentrates along a sheet of voids, and local necking instabilities develop as shown schematically in the figure.

A proper modeling of this micro-void nucleation and growth mechanism is needed to predict ductile failure in steel members and structures. In the context of continuum mechanics, plasticity and damage models are essential for the simulation. Plastic behavior and models, damage and fracture of structural steel under monotonic and cyclic loading are discussed in the following sections.

Figure 3.1: Void accumulation in a tensile specimen (Puttick, 1959)

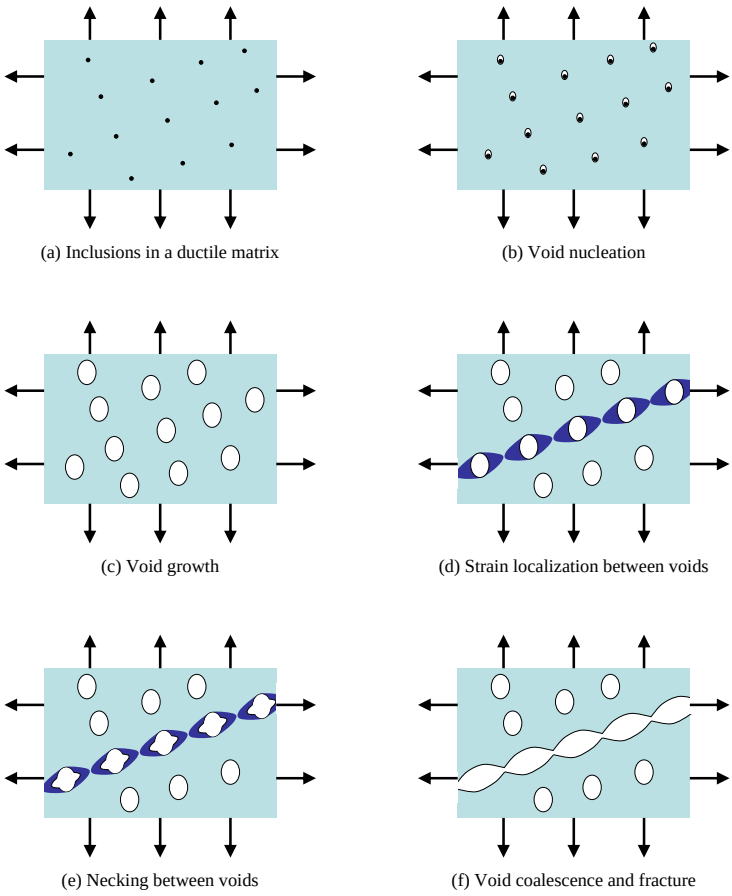

[after Anderson (1995)]

Figure 3.2: Void nucleation, growth, and coalescence in ductile metals

3.1 Plastic behavior and models

Isotropic hardening and/or kinematic hardening are commonly used to describe the plastic behavior of metal-like materials under complex loading conditions. Prager (1956) and Ziegler (1959) initiated the fundamental framework used for kinematic hardening rules. Armstrong and Frederick (1966) developed a nonlinear kinematic hardening rule that generalized its linear predecessor. In this model, the kinematic hardening component is defined to be an additive combination of a purely kinematic term (*i.e.,* the linear Prager/Ziegler hardening law) and a dynamic recovery term, which introduces the nonlinearity. When combined together with isotropic hardening, such a model can account for the following observed phenomena: (1) Nonlinear Bauschinger effect (Figure 3.3); (2) Cyclic hardening (Figure 3.3); and (3) Ratcheting (Figure 3.4).

The Armstrong and Frederick's rule was further extended by Chaboche (1986, 1989), where an additive decomposition of the back stress was postulated. The evolution equation of each back stress component is similar to the work done by Armstrong and Frederick (1966). The advantages of this superposition are that a larger strain range can be realistically modeled, and a more accurate description of ratcheting is provided. These features allow modeling of inelastic behaviors of metals that are subjected to cycles of load, resulting in significant inelastic deformation and, possibly, low-cycle fatigue failure. Discussion of these plasticity models can be found in Lemaitre and Chaboche (1990).

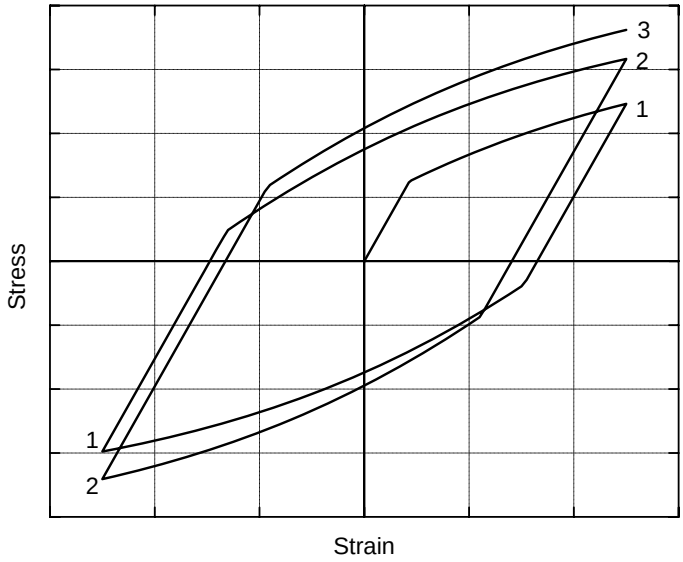

Figure 3.3: Nonlinear Bauschinger effect and cyclic hardening

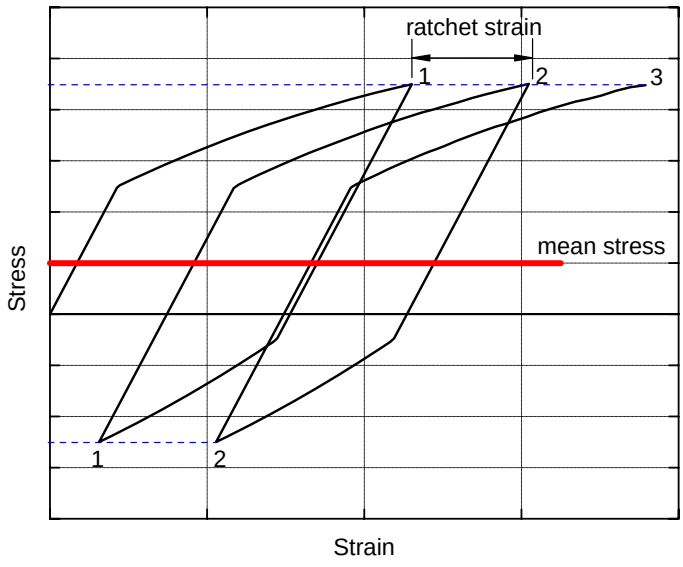

Figure 3.4: Ratcheting under asymmetric stress history

3.2 Damage and fracture under monotonic loading

Two alternative approaches are generally considered for modeling material failure: local approaches and global approaches. Local approaches focus on issues related to micromechanics, whereas global approaches address issues of fracture mechanics.

3.2.1 Local approaches

The local approach to fracture can be defined very generally as the combination of the following two factors: (1) the computation of local stress and deformation values in the most loaded zones of a component or structure; and (2) the use of predefined empirical models corresponding to various fracture mechanisms, such as cleavages, ductile fracture, fatigue, creep, stress-corrosion, *etc.* (Rousselier, 1987). The parameters needed for these empirical models are obtained by calibration to experimental data.

Many damage models have been developed since the initial micromechanics studies of McClintock (1968) and Rice and Tracey (1969). The models can be categorized into two classes: (1) void volume fraction models; and (2) continuum damage mechanics models. In the first group, failure is predicted when void volume fraction reaches a critical value. In the second group, the material is considered fractured when the reduction of effective area exceeds a critical value.

Both types of models can be written in the form of stress-modified critical plastic

strain:

$$\text{Damage evolution} \qquad D = \int F\left(\boldsymbol{\sigma}\right) G\left(\dot{\boldsymbol{\epsilon}}^{p}\right) \, \mathrm{d}t \tag{3.1a}$$

$$\text{Failure criteria} \qquad D = D_c \tag{3.1b}$$

where $\boldsymbol{\sigma}$ is the stress tensor, F is the stress modification function, $\dot{\boldsymbol{\epsilon}}^{p}$ is the plastic strain rate tensor, G is the plastic strain rate function, D represents the damage of the material, and D_c is the value of the critical damage parameter at failure. For example, the Rice and Tracey (1969) model can be written as

$$F\left(\boldsymbol{\sigma}\right) = \exp\left(1.5\sigma_m/\sigma_{eq}\right) \qquad G\left(\dot{\boldsymbol{\epsilon}}^{p}\right) = \dot{\bar{\varepsilon}}^{p} \tag{3.2}$$

where $\sigma_m = \boldsymbol{\sigma} : \mathbf{1}/3$ is the mean stress, $\sigma_{eq} = \sqrt{3/2}\|\boldsymbol{\sigma}\|$ is the equivalent stress, σ_m/σ_{eq} is the stress triaxiality, and $\dot{\bar{\varepsilon}}^{p}$ is the equivalent plastic strain rate, defined as

$$\dot{\bar{\varepsilon}}^{p} = \sqrt{\frac{2}{3}\dot{\boldsymbol{\epsilon}}^{p} : \dot{\boldsymbol{\epsilon}}^{p}} \tag{3.3}$$

For the porous metal plasticity model (GTN model) developed by Gurson (1977), and Tvergaard and Needleman (1984), a sophisticated yield function is developed and the void growth part is given by

$$F\left(\boldsymbol{\sigma}\right) = 1 \qquad G\left(\dot{\boldsymbol{\epsilon}}^{p}\right) = \dot{\varepsilon}_{v}^{p} = \dot{\boldsymbol{\epsilon}}^{p} : \mathbf{1} \tag{3.4}$$

where $\dot{\varepsilon}_{v}^{p}$ is the volumetric plastic strain rate, and $\mathbf{1}$ is the second-order identity tensor $\mathbf{1} = \delta_{ij}\boldsymbol{e}_i \otimes \boldsymbol{e}_j$.

For the ductile damage model proposed by Lemaitre (Lemaitre, 1992; Dufailly and Lemaitre, 1995), which is based on continuum damage mechanisms (CDM) introduced

by Kachanov (1958), the damage evolution function becomes

$$F(\boldsymbol{\sigma}) = \left[\frac{Y}{S}\right]^t \qquad G(\dot{\boldsymbol{\epsilon}}^p) = \dot{\bar{\varepsilon}}^p \tag{3.5}$$

where S is a material constant in energy density units, t is a dimensionless material constant, and Y is the internal energy density release rate, calculated as

$$Y = \frac{1}{2}\boldsymbol{\sigma} : [\mathbb{D}^e]^{-1} : \boldsymbol{\sigma} \tag{3.6}$$

where $\mathbb{D}^e$ represents the fourth-order elasticity tensor

$$\mathbb{D}^e = \kappa \mathbf{1} \otimes \mathbf{1} + 2G(\mathbb{I} - \frac{1}{3}\mathbf{1} \otimes \mathbf{1}) \tag{3.7}$$

where λ and G are the Lamé constants, and $\mathbb{I}$ is the fourth-order symmetric identity tensor.

$$\mathbb{I} = \frac{1}{2}\left[\delta_{ik}\delta_{jl} + \delta_{il}\delta_{jk}\right] \boldsymbol{e}_i \otimes \boldsymbol{e}_j \otimes \boldsymbol{e}_k \otimes \boldsymbol{e}_l \tag{3.8}$$

The Rice and Tracey (1969) model and Lemaitre (1992) model predict very similar trends in the case of proportional loading, as seen in Figure 3.5, where the equivalent plastic strain to failure $\bar{\varepsilon}_f^p$ versus stress triaxiality σ_m/σ_{eq} is plotted for the two models. In the case of non-proportional loading, Marini *et al.* (1985) showed that the two models also give similar results. Recently, Steglich *et al.* (2005) investigated the relationship between the CDM and the GTN models.

3.2.2 Global approaches

Global approaches are based on asymptotic continuum mechanics analysis. Under some situations, single- or dual-parameters can uniquely characterize the crack tip

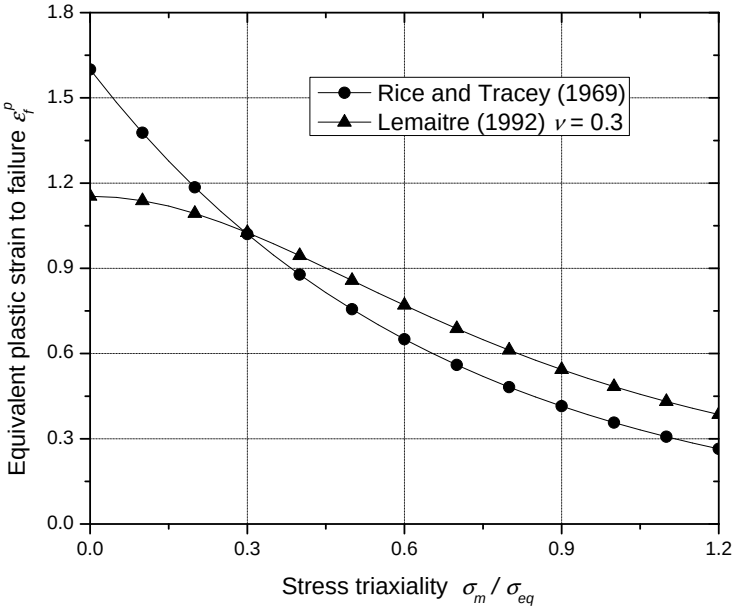

Figure 3.5: Equivalent plastic strain to failure versus stress triaxiality

condition. Well-known single-parameter variables are stress intensity K, J-integral, and CTOD (crack tip opening displacement). A well-known dual-parameter formulation is based on the addition of a T-stress parameter that characterizes the crack tip constraint.

All these parameters are defined at the global level of the crack medium, within the framework of fracture mechanics. They are applicable to a number of situations where it is not necessary to know the exact state of stress or damage in the vicinity of the crack tip (ranging from a two-dimensional, almost elastic medium, with only a small plastic zone relative to the crack size; to a three-dimensional medium subjected to proportional loading or cyclic loading in fatigue). On the other hand, this approach may prove deficient in some cases, because of the size of the cracks, pronounced overall plasticity during ductile fracture, or loading history effects.

3.2.3 Relation between local and global approaches

A systematic comparative and parametric study of local and global models was reported by Xia and Shih (1995) using the representative volume element (RVE) methodology. Here, the size of the elements in the fracture process layer (the fracture elements representing the crack) in local approaches is the key parameter linking local and global approaches, and an approximate equality exists:

$$J_{Ic} = \mu d \sigma_0 \tag{3.9}$$

where J_{Ic} is the critical J-integral under the Mode I condition, d is the size of the elements, σ_0 is the flow stress, and μ is a factor of order unity, suggesting that the element size in local approaches should be on the order of J_{Ic}/σ_0 or CTOD to obtain consistent results. This may make local approaches infeasible for large structural systems or subassemblies.

3.3 Damage and fracture under cyclic loading

In this section, local approaches (as defined in previous section) to modeling damage and fracture under cyclic loading are examined in more detail. This approach is compared to the popular Manson-Coffin rule for low-cycle fatigue. The traditional Manson-Coffin rule "increments" the damage state only at the end of each cycle. In contrast, the micromechanics and damage plasticity approach "ramps" the damage continuously during cycling.

3.3.1 Manson-Coffin rule

The Manson-Coffin rule is a popular model for low-cycle fatigue because of its simplicity. Generally, it is written in the form

$$\frac{\Delta\varepsilon_p}{2} = \varepsilon'_f(2N_f)^c \tag{3.10}$$

where $\Delta\varepsilon_p/2$ is the amplitude of plastic strain, N_f is the number of cycles, ε'_f is the ductility coefficient, and c is the ductility exponent. In 1953, Manson, recognizing the form of Equation (3.10) relating fatigue life and plastic strain range, suggested that the magnitude of $1/c$ was "in the neighborhood of three" (Manson, 1953). Coffin (1954) showed that for practical purposes the fatigue property c is approximately equal to $-1/2$, and that ε'_f is related to the monotonic fracture ductility ε_f (Tvernelli and Coffin, 1959). Actually, c commonly ranges from -0.5 to -0.7 for most metals, with -0.6 as a representative value.

Despite a large amount of work to generalize this law to multi-axial states of stress (*e.g.,* Morrow, 1964) and to complex histories of loading (Manson *et al.,* 1971), it remains a model generally only applied to uniaxial periodic loadings. Still, a wide variety of tests of structure, component, and material specimens have demonstrated the general validity of the Manson-Coffin relation, and the range for the coefficient c cited above.

Recently, Uriz (2005) utilized the Manson-Coffin rule together with Palmgren-Miner linear hypothesis for damage accumulation (Palmgren, 1924; Miner, 1945) and

the rainflow cycle counting method (Matsuishi and Endo, 1968) to predict the low-cycle fatigue behavior of uniaxially loaded struts. This approach mimics rupture of uniaxially loaded material fibers used to represent the cross-section of a member. They simplified the rainflow cycle counting method so that only several recent cycles were considered. This allows computation of damage during the response rather than just at the end. After parameter calibration it was shown that the prediction matched the experiment quite well. Note that the continuous damage models discussed in this chapter do not rely on cycle counting algorithms, but rather damage continuously accumulating based on the damage mechanics models presented.

3.3.2 Continuous damage models

Not much attention has been given to the possibility of incorporating damage into cyclic plasticity by means of micromechanics. Recent works on porous metal plasticity are those of Leblond *et al.* (1995), Besson and Guillemer-Neel (2003), and Cedergren *et al.* (2004). These models introduce nonlinear kinematic hardening into the GTN model. As far as continuum damage mechanics is concerned, Pirondi and Bonora (2003) introduced uniaxial conditions to model stiffness recovery during tension-compression cyclic loading. Kanvinde and Deierlein (2004) extended the Rice and Tracey (1969) formulation to incorporate a cyclic void growth model (CVGM). They revised the material characteristic D_c in Equation (3.1).

$$D_c = D_{c0} \exp(\lambda \bar{\varepsilon}^p) \tag{3.11}$$

so that the critical void volume fraction decreases as the equivalent plastic strain increases, and then revising the stress modification function as

$$F(\boldsymbol{\sigma}) = \frac{|\sigma_m|}{\sigma_m} \exp(1.5\sigma_m/\sigma_{eq}) \tag{3.12}$$

so that the void volume fraction decreases (heals) in compression.

Lemaitre (1992) introduced a relative simple modification for damage evolution in cyclic loading

$$\dot{D} = \begin{cases} \left[\frac{Y}{S}\right]^t \dot{\bar{\varepsilon}}^p & \sigma_1 > 0 \\ 0 & \text{otherwise} \end{cases} \tag{3.13}$$

where σ_1 is the maximum principal stress. Here, damage does not accumulate when all principle stresses are in compression. In the present investigation, this is further revised for simpler implementation as:

$$\dot{D} = \begin{cases} \left[\frac{Y}{S}\right]^t \dot{\bar{\varepsilon}}^p & \frac{\sigma_m}{\sigma_{eq}} > -\frac{1}{3} \\ 0 & \text{otherwise} \end{cases} \tag{3.14}$$

This simplification has negligible effect for most states of stress.

To schematically illustrate the difference between the CVGM and CDM models, preliminary results of an analysis of an individual brace (presented later in more detail in Section 5.2.1) are shown in Figures 3.6 and 3.7. From Figure 3.6 it can be seen that for the cyclic void growth model, the damage D increases during some portions of the deformation cycle and then heals in other portions, and the critical damage parameter D_c decreases with pseudo-time [according to Equation (3.11)]. In contrast, for the

same example, the continuum damage model given by Equation (3.14) only increases with increasing pseudo-time, and the critical damage parameter D_c is a constant. The numerical values of the critical damage parameters, D_{c0} for the CVGM and D_c for the CDM models will, in general, differ. For the sake of this illustration, they have been loosely calibrated to tail at about the same time.

It is also worth mentioning that although the critical equivalent-plastic-strain approach ($F(\boldsymbol{\sigma}) = 1, G(\dot{\boldsymbol{\epsilon}}^p) = \dot{\bar{\varepsilon}}^p$) can be used in proportional loading cases where the triaxiality is constant and known, it is unsuitable for arbitrary cases of cyclic loading. As illustrated in Table 3.1 (and approximately in Figures 3.8 and 3.9), fatigue life (number of cycles to failure) will tend to be underestimated if large strain amplitude data is used to calibrate the parameters (by a factor of 4 in the table); conversely, the fatigue life will tend to be overestimated if small strain amplitude data is used to calibrate the parameters. This is an inherent and important drawback of applying the critical equivalent-plastic-strain criterion to cyclic loading. This drawback is one of the reasons why "stress-modified" critical plastic strain criteria, such as CVGM and CDM, are typically used to simulate low-cycle fatigue failure behavior under arbitrarily varying strain histories. The other reason is the triaxiality-independence of critical equivalent plastic strain criterion; the effect of triaxial constraint on the initiation of rupture is a well-known phenomenon.

3.3.3 Simple comparison of the continuous damage models with the Manson-Coffin rule

Although the basic trends predicted by the Manson-Coffin rule have been verified by considerable low-cycle fatigue data, the rule only increments the damage state at the end of each cycle. This rule is not suitable for the case where the number of cycles to failure is less than 10, because this will not allow a point in a material to fracture until the end of a full cycle. Continuous damage models resolve this difficulty. Thus, it is useful to use the Manson-Coffin rule as a reference and to compare results of different continuous damage models to results predicted by the Manson-Coffin rule.

For this comparison, the cyclic void growth model in Equation (3.11) and (3.12) and the simplified continuum damage mechanics model in Equation (3.14) are evaluated for low-cycle fatigue and compared against the Manson-Coffin rule. A uniaxial stress condition model is subjected to a series of constant amplitude strain cycles considering several amplitudes of maximum strain. These cyclic deformation histories are imposed until rupture of the material occurs. In this way, standard Manson-Coffin type plots can be prepared for the analysis results, and these can be compared directly with the most basic Manson-Coffin criteria for an ideal experiment, as shown in Figures 3.8 and 3.9. Both models predict results that agree with those computed with the Manson-Coffin rule, with the ductility exponent c ranging from -0.5 to -0.7; *i.e.,* corresponding to typical values for metals.

Note that the low-cycle fatigue criterion based on critical equivalent plastic strain

results in a fixed ductility exponent c equal to -1. As such, it cannot predict the correct trend of low-cycle fatigue for metals. Thus, although the effective plastic strain criterion can be calibrated for a particular material and specimen configuration subjected to a specific loading protocol, the same failure criterion might be inappropriate for different loading histories at other locations within the same structure.

Considering that the CDM result in Figure 3.9 is more accurate than CVGM result in Figure 3.8, and that CDM is comparatively easy to implement and numerically more efficient, the simplified CDM model in Equation (3.14) is chosen herein as the damage evolution model for further investigation. It is believed that some underlying relationship should be satisfied when continuous damage models match the Manson-Coffin relation, suggesting that deeper investigation is needed.

3.4 Concluding remarks

This chapter systematically reviews material models for structural steel subject to plasticity, damage, and failure, and subject to cyclic loading history. Among several models reviews, the sophisticated low-cycle fatigue model based on damage mechanics is chosen because of its ability to reproduce the Manson-Coffin relation with reasonable accuracy.

Calibrated to large strain amplitude data

	Strain amplitude	Failure Cycle	Test/EPS
Test	0.20	2	1.00
EPS*		2	
Test	0.05	32	4.00
EPS		8	

Calibrated to small strain amplitude data

	Strain amplitude	Failure Cycle	Test/EPS
Test	0.20	2	0.25
EPS		8	
Test	0.05	32	1.00
EPS		32	

*EPS — critical equivalent-plastic-strain criterion

Table 3.1: Simple illustration of the difference between predictions of number of cycles to failure for an ideal experiment following the Manson-Coffin relation

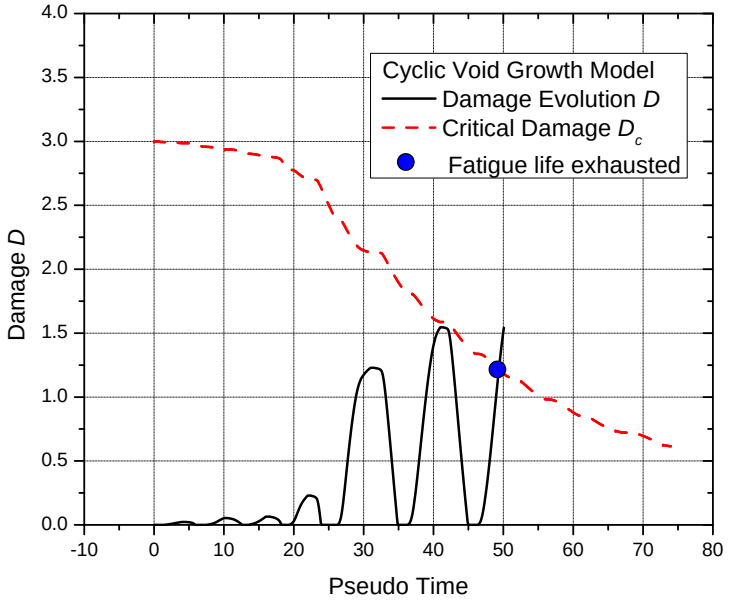

Figure 3.6: Damage evolution of CVGM model

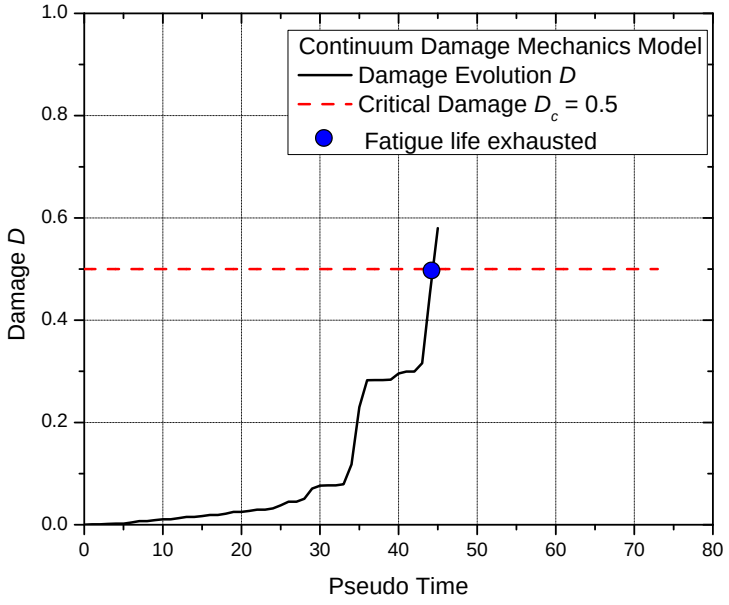

Figure 3.7: Damage evolution of CDM model

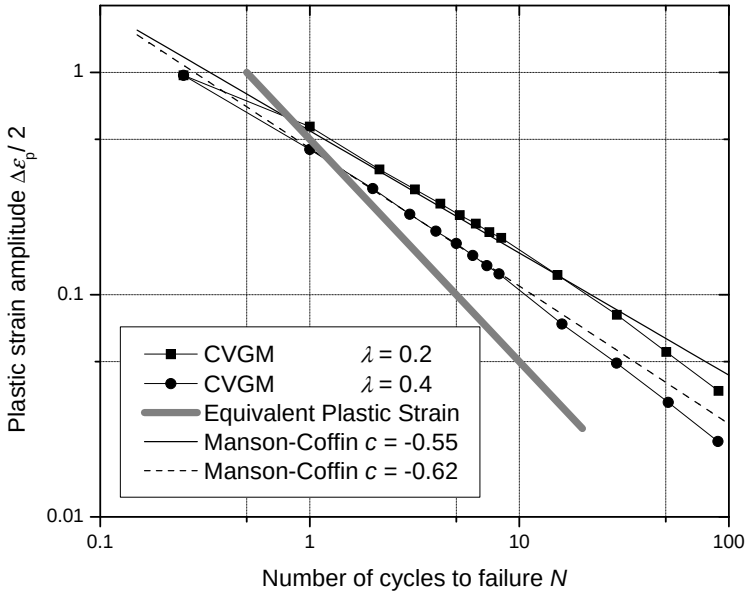

Figure 3.8: Manson-Coffin plot of CVGM model

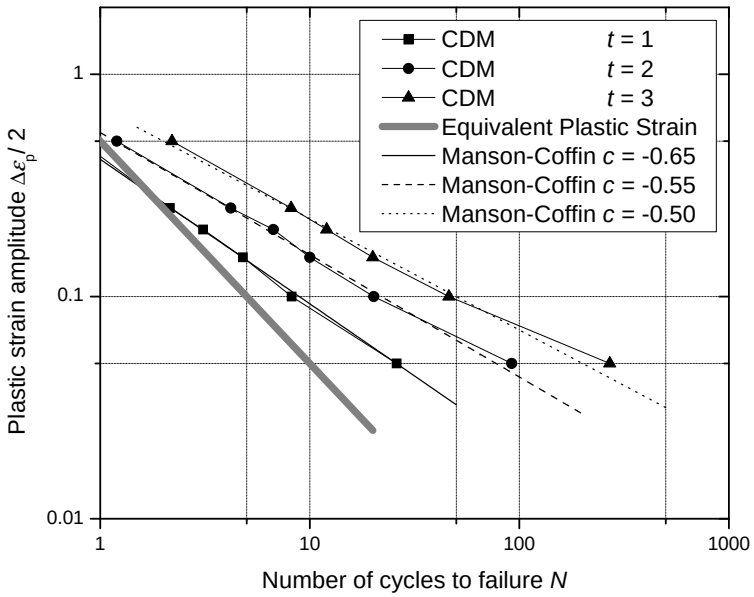

Figure 3.9: Manson-Coffin plot of CDM model

Chapter 4

Cyclic Damage Plasticity Model

This chapter develops a cyclic damage plasticity model based on the review of material models in previous chapter. First, the theory of plasticity and damage evolution is presented. Next, implementation of plasticity and damage models using the cutting-plane algorithm or the closest-point algorithm is discussed. Finally, examples of time integration procedure for brick and shell elements is shown step-by-step. The cyclic damage plasticity model is used in next two chapters for calibration, validation, application, and studies of steel braced frame components and subassemblies.

4.1 Theory of plasticity and damage evolution

Components of the damage plasticity model, including strain rate decomposition, yield criterion, isotropic and kinematic hardening behavior, and damage evolution are summarized in this section.

4.1.1 Strain rate decomposition

The rate-of-deformation tensor $\dot{\boldsymbol{\epsilon}}$ is written in the additive form of the elastic and plastic strain rate components as

$$\dot{\boldsymbol{\epsilon}} = \dot{\boldsymbol{\epsilon}}^e + \dot{\boldsymbol{\epsilon}}^p \tag{4.1}$$

4.1.2 Elastic behavior

The elastic behavior is modeled as isotropic hypoelasticity, *i.e.,* the corotational rate of the Cauchy stress tensor $\dot{\boldsymbol{\sigma}}$ is calculated from the elastic strain rate tensor $\dot{\boldsymbol{\epsilon}}^e$ as

$$\dot{\boldsymbol{\sigma}} = \mathbb{D}^e : \dot{\boldsymbol{\epsilon}}^e \tag{4.2}$$

where $\mathbb{D}^e$ represents the fourth-order elasticity tensor

$$\mathbb{D}^e = \kappa \mathbf{1} \otimes \mathbf{1} + 2G(\mathbb{I} - \frac{1}{3}\mathbf{1} \otimes \mathbf{1}) \tag{4.3}$$

where λ and G are the Lamé constants, $\mathbf{1}$ is the second-order identity tensor, and $\mathbb{I}$ is the fourth-order symmetric identity tensor.

$$\mathbf{1} = \delta_{ij} \boldsymbol{e}_i \otimes \boldsymbol{e}_j \tag{4.4a}$$

$$\mathbb{I} = \frac{1}{2}\left[\delta_{ik}\delta_{jl} + \delta_{il}\delta_{jk}\right] \boldsymbol{e}_i \otimes \boldsymbol{e}_j \otimes \boldsymbol{e}_k \otimes \boldsymbol{e}_l \tag{4.4b}$$

4.1.3 Plastic behavior

The plastic behavior is modeled as pressure-independent plasticity. If the Huber-von Mises yield condition is adopted, the yield surface is defined by the function

$$F = \bar{\sigma} - \sigma_y = 0 \tag{4.5}$$

where σ_y is uniaxial yield stress, and $\bar{\sigma}$ is the effective von Mises stress, with respect to the effective deviatoric stress tensor

$$\boldsymbol{s}_e = \text{dev}[\boldsymbol{\sigma}] - \boldsymbol{\alpha} = \boldsymbol{s} - \boldsymbol{\alpha} \tag{4.6}$$

where $\boldsymbol{s}$ is deviatoric stress tensor and $\boldsymbol{\alpha}$ is the back stress tensor, which is decomposed into multiple tensor components

$$\boldsymbol{\alpha} = \sum_j \boldsymbol{\alpha}_j \tag{4.7}$$

The effective von Mises stress is defined as

$$\bar{\sigma}\left(\boldsymbol{s}_e\right) = \sqrt{\frac{3}{2}\boldsymbol{s}_e : \boldsymbol{s}_e} = \sqrt{\frac{3}{2}}\|\boldsymbol{s}_e\| \tag{4.8}$$

The model assumes associated Levy-Saint Venant plastic flow, *i.e.,* the plastic strain rate tensor is defined as

$$\dot{\boldsymbol{\epsilon}}^p = \frac{\partial F}{\partial \boldsymbol{\sigma}}\dot{\lambda} = \frac{3}{2}\frac{\boldsymbol{s}_e}{\bar{\sigma}}\dot{\lambda} = \frac{3}{2}\boldsymbol{n}\dot{\lambda} \tag{4.9}$$

where $\dot{\lambda}$ is the plastic consistency parameter, and $\boldsymbol{n}$ is the flow direction

$$\boldsymbol{n} = \frac{\boldsymbol{s}_e}{\bar{\sigma}} \tag{4.10}$$

Note that for the sake of implementation simplicity, $\boldsymbol{n}$ is *not* a unit vector; its norm is

$$\|\boldsymbol{n}\| = \sqrt{\frac{2}{3}} \tag{4.11}$$

Adoption of the above form of von Mises yield criterion results in $\dot{\lambda} = \dot{\bar{\varepsilon}}^p$, where $\dot{\bar{\varepsilon}}^p$ is the equivalent plastic strain rate defined as

$$\dot{\bar{\varepsilon}}^p = \sqrt{\frac{2}{3}\dot{\boldsymbol{\epsilon}}^p : \dot{\boldsymbol{\epsilon}}^p} \tag{4.12}$$

4.1.4 Nonlinear isotropic/kinematic hardening model

The size of the yield surface σ_y is a function of equivalent plastic strain $\bar{\varepsilon}^p$ for materials that either cyclically harden or soften.

$$\sigma_y = \sigma_y\left(\bar{\varepsilon}^p\right) \tag{4.13}$$

where the equivalent plastic strain is defined as an accumulation

$$\bar{\varepsilon}^p(t) = \int_0^t \dot{\bar{\varepsilon}}^p(\tau)\ \mathrm{d}\tau \tag{4.14}$$

The evolution of the back stress tensor components are of the Armstrong-Frederick type (Armstrong and Frederick, 1966), defined as

$$\dot{\boldsymbol{\alpha}}_j = \frac{2}{3}C_j\dot{\boldsymbol{\epsilon}}^p - \gamma_j\boldsymbol{\alpha}_j\dot{\bar{\varepsilon}}^p = \left[C_j\boldsymbol{n} - \gamma_j\boldsymbol{\alpha}_j\right]\dot{\bar{\varepsilon}}^p \tag{4.15}$$

where C_i and γ_i are material parameters. The recall term $\gamma_j\boldsymbol{\alpha}_j\dot{\bar{\varepsilon}}^p$ introduces the nonlinearity in the evolution law. The law can be degenerated into the linear kinematic one by specifying only one $\boldsymbol{\alpha}$ component with $\gamma = 0$.

4.1.5 Damage evolution model

Based on the principle of strain equivalence (Lemaitre, 1971): "Any strain constitutive equation for a damage material may be derived in the same way as for a virgin material except that the usual stress is replaced by the effective stress," the stress tensor (in the damaged material) $\boldsymbol{\sigma}_D$ is calculated from the effective stress tensor $\boldsymbol{\sigma}$ as

$$\boldsymbol{\sigma}_D = \boldsymbol{\sigma}(1 - D) \tag{4.16}$$

where D is the damage variable, whose rate is given by Lemaitre's model (Lemaitre, 1992; Dufailly and Lemaitre, 1995)

$$\dot{D} = \begin{cases} \left[\dfrac{Y}{S}\right]^t \dot{\bar{\varepsilon}}^p & \bar{\varepsilon}^p > \bar{\varepsilon}_d^p \text{ and } \dfrac{\sigma_m}{\sigma_{eq}} > -\dfrac{1}{3} \\ 0 & \text{otherwise} \end{cases} \tag{4.17}$$

where $\sigma_m = \boldsymbol{\sigma} : \mathbf{1}/3$ is the mean stress, $\sigma_{eq} = \sqrt{3/2}\|\boldsymbol{\sigma}\|$ is the equivalent stress, σ_m/σ_{eq} is the stress triaxiality, $\bar{\varepsilon}_d^p$ is damage threshold, S is a material constant in energy density units, t is a dimensionless material constant, and Y is the internal energy density release rate, calculated as

$$Y = \frac{1}{2}\boldsymbol{\sigma} : [\mathbb{D}^e]^{-1} : \boldsymbol{\sigma} \tag{4.18}$$

4.2 Implementation of the plasticity model

In numerical analysis, the state variables of a material model such as stress, elastic and plastic strain are updated from one discrete time to the next, known as "time

integration" of state variables. Corresponding discretization and update procedure of these state variables, *i.e.,* implementation of the plasticity model is presented in this section.

4.2.1 Backward Euler difference scheme

First, the state variables are discretized using backward Euler difference scheme. Subscript i represent the step number; $(\bullet)_i$'s are variables at time t_i

$$\bar{\varepsilon}^p_{i+1} = \bar{\varepsilon}^p_i + \Delta\lambda \tag{4.19a}$$

$$\boldsymbol{\sigma}_{i+1} = \boldsymbol{\sigma}_i + \mathbb{D}^e : (\Delta\boldsymbol{\epsilon} - \Delta\boldsymbol{\epsilon}^p) \tag{4.19b}$$

$$\Delta\boldsymbol{\epsilon}^p = \frac{3}{2}\boldsymbol{n}_{i+1}\Delta\lambda \tag{4.19c}$$

$$\Delta\boldsymbol{\alpha}_j = \left[C_j\boldsymbol{n}_{i+1} - \gamma_j(\boldsymbol{\alpha}_j)_{i+1}\right]\Delta\lambda \tag{4.19d}$$

4.2.2 Elastic-plastic operator split

Next, the state variables are updated using a two-step algorithm: (1) an elastic trial predictor; followed by (2) a plastic corrector that performs projection of the trial states onto the yield surface. The elastic predictor obtains the trial elastic states by

freezing plastic flow during the time step as

$$\bar{\varepsilon}_{i+1}^{p,trial} = \bar{\varepsilon}_i^p \tag{4.20a}$$

$$\boldsymbol{\sigma}_{i+1}^{trial} = \boldsymbol{\sigma}_i + \mathbb{D}^e : \Delta\boldsymbol{\epsilon} \tag{4.20b}$$

$$\Delta\boldsymbol{\epsilon}^{p,trial} = \mathbf{0} \tag{4.20c}$$

$$\Delta\boldsymbol{\alpha}_j^{trial} = \mathbf{0} \tag{4.20d}$$

The plastic return-mapping corrector then updates the states as

$$\bar{\varepsilon}_{i+1}^p = \bar{\varepsilon}_i^{p,trial} + \Delta\lambda \tag{4.21a}$$

$$\boldsymbol{\sigma}_{i+1} = \boldsymbol{\sigma}_{i+1}^{trial} - \mathbb{D}^e : \Delta\boldsymbol{\epsilon}^p \tag{4.21b}$$

$$\Delta\boldsymbol{\epsilon}^p = \frac{3}{2}\boldsymbol{n}_{i+1}\Delta\lambda \tag{4.21c}$$

$$\Delta\boldsymbol{\alpha}_j = \left[C_j\boldsymbol{n}_{i+1} - \gamma_j(\boldsymbol{\alpha}_j)_{i+1}\right]\Delta\lambda \tag{4.21d}$$

The plastic corrector can be implemented either using the cutting-plane algorithm or the closest-point algorithm. For theory of these two algorithms, see Simo and Hughes (1998). The development of these two algorithms for the damage plasticity model is shown below.

4.2.3 Cutting-plane algorithm

For the cutting-plane algorithm, in the k-th iteration, the states are integrated from $(\bullet)^{(k)}$ to $(\bullet)^{(k+1)}$, with linearization about $(\bullet)^{(k)}$:

$$\bar{\varepsilon}_{i+1}^{p,(k+1)} = \bar{\varepsilon}_{i+1}^{p,(k)} + \Delta^2\lambda^{(k)} \tag{4.22a}$$

$$\boldsymbol{\sigma}_{i+1}^{(k+1)} = \boldsymbol{\sigma}_{i+1}^{(k)} - 3G\boldsymbol{n}_{i+1}^{(k)}\Delta^2\lambda^{(k)} \tag{4.22b}$$

$$(\boldsymbol{\alpha}_j)_{i+1}^{(k+1)} = (\boldsymbol{\alpha}_j)_{i+1}^{(k)} + \left[C_j\boldsymbol{n}_{i+1}^{(k)} - \gamma_j(\boldsymbol{\alpha}_j)_{i+1}^{(k)}\right]\Delta^2\lambda^{(k)} \tag{4.22c}$$

$$\sigma_y\left(\bar{\varepsilon}_{i+1}^{p,(k+1)}\right) \approx \sigma_y\left(\bar{\varepsilon}_{i+1}^{p,(k)}\right) + \frac{\partial\sigma_y}{\partial\bar{\varepsilon}^p}\left(\bar{\varepsilon}_{i+1}^{p,(k)}\right)\Delta^2\lambda^{(k)} \tag{4.22d}$$

Solution of the yield function

$$\begin{aligned} 0 = F_{i+1}^{(k+1)} \approx & F_{i+1}^{(k)} + \frac{\partial F}{\partial\boldsymbol{\sigma}}^{(k)}\Delta^2\boldsymbol{\sigma}_{i+1}^{(k)} + \frac{\partial F}{\partial\boldsymbol{\alpha}}^{(k)}\Delta^2\boldsymbol{\alpha}_{i+1}^{(k)} + \frac{\partial F}{\partial\sigma_y}^{(k)}\Delta^2\sigma_{y,i+1}^{(k)} \\ = & F_{i+1}^{(k)} + \frac{3}{2}\boldsymbol{n}_{i+1}^{(k)} : \left(-3G\boldsymbol{n}_{i+1}^{(k)}\Delta^2\lambda^{(k)}\right) + \frac{\partial\sigma_y}{\partial\bar{\varepsilon}^p}\left(\bar{\varepsilon}_{i+1}^{p,(k)}\right)\Delta^2\lambda^{(k)} \\ & - \frac{3}{2}\boldsymbol{n}_{i+1}^{(k)} : \left[C_j\boldsymbol{n}_{i+1}^{(k)} - \gamma_j(\boldsymbol{\alpha}_j)_{i+1}^{(k)}\right]\Delta^2\lambda^{(k)} \end{aligned} \tag{4.23}$$

obtains

$$\Delta^2\lambda^{(k)} = \frac{F_{i+1}^{(k)}}{3G + \frac{\partial\sigma_y}{\partial\bar{\varepsilon}^p}\left(\bar{\varepsilon}_{i+1}^{p,(k)}\right) + \sum_j C_j - \frac{3}{2}\boldsymbol{n}_{i+1}^{(k)} : \left[\sum_j \gamma_j(\boldsymbol{\alpha}_j)_{i+1}^{(k)}\right]} \tag{4.24}$$

Because linearization is used to update the state except for

$$\sigma_y\left(\bar{\varepsilon}_{i+1}^{p,(k+1)}\right) \approx \sigma_y\left(\bar{\varepsilon}_{i+1}^{p,(k)}\right) + \frac{\partial\sigma_y}{\partial\bar{\varepsilon}^p}\left(\bar{\varepsilon}_{i+1}^{p,(k)}\right)\Delta^2\lambda^{(k)} \tag{4.25}$$

the yield function can be calculated that

$$F_{i+1}^{(k+1)} = \sigma_y\left(\bar{\varepsilon}_{i+1}^{p,(k)}\right) + \frac{\partial\sigma_y}{\partial\bar{\varepsilon}^p}\left(\bar{\varepsilon}_{i+1}^{p,(k)}\right)\Delta^2\lambda^{(k)} - \sigma_y\left(\bar{\varepsilon}_{i+1}^{p,(k+1)}\right) \tag{4.26}$$

If the isotropic hardening function $\sigma_y\left(\bar{\varepsilon}^p\right)$ is defined using piecewise linear curve, and $\Delta^2\lambda^{(0)}$ is small enough, the linearization of σ_y is accurate. Then, the error of $F_{i+1}^{(1)}$ above may be ignored. This leads to a non-iterative algorithm:

$$\Delta\lambda = \Delta^2\lambda^{(0)} = \frac{F_{i+1}^{trial}}{k} \tag{4.27}$$

where

$$k = 3G + \frac{\partial\sigma_y}{\partial\bar{\varepsilon}^p}\left(\bar{\varepsilon}_i^p\right) + \sum_j C_j - \frac{3}{2}\boldsymbol{n}_{i+1}^{trial} : \left[\sum_j \gamma_j(\boldsymbol{\alpha}_j)_i\right] \tag{4.28}$$

whereby the states are updated as

$$\bar{\varepsilon}_{i+1}^p = \bar{\varepsilon}_i^p + \Delta\lambda \tag{4.29a}$$

$$\boldsymbol{\sigma}_{i+1} = \boldsymbol{\sigma}_{i+1}^{trial} - 3G\boldsymbol{n}_{i+1}^{trial}\Delta\lambda \tag{4.29b}$$

$$(\boldsymbol{\alpha}_j)_{i+1} = (\boldsymbol{\alpha}_j)_i + \left[C_j\boldsymbol{n}_{i+1}^{trial} - \gamma_j(\boldsymbol{\alpha}_j)_i\right]\Delta\lambda \tag{4.29c}$$

And because

$$\frac{\partial\Delta\lambda}{\partial\boldsymbol{\epsilon}_{i+1}} = \frac{1}{k}\left\{3G\boldsymbol{n}_{i+1}^{trial} + \frac{3}{2}\Delta\lambda\frac{\partial\boldsymbol{n}_{i+1}^{trial}}{\partial\boldsymbol{\epsilon}_{i+1}} : \left[\sum_j \gamma_j(\boldsymbol{\alpha}_j)_i\right]\right\} \tag{4.30}$$

where

$$\begin{aligned}\frac{\partial\boldsymbol{n}_{i+1}^{trial}}{\partial\boldsymbol{\epsilon}_{i+1}} = \frac{\partial\boldsymbol{n}_{i+1}^{trial}}{\partial\boldsymbol{s}_{e,i+1}^{trial}} : \frac{\partial\boldsymbol{s}_{e,i+1}^{trial}}{\partial\boldsymbol{\epsilon}_{i+1}} &= \frac{\mathbb{I} - \frac{3}{2}\boldsymbol{n}_{i+1}^{trial}\otimes\boldsymbol{n}_{i+1}^{trial}}{\bar{\sigma}_{i+1}^{trial}} : \left[2G\left(\mathbb{I} - \frac{1}{3}\mathbf{1}\otimes\mathbf{1}\right)\right] \\ &= \frac{2G}{\bar{\sigma}_{i+1}^{trial}}\left(\mathbb{I} - \frac{1}{3}\mathbf{1}\otimes\mathbf{1} - \frac{3}{2}\boldsymbol{n}_{i+1}^{trial}\otimes\boldsymbol{n}_{i+1}^{trial}\right)\end{aligned} \tag{4.31}$$

then from

$$\boldsymbol{\sigma}_{i+1} = \boldsymbol{\sigma}_{i+1}^{trial} - 3G\boldsymbol{n}_{i+1}^{trial}\Delta\lambda \tag{4.32a}$$

$$\mathrm{d}\boldsymbol{\sigma}_{i+1} = \mathbb{D}^e : \mathrm{d}\boldsymbol{\epsilon}_{i+1} - 3G[\boldsymbol{n}_{i+1}^{trial}\mathrm{d}\Delta\lambda + \mathrm{d}\boldsymbol{n}_{i+1}^{trial}\Delta\lambda] \tag{4.32b}$$

$$= \left[\mathbb{D}^e - 3G\boldsymbol{n}_{i+1}^{trial}\otimes\frac{\partial\Delta\lambda}{\partial\boldsymbol{\epsilon}_{i+1}} - 3G\Delta\lambda\frac{\partial\boldsymbol{n}_{i+1}^{trial}}{\partial\boldsymbol{\epsilon}_{i+1}}\right] : \mathrm{d}\boldsymbol{\epsilon}_{i+1} \tag{4.32c}$$

the algorithm consistent tangent moduli can be obtained as

$$\frac{\partial \boldsymbol{\sigma}_{i+1}}{\partial \boldsymbol{\epsilon}_{i+1}} = \mathbb{D}_{i+1} = \kappa \mathbf{1} \otimes \mathbf{1} + 2G\theta_{i+1}(\mathbb{I} - \frac{1}{3}\mathbf{1} \otimes \mathbf{1}) - 3G\tilde{\theta}_{i+1}\boldsymbol{n}_{i+1}^{trial} \otimes \boldsymbol{n}_{i+1}^{trial} - \tilde{\mathbb{D}}_{i+1} \quad (4.33)$$

where

$$\theta_{i+1} = 1 - \frac{3G\Delta\lambda}{\bar{\sigma}_{i+1}^{trial}} \quad (4.34a)$$

$$\tilde{\theta}_{i+1} = \frac{3G}{k} - (1 - \theta_{i+1}) \quad (4.34b)$$

$$\tilde{\mathbb{D}}_{i+1} = \frac{9G^2\Delta\lambda}{k\bar{\sigma}_{i+1}^{trial}}\boldsymbol{n}_{i+1}^{trial} \otimes \left\{ \left[\mathbb{I} - \frac{3}{2}\boldsymbol{n}_{i+1}^{trial} \otimes \boldsymbol{n}_{i+1}^{trial} \right] : \left[\sum_j \gamma_j (\boldsymbol{\alpha}_j)_i \right] \right\} \quad (4.34c)$$

4.2.4 Closest-point projection algorithm

For the closest-point projection algorithm, in iteration number k, the states are integrated from $(\bullet)^{(0)}$ to $(\bullet)^{(k)}$, with linearization about $(\bullet)^{(k)}$:

$$\bar{\varepsilon}_{i+1}^{p,(k)} = \bar{\varepsilon}_i^p + \Delta\lambda^{(k)} \quad (4.35a)$$

$$\boldsymbol{s}_{i+1}^{(k)} = \boldsymbol{s}_{i+1}^{trial} - 3G\boldsymbol{n}_{i+1}^{(k)}\Delta\lambda^{(k)} \quad (4.35b)$$

$$(\boldsymbol{\alpha}_j)_{i+1}^{(k)} = (\boldsymbol{\alpha}_j)_i + \left[C_j \boldsymbol{n}_{i+1}^{(k)} - \gamma_j (\boldsymbol{\alpha}_j)_{i+1}^{(k)} \right] \Delta\lambda^{(k)} \quad (4.35c)$$

resulting in

$$\begin{aligned} \boldsymbol{s}_{e,i+1}^{(k)} &= \boldsymbol{s}_{i+1}^{(k)} - \boldsymbol{\alpha}_{i+1}^{(k)} \\ &= \left[\boldsymbol{s}_{i+1}^{trial} - \sum_j \frac{(\boldsymbol{\alpha}_j)_i}{1 + \gamma_j \Delta\lambda^{(k)}} \right] - \left[3G + \sum_j \frac{C_j}{1 + \gamma_j \Delta\lambda^{(k)}} \right] \Delta\lambda^{(k)} \boldsymbol{n}_{i+1}^{(k)} \\ &= \boldsymbol{\xi}_{i+1}^{(k)} - \left[3G + \sum_j \frac{C_j}{1 + \gamma_j \Delta\lambda^{(k)}} \right] \Delta\lambda^{(k)} \boldsymbol{n}_{i+1}^{(k)} \end{aligned} \quad (4.36)$$

where

$$\boldsymbol{\xi}_{i+1}^{(k)} = \boldsymbol{s}_{i+1}^{trial} - \sum_j \frac{(\boldsymbol{\alpha}_j)_i}{1+\gamma_j \Delta\lambda^{(k)}} \tag{4.37}$$

From the yield function

$$0 = F_{i+1}^{(k)} = \bar{\sigma}_{i+1}^{(k)} - \sigma_y\left(\bar{\varepsilon}_{i+1}^{p,(k)}\right) \tag{4.38}$$

obtain

$$\boldsymbol{s}_{e,i+1}^{(k)} = \bar{\sigma}_{i+1}^{(k)} \boldsymbol{n}_{i+1}^{(k)} = \sigma_y\left(\bar{\varepsilon}_{i+1}^{p,(k)}\right) \boldsymbol{n}_{i+1}^{(k)} \tag{4.39}$$

Hence, the direction $\boldsymbol{n}_{i+1}^{(k)}$ is determined exclusively in terms of $\boldsymbol{\xi}_{i+1}^{(k)}$

$$\boldsymbol{n}_{i+1}^{(k)} = \frac{\boldsymbol{\xi}_{i+1}^{(k)}}{\tilde{\sigma}_{i+1}^{(k)}} \quad \text{where} \quad \tilde{\sigma}_{i+1}^{(k)} = \sqrt{\frac{3}{2}}\left\|\boldsymbol{\xi}_{i+1}^{(k)}\right\| \tag{4.40}$$

Therefore,

$$\sigma_y\left(\bar{\varepsilon}_{i+1}^{p,(k)}\right) \boldsymbol{n}_{i+1}^{(k)} = \tilde{\sigma}_{i+1}^{(k)} \boldsymbol{n}_{i+1}^{(k)} - \left[3G + \sum_j \frac{C_j}{1+\gamma_j \Delta\lambda^{(k)}}\right] \Delta\lambda^{(k)} \boldsymbol{n}_{i+1}^{(k)} \tag{4.41}$$

and the following nonlinear scalar equation is obtained

$$0 = g\left(\Delta\lambda^{(k)}\right) = \tilde{\sigma}_{i+1}^{(k)} - \left[3G + \sum_j \frac{C_j}{1+\gamma_j \Delta\lambda^{(k)}}\right] \Delta\lambda^{(k)} - \sigma_y\left(\bar{\varepsilon}_{i+1}^{p,(k)}\right) \tag{4.42}$$

and

$$\begin{aligned} \frac{\partial g}{\partial \Delta\lambda}\left(\Delta\lambda^{(k)}\right) = & \frac{3}{2}\boldsymbol{n}_{i+1}^{(k)} : \left[\sum_j \frac{\gamma_j (\boldsymbol{\alpha}_j)_i}{\left(1+\gamma_j \Delta\lambda^{(k)}\right)^2}\right] \\ & - 3G - \sum_j \frac{C_j}{\left(1+\gamma_j \Delta\lambda^{(k)}\right)^2} - \frac{\partial \sigma_y}{\partial \bar{\varepsilon}^p}\left(\bar{\varepsilon}_{i+1}^{p,(k)}\right) \end{aligned} \tag{4.43}$$

Advancing to the next iteration by Newton's method

$$\Delta\lambda^{(k+1)} = \Delta\lambda^{(k)} - \left[\frac{\partial g}{\partial \Delta\lambda}\left(\Delta\lambda^{(k)}\right)\right]^{-1} g\left(\Delta\lambda^{(k)}\right) \tag{4.44}$$

After convergence, the states are updated as

$$\bar{\varepsilon}^p_{i+1} = \bar{\varepsilon}^p_i + \Delta\lambda^{(k+1)} \tag{4.45a}$$

$$\boldsymbol{s}_{i+1} = \boldsymbol{s}^{trial}_{i+1} - 3G\boldsymbol{n}^{(k+1)}_{i+1}\Delta\lambda^{(k+1)} \tag{4.45b}$$

$$(\boldsymbol{\alpha}_j)_{i+1} = \frac{(\boldsymbol{\alpha}_j)_i + C_j\Delta\lambda^{(k+1)}\boldsymbol{n}^{(k+1)}_{i+1}}{1+\gamma_j\Delta\lambda^{(k+1)}} \tag{4.45c}$$

Because $\boldsymbol{\epsilon}_{i+1}$ is fixed in plastic corrector

$$\begin{aligned} 0 = \frac{\partial g}{\partial \boldsymbol{\epsilon}_{i+1}} &= \frac{\partial g}{\partial \Delta\lambda}(\Delta\lambda)\ \frac{\partial \Delta\lambda}{\partial \boldsymbol{\epsilon}_{i+1}} + \frac{\partial g}{\partial \boldsymbol{s}^{trial}_{i+1}} : \frac{\partial \boldsymbol{s}^{trial}_{i+1}}{\partial \boldsymbol{\epsilon}_{i+1}} \\ &= \frac{\partial g}{\partial \Delta\lambda}(\Delta\lambda)\ \frac{\partial \Delta\lambda}{\partial \boldsymbol{\epsilon}_{i+1}} + \frac{3}{2}\boldsymbol{n}_{i+1} : 2G\left(\mathbb{I} - \frac{1}{3}\mathbf{1}\otimes\mathbf{1}\right) \\ &= \frac{\partial g}{\partial \Delta\lambda}(\Delta\lambda)\ \frac{\partial \Delta\lambda}{\partial \boldsymbol{\epsilon}_{i+1}} + 3G\boldsymbol{n}_{i+1} \end{aligned} \tag{4.46}$$

So$\dfrac{\partial \Delta\lambda}{\partial \boldsymbol{\epsilon}_{i+1}} = \dfrac{3G}{k}\boldsymbol{n}_{i+1}$, where $k = -\dfrac{\partial g}{\partial \Delta\lambda}(\Delta\lambda)$.

Then from

$$\begin{aligned} &\frac{\partial \boldsymbol{n}_{i+1}}{\partial \boldsymbol{\epsilon}_{i+1}} = \frac{\partial \boldsymbol{n}_{i+1}}{\partial \boldsymbol{\xi}_{i+1}} : \frac{\partial \boldsymbol{\xi}_{i+1}}{\partial \boldsymbol{\epsilon}_{i+1}} \\ =&\frac{\mathbb{I} - \dfrac{3}{2}\boldsymbol{n}_{i+1}\otimes\boldsymbol{n}_{i+1}}{\tilde{\sigma}_{i+1}} : \left[2G\left(\mathbb{I} - \frac{1}{3}\mathbf{1}\otimes\mathbf{1}\right) + \sum_j \frac{\gamma_j(\boldsymbol{\alpha}_j)_i}{(1+\gamma_j\Delta\lambda)^2}\otimes\frac{\partial\Delta\lambda}{\partial\boldsymbol{\epsilon}_{i+1}}\right] \\ =&\frac{\mathbb{I} - \dfrac{3}{2}\boldsymbol{n}_{i+1}\otimes\boldsymbol{n}_{i+1}}{\tilde{\sigma}_{i+1}} : \left[2G\left(\mathbb{I} - \frac{1}{3}\mathbf{1}\otimes\mathbf{1}\right) + \frac{3G}{k}\sum_j \frac{\gamma_j(\boldsymbol{\alpha}_j)_i\otimes\boldsymbol{n}_{i+1}}{(1+\gamma_j\Delta\lambda)^2}\right] \\ =&\frac{2G}{\tilde{\sigma}_{i+1}}\left(\mathbb{I} - \frac{1}{3}\mathbf{1}\otimes\mathbf{1} - \frac{3}{2}\boldsymbol{n}_{i+1}\otimes\boldsymbol{n}_{i+1}\right) \\ &+ \frac{3G}{k\tilde{\sigma}_{i+1}}\left[\mathbb{I} - \frac{3}{2}\boldsymbol{n}_{i+1}\otimes\boldsymbol{n}_{i+1}\right] : \left[\sum_j \frac{\gamma_j(\boldsymbol{\alpha}_j)_i\otimes\boldsymbol{n}_{i+1}}{(1+\gamma_j\Delta\lambda)^2}\right] \end{aligned} \tag{4.47}$$

and

$$\boldsymbol{\sigma}_{i+1} = \boldsymbol{\sigma}_{i+1}^{trial} - 3G\boldsymbol{n}_{i+1}\Delta\lambda \tag{4.48a}$$

$$\mathrm{d}\boldsymbol{\sigma}_{i+1} = \mathbb{D}^{el} : \mathrm{d}\boldsymbol{\epsilon}_{i+1} - 3G[\boldsymbol{n}_{i+1}\mathrm{d}\Delta\lambda + \mathrm{d}\boldsymbol{n}_{i+1}\Delta\lambda] \tag{4.48b}$$

$$= \left[\mathbb{D}^{el} - 3G\boldsymbol{n}_{i+1} \otimes \frac{\partial\Delta\lambda}{\partial\boldsymbol{\epsilon}_{i+1}} - 3G\Delta\lambda\frac{\partial\boldsymbol{n}_{i+1}}{\partial\boldsymbol{\epsilon}_{i+1}}\right] : \mathrm{d}\boldsymbol{\epsilon}_{i+1} \tag{4.48c}$$

the algorithm consistent tangent moduli is obtained as

$$\frac{\partial\boldsymbol{\sigma}_{i+1}}{\partial\boldsymbol{\epsilon}_{i+1}} = \mathbb{D}_{i+1} = \kappa\mathbf{1}\otimes\mathbf{1} + 2G\theta_{i+1}(\mathbb{I} - \frac{1}{3}\mathbf{1}\otimes\mathbf{1}) - 3G\tilde{\theta}_{i+1}\boldsymbol{n}_{i+1}\otimes\boldsymbol{n}_{i+1} - \tilde{\mathbb{D}}_{i+1} \tag{4.49}$$

where

$$\theta_{i+1} = 1 - \frac{3G\Delta\lambda}{\tilde{\sigma}_{i+1}} \tag{4.50a}$$

$$\tilde{\theta}_{i+1} = \frac{3G}{k} - (1 - \theta_{i+1}) \tag{4.50b}$$

$$\tilde{\mathbb{D}}_{i+1} = \frac{9G^2\Delta\lambda}{k\tilde{\sigma}_{i+1}}\left[\mathbb{I} - \frac{3}{2}\boldsymbol{n}_{i+1}\otimes\boldsymbol{n}_{i+1}\right] : \left[\sum_j \frac{\gamma_j(\boldsymbol{\alpha}_j)_i \otimes \boldsymbol{n}_{i+1}}{(1+\gamma_j\Delta\lambda)^2}\right] \tag{4.50c}$$

4.3 Implementation of the damage model

The damage state is updated using a trapezoidal scheme

$$\Delta D_i = \frac{1}{2}\left[\left(\frac{Y_i}{S}\right)^t + \left(\frac{Y_{i+1}}{S}\right)^t\right]\Delta\bar{\varepsilon}_i^p \tag{4.51}$$

where

$$Y_i = \frac{1}{2}\boldsymbol{\sigma}_i : [\mathbb{D}^e]^{-1} : \boldsymbol{\sigma}_i \tag{4.52}$$

The stress in the damaged material is then updated as

$$\boldsymbol{\sigma}_{D,i+1} = \boldsymbol{\sigma}_{i+1}(1 - D_{i+1}) \tag{4.53}$$

Because of major symmetry of elastic moduli, the algorithm consistent tangent moduli for the stress (in the damaged material) is derived as follows:

$$\begin{aligned}\frac{\partial Y_{i+1}}{\partial \boldsymbol{\epsilon}_{i+1}} &= \frac{1}{2}\boldsymbol{\sigma}_{i+1} : \left[\mathbb{D}^e\right]^{-1} : \frac{\partial \boldsymbol{\sigma}_{i+1}}{\partial \boldsymbol{\epsilon}_{i+1}} + \frac{1}{2}\frac{\partial \boldsymbol{\sigma}_{i+1}}{\partial \boldsymbol{\epsilon}_{i+1}} : \left[\mathbb{D}^e\right]^{-1} : \boldsymbol{\sigma}_{i+1} \\ &= \boldsymbol{\sigma}_{i+1} : \left[\mathbb{D}^e\right]^{-1} : \frac{\partial \boldsymbol{\sigma}_{i+1}}{\partial \boldsymbol{\epsilon}_{i+1}}\end{aligned} \tag{4.54}$$

then

$$\begin{aligned}\frac{\partial \Delta D_i}{\partial \boldsymbol{\epsilon}_{i+1}} &= \frac{1}{2}\left[\left(\frac{Y_i}{S}\right)^t + \left(\frac{Y_{i+1}}{S}\right)^t\right]\frac{\partial \Delta\lambda}{\partial \boldsymbol{\epsilon}_{i+1}} + \frac{t}{2}\left(\frac{Y_{i+1}}{S}\right)^{t-1}\frac{1}{S}\Delta\lambda\frac{\partial Y_{i+1}}{\partial \boldsymbol{\epsilon}_{i+1}} \\ =&\frac{1}{2}\left[\left(\frac{Y_i}{S}\right)^t + \left(\frac{Y_{i+1}}{S}\right)^t\right]\frac{\partial \Delta\lambda}{\partial \boldsymbol{\epsilon}_{i+1}} + \frac{t\Delta\lambda}{2S}\left(\frac{Y_{i+1}}{S}\right)^{t-1}\boldsymbol{\sigma}_{i+1} : \left[\mathbb{D}^e\right]^{-1} : \frac{\partial \boldsymbol{\sigma}_{i+1}}{\partial \boldsymbol{\epsilon}_{i+1}}\end{aligned} \tag{4.55}$$

and finally

$$\frac{\partial \boldsymbol{\sigma}_{D,i+1}}{\partial \boldsymbol{\epsilon}_{i+1}} = \frac{\partial \boldsymbol{\sigma}_{i+1}}{\partial \boldsymbol{\epsilon}_{i+1}}(1 - D_{i+1}) - \boldsymbol{\sigma}_{i+1} \otimes \frac{\partial \Delta D_i}{\partial \boldsymbol{\epsilon}_{i+1}} \tag{4.56}$$

4.4 Time integration examples

The pseudo-code for the time integration procedure using non-iterative cutting-plane algorithm for brick and shell elements is listed step-by-step below. For the sake of simplicity and clarity, there is only one back stress tensor component and isotropic hardening is not included. The complete cyclic damage plasticity model with two back stress tensor components, piecewise linear isotropic hardening, and damage evolution was implemented as LS-DYNA MAT_153 (MAT_DAMAGE_3, LSTC, 2007). A simplified version with one back stress tensor component, linear isotropic hardening, and critical equivalent plastic strain damage criterion was implemented as LS-DYNA MAT_165 (MAT_PLASTIC_NONLINEAR_KINEMATIC, LSTC, 2007).

4.4.1 Integration procedure for brick elements

1. Compute incremental average strain

$$\Delta\varepsilon_{avg} = \frac{\Delta\varepsilon_1 + \Delta\varepsilon_2 + \Delta\varepsilon_3}{3} \tag{4.57}$$

2. Compute incremental hydrostatic stress

$$\Delta p = 3K\Delta\varepsilon_{avg} \tag{4.58}$$

3. Compute trial stress $\boldsymbol{\sigma}^{trial}$

$$\sigma_i^{trial} = \sigma_i + \Delta p + 2G\left(\Delta\varepsilon_i - \Delta\varepsilon_{avg}\right) \qquad (i = 1, 2, 3) \tag{4.59a}$$

$$\sigma_i^{trial} = \sigma_i + \Delta p + G\Delta\varepsilon_i \qquad (i = 4, 5, 6) \tag{4.59b}$$

4. Compute trial hydrostatic stress

$$p^{trial} = \frac{\sigma_1^{trial} + \sigma_2^{trial} + \sigma_3^{trial}}{3} \tag{4.60}$$

5. Compute trial deviatoric effective stress $\boldsymbol{s}_e^{trial}$

$$\begin{aligned} s_{e,i}^{trial} &= \sigma_i^{trial} - p^{trial} - \alpha_i \quad (i = 1, 2, 3) \\ s_{e,i}^{trial} &= \sigma_i^{trial} - \alpha_i \qquad\qquad (i = 4, 5, 6) \end{aligned} \tag{4.61}$$

6. Compute second invariant of trial effective deviatoric stress

$$J_2^{trial} = \frac{\left(s_{e,1}^{trial}\right)^2 + \left(s_{e,2}^{trial}\right)^2 + \left(s_{e,3}^{trial}\right)^2}{2} + \left(s_{e,4}^{trial}\right)^2 + \left(s_{e,5}^{trial}\right)^2 + \left(s_{e,6}^{trial}\right)^2 \tag{4.62}$$

7. Compute trial Mises stress

$$\bar{\sigma}^{trial} = \sqrt{3J_2^{trial}} \tag{4.63}$$

8. Compute flow direction $\boldsymbol{n}$

$$n_i = \frac{s_{e,i}^{trial}}{\bar{\sigma}^{trial}} \quad (i = 1, 2, 3, 4, 5, 6) \tag{4.64}$$

9. Compute equivalent plastic strain increment

$$\Delta\bar{\varepsilon}^p = \frac{\bar{\sigma}^{trial} - \sigma_y}{3G + C - \frac{3}{2}\gamma\left(\sum_{i=1}^{3} n_i\alpha_i + \sum_{i=4}^{6} 2n_i\alpha_i\right)} \tag{4.65}$$

10. Update total equivalent plastic strain

$$\bar{\varepsilon}^p = \bar{\varepsilon}^p + \Delta\bar{\varepsilon}^p \tag{4.66}$$

11. Update back stress $\boldsymbol{\alpha}$

$$\alpha_i = \alpha_i + (Cn_i - \gamma\alpha_i)\,\Delta\bar{\varepsilon}^p \quad (i = 1, 2, 3, 4, 5, 6) \tag{4.67}$$

12. Update stress $\boldsymbol{\sigma}$

$$\sigma_i = \sigma_i^{trial} - 3Gn_i\Delta\bar{\varepsilon}^p \quad (i = 1, 2, 3, 4, 5, 6) \tag{4.68}$$

4.4.2 Integration procedure for shell elements

1. For plane stress iteration number $j = 1$, compute fully elastic normal strain

$$\varepsilon_3^{(1)} = -\frac{\nu}{1-\nu}\left(\varepsilon_1 + \varepsilon_2\right) \tag{4.69}$$

2. Follow the procedure of brick element and compute normal stress $\sigma_3^{(i)}$;

3. For iteration number $j = 2$, compute fully plastic normal strain

$$\varepsilon_3^{(2)} = -(\varepsilon_1 + \varepsilon_2) \tag{4.70}$$

4. Follow the procedure of brick element and compute normal stress $\sigma_3^{(i)}$;

5. Compute estimated normal strain

$$\varepsilon_3^{(j+1)} = \varepsilon_3^{(j-1)} - \frac{\varepsilon_3^{(j)} - \varepsilon_3^{(j-1)}}{\sigma_3^{(j)} - \sigma_3^{(j-1)}} \sigma_3^{(j-1)} \tag{4.71}$$

6. Compare $\varepsilon_3^{(j)}$ and $\varepsilon_3^{(j+1)}$, check convergence and check normal stress condition $\sigma_3^{(j)} = 0$; if either check does not satisfy its tolerance, increase j, and go to step 4.

7. Update state.

4.5 Concluding remarks

The theory, implementation, and examples of the cyclic damage plasticity models are discussed in detailed. The model was implemented by the author in finite element software LS-DYNA as Material 153 (MAT_DAMAGE_3, LSTC, 2007). This newly developed material model is used in the following chapters.

Chapter 5

Calibration, Validation and Application

This chapter focusses on calibration, validation and application of the new damage material model using experimental results from beam-to-column connections, individual braces, and braced frame subassemblies. Material calibration procedures using monotonic and cyclic experimental data is discussed, followed by the application of the calibrated material model to components and subassemblies of steel braced frame.

5.1 Material calibration

The material model developed in Chapter 4 has several plasticity and damage properties. These properties can be calibrated using monotonic and/or cyclic experimental data, discussed as following.

5.1.1 Calibration using monotonic data

For monotonic loading in uniaxial tension test, the stress-plastic strain curve represented by the model is given by

$$\sigma = \sigma_y + \frac{C_1}{\gamma_1}\left[1 - \exp\left(-\gamma_1 \varepsilon^p\right)\right] + \frac{C_2}{\gamma_2}\left[1 - \exp\left(-\gamma_2 \varepsilon^p\right)\right] + H\varepsilon^p \tag{5.1}$$

where σ is the uniaxial stress, ε^p is the uniaxial plastic strain, σ_y is the initial yield stress, C_1, γ_1, C_2, and γ_2 are kinematic hardening parameters, and H is linear isotropic hardening parameter. If $\gamma_i = 0$, the nonlinear term $\dfrac{C_i}{\gamma_i}\left[1 - \exp\left(-\gamma_i \varepsilon^p\right)\right]$ is reduced to a linear term $C_i \varepsilon^p$. Equation (5.1) may be used to determine the plasticity parameters if only monotonic tension test data is available.

The physical meaning of kinematic hardening parameters C_1 and γ_1 can be illustrated by specifying $C_2 = H = 0$; then Equation (5.1) becomes

$$\sigma = \sigma_y + \frac{C_1}{\gamma_1}\left[1 - \exp\left(-\gamma_1 \varepsilon^p\right)\right] \tag{5.2}$$

making the initial slope (derivative $\left.\dfrac{\partial \sigma}{\partial \varepsilon^p}\right|_{\varepsilon^p = 0}$) equal to C_1, and the saturated yield stress equal to $\sigma_y + C_1/\gamma_1$ (Figure 5.1).

5.1.2 Calibration using cyclic data

For uniaxial stress cyclic loading, the evolution of back stress is given by

$$\dot{\alpha}_i = C_i \dot{\varepsilon}^p - \gamma_i \alpha \left|\dot{\varepsilon}^p\right| = -\left(\alpha - nC_i/\gamma_i\right) n\gamma_i \dot{\varepsilon}^p \tag{5.3}$$

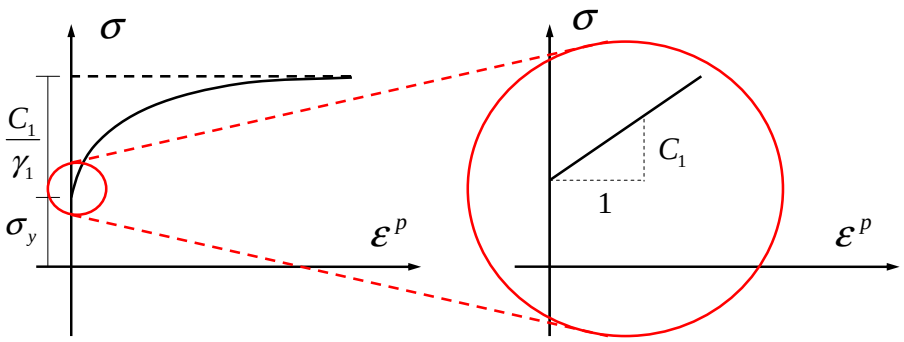

Figure 5.1: Illustration of kinematic hardening parameters

where α_i's are the uniaxial back stress components, $\dot{\varepsilon}^p$ is the uniaxial plastic strain rate, and $n = \text{sign}(\dot{\varepsilon}^p)$ is the plastic flow direction. Equation (5.3) is transformed as

$$\frac{\dot{\alpha}_i}{\alpha_i - nC_i/\gamma_i} = -n\gamma_i\dot{\varepsilon}^p \tag{5.4}$$

If the plastic strain increases or decreases monotonically, direction n is constant. Integration of Equation (5.4) results in

$$\ln\frac{\alpha_i - nC_i/\gamma_i}{\alpha_{i0} - nC_i/\gamma_i} = -n\gamma_i\left(\varepsilon^p - \varepsilon_0^p\right) \tag{5.5}$$

where the subscripts 0 denote the initial values. Equation (5.5) can be written as

$$\alpha_i = nC_i/\gamma_i + (\alpha_{i0} - nC_i/\gamma_i)\exp\left[-n\gamma_i\left(\varepsilon^p - \varepsilon_0^p\right)\right] \tag{5.6}$$

For a stabilized symmetric cycle, the amplitude and peaks of back stress are $\Delta\alpha_i/2$ and $\pm\Delta\alpha_i/2$, respectively. Similarly, the amplitude and peaks of plastic strain are $\Delta\varepsilon^p/2$ and $\pm\Delta\varepsilon^p/2$, respectively. Substitute them into Equation (5.5) and obtain

$$\frac{\Delta\alpha_i/2 - nC_i/\gamma_i}{-\Delta\alpha_i/2 - nC_i/\gamma_i} = \frac{1}{\exp\left[2\left(\gamma_i\Delta\varepsilon^p/2\right)\right]} \tag{5.7}$$

which leads to the relation between back stress and plastic strain amplitudes

$$\frac{\Delta\alpha_i}{2} = \frac{C_i}{\gamma_i}\tanh\left(\gamma_i\frac{\Delta\varepsilon^p}{2}\right) \tag{5.8}$$

For the tension half cycle, direction $n = 1$, then Equation (5.6) becomes

$$\alpha_i = \frac{C_i}{\gamma_i} - \left[\frac{C_i}{\gamma_i}\tanh\left(\gamma_i\frac{\Delta\varepsilon^p}{2}\right) + \frac{C_i}{\gamma_i}\right]\exp\left[-\gamma_i\left(\varepsilon^p + \frac{\Delta\varepsilon^p}{2}\right)\right] \tag{5.9}$$

For the tension half cycle of a stabilized symmetric cycle, when the cyclic hardening is saturated, the stress-plastic strain curve is given by

$$\begin{aligned}\sigma = \sigma_y' &+ \frac{C_1}{\gamma_1} - \left[\frac{C_1}{\gamma_1}\tanh\left(\gamma_1\frac{\Delta\varepsilon^p}{2}\right) + \frac{C_1}{\gamma_1}\right]\exp\left[-\gamma_1\left(\varepsilon^p + \frac{\Delta\varepsilon^p}{2}\right)\right] \\ &+ \frac{C_2}{\gamma_2} - \left[\frac{C_2}{\gamma_2}\tanh\left(\gamma_2\frac{\Delta\varepsilon^p}{2}\right) + \frac{C_2}{\gamma_2}\right]\exp\left[-\gamma_2\left(\varepsilon^p + \frac{\Delta\varepsilon^p}{2}\right)\right]\end{aligned} \tag{5.10}$$

Equation (5.10) may be used to determine the kinematic hardening parameters using cyclic test data. Then, isotropic hardening parameters can be obtained by removing the kinematic hardening part of stress-equivalent plastic strain curve. The material properties may be further adjusted by running numerical tests and using a least square nonlinear fitting process to improve fidelity.

The above calibration process may result in widely different sets of kinematic hardening parameters (C_1, γ_1, C_2, and γ_2) depending upon the strain range of interest. Interest in response with a larger range of strain tends to result in lower kinematic hardening modules. Using a series of material tests of Japanese SM490 steel (Fujimoto *et al.,* 1985) and SS440 steel (Nishimura *et al.,* 1994) as examples, calibration results in two sets of parameters. Parameters in Set A are $C_1 = 30000$, $\gamma_1 = 300$, $C_2 = 2000$,

and $\gamma_2 = 15$, and parameters in Set B are $C_1 = 4000$, $\gamma_1 = 400$, $C_2 = 500$, and $\gamma_2 = 0$. The results are shown in Figures 5.2 to 5.5 for SM490 steel and Figures 5.6 to 5.9 for SS440 steel, both for cases of cyclic loading. Compared to the experimental results, the numerical results predicted by parameters in Set A are more accurate than those in Set B, in which the ranges of strain are relative small. For larger ranges of strain, however, the numerical results presented with the parameters in Set A are not as good as those in Set B. This is demonstrated in Figure 5.10, which compares results for monotonic tensile tests. Thus, there are two options; a user may choose Set A for the pleasing round corners during smaller strain cycles, or Set B for better agreement during larger strain cycles or monotonic straining. Other sets of parameters may be determined by "trial and error" to provide a balance of characteristics more appropriate for a particular application.

The best method of calibrating damage parameters is unknown because of current lack of detailed low-cycle fatigue data. Additional research and material testing is needed.

If no specific input is provided by the user, "default" values are provided in the implementation of the damage plasticity model to maintain backward compatibility with LS-DYNA Material 104 (LSTC, 2007). The "default" values for S and t are $\sigma_y/200$ and 1, respectively, where σ_y is the initial yield stress. The effect of different values of parameter t on the rate of deterioration can be seen in the simulated Manson-Coffin curves plotted in Figure 3.9.

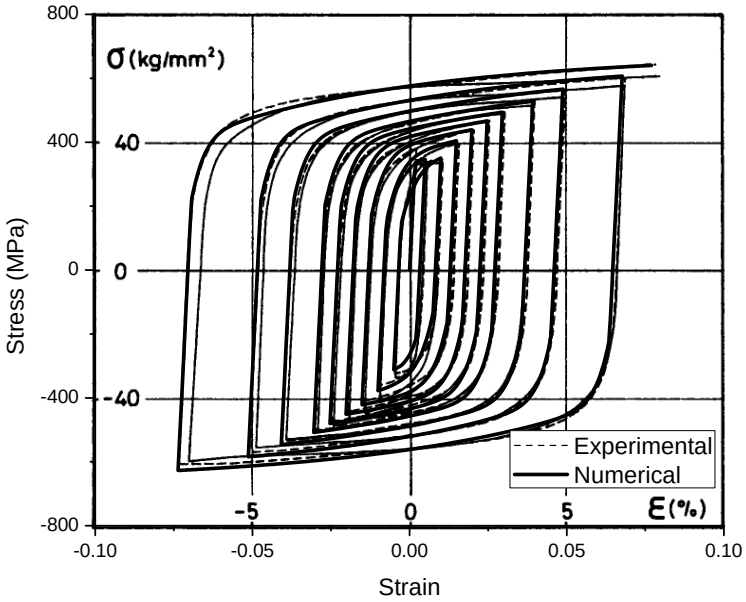

(a) Parameters Set A

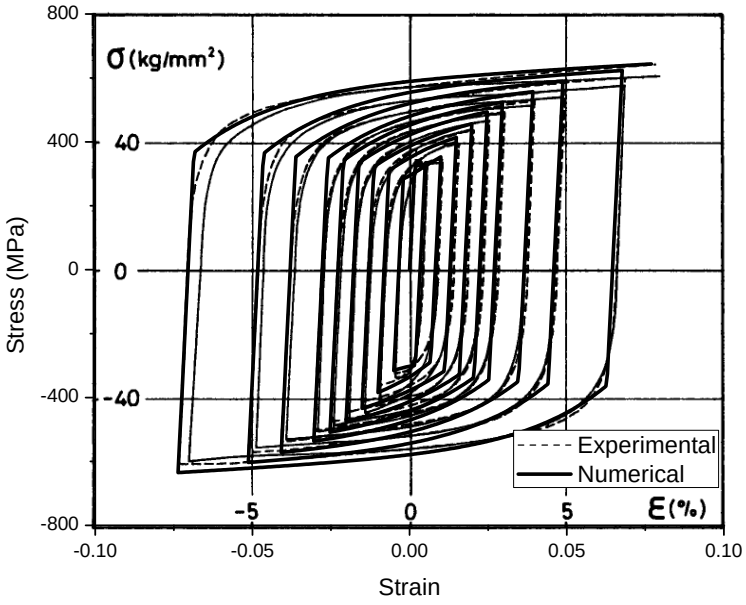

(b) Parameters Set B

[Experimental results by Fujimoto *et al.* (1985)]

Figure 5.2: Experimental versus numerical results (SM490 cyclic test 1)

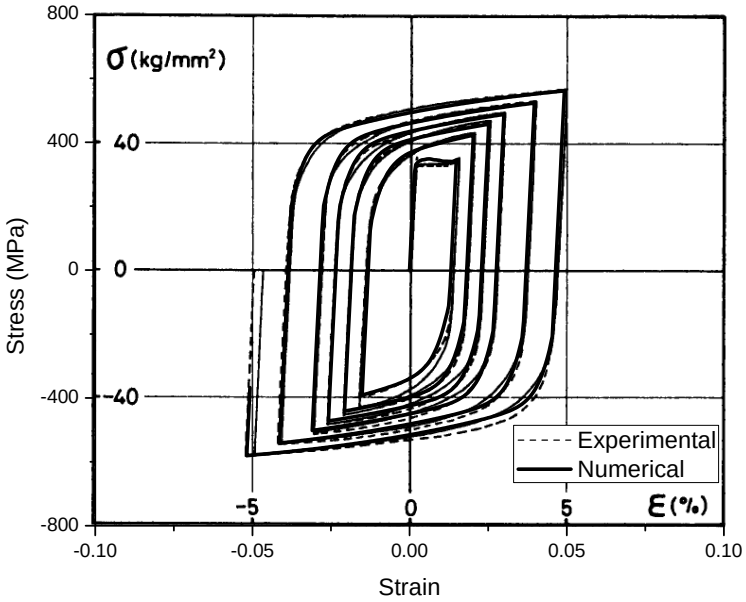

(a) Parameters Set A

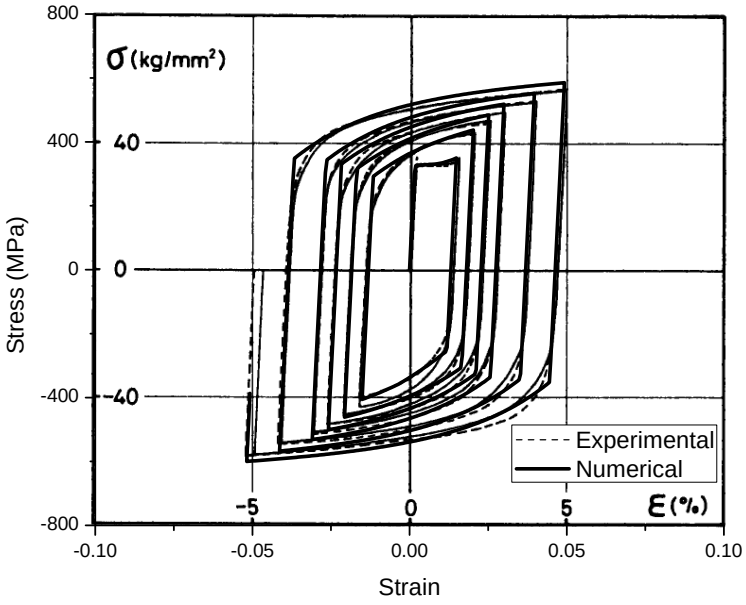

(b) Parameters Set B

[Experimental results by Fujimoto *et al.* (1985)]

Figure 5.3: Experimental versus numerical results (SM490 cyclic test 2)

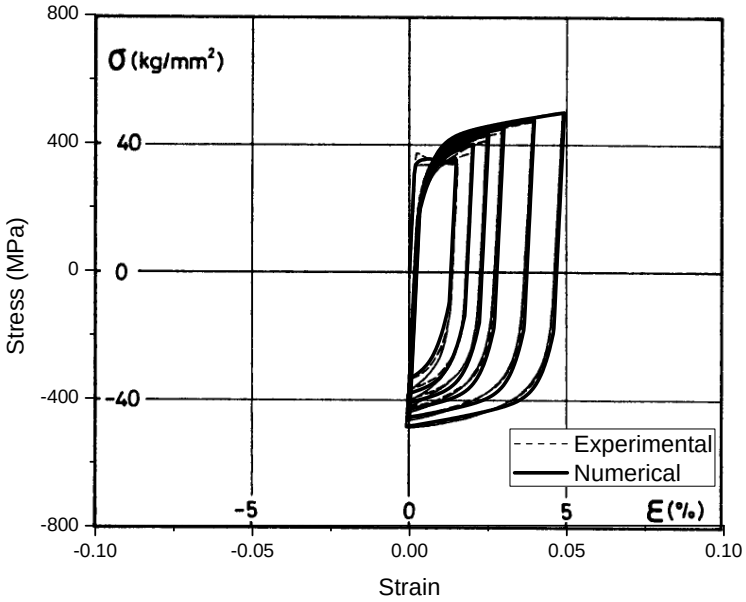

(a) Parameters Set A

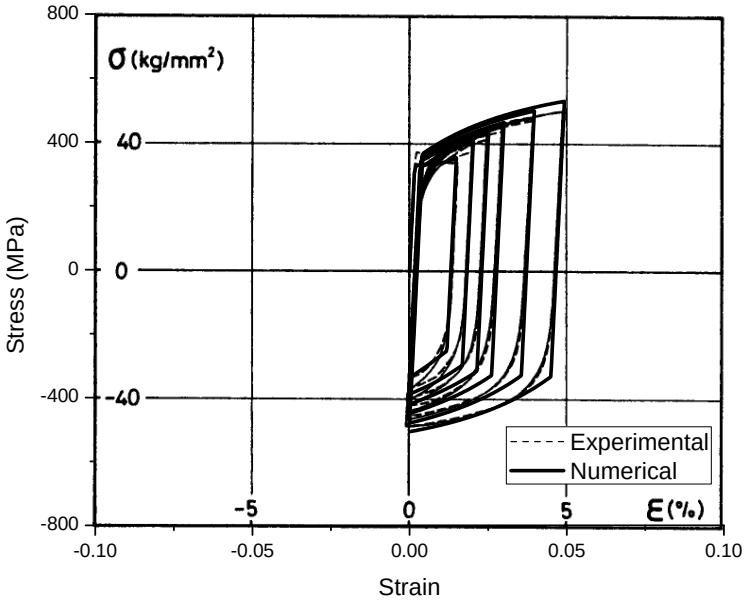

(b) Parameters Set B

[Experimental results by Fujimoto *et al.* (1985)]

Figure 5.4: Experimental versus numerical results (SM490 cyclic test 3)

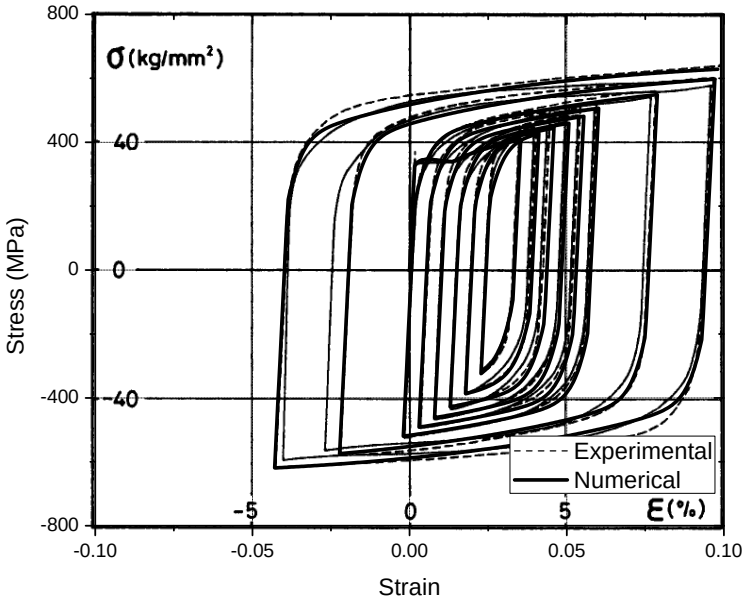

(a) Parameters Set A

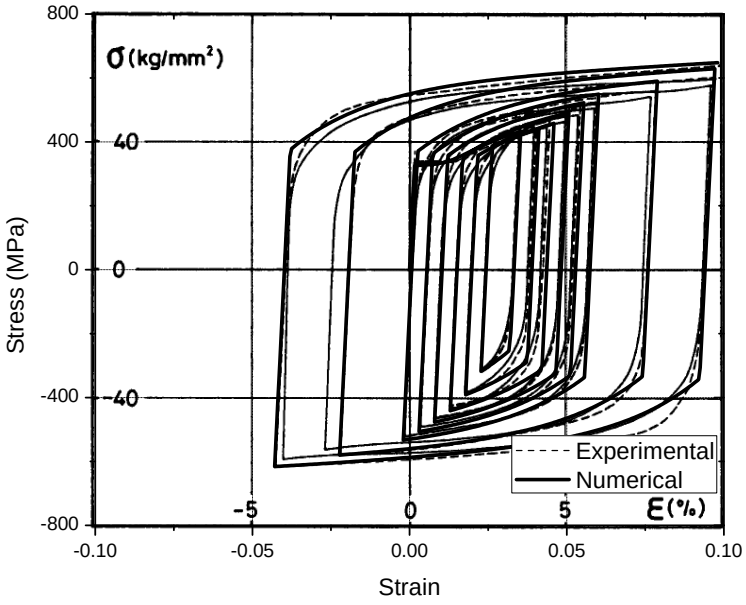

(b) Parameters Set B

[Experimental results by Fujimoto *et al.* (1985)]

Figure 5.5: Experimental versus numerical results (SM490 cyclic test 4)

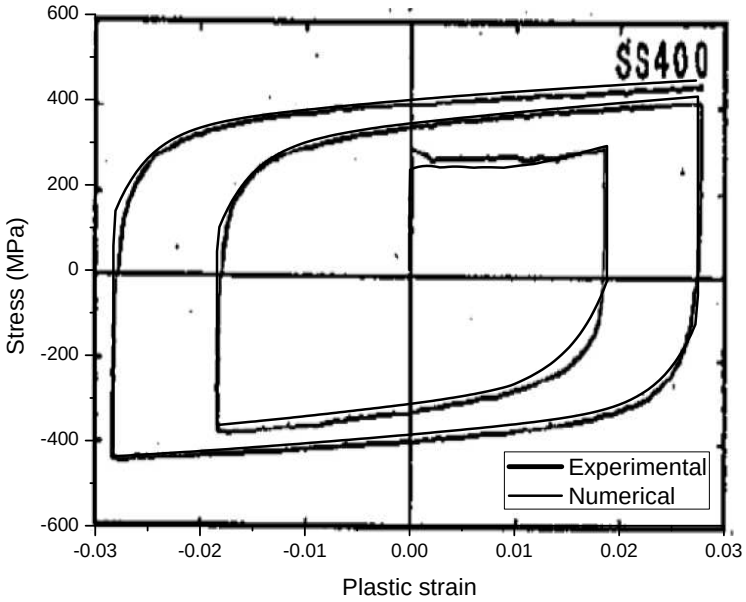

(a) Parameters Set A

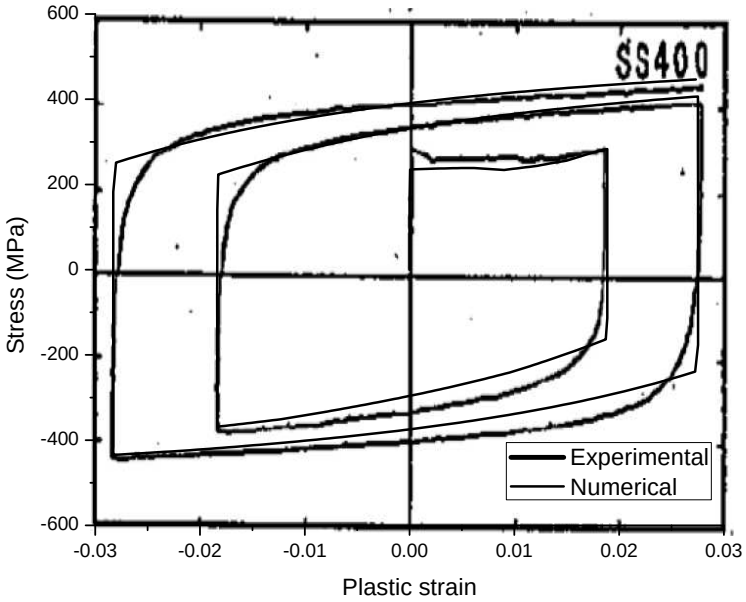

(b) Parameters Set B

[Experimental results by Nishimura *et al.* (1994)]

Figure 5.6: Experimental versus numerical results (SS440 cyclic test 1)

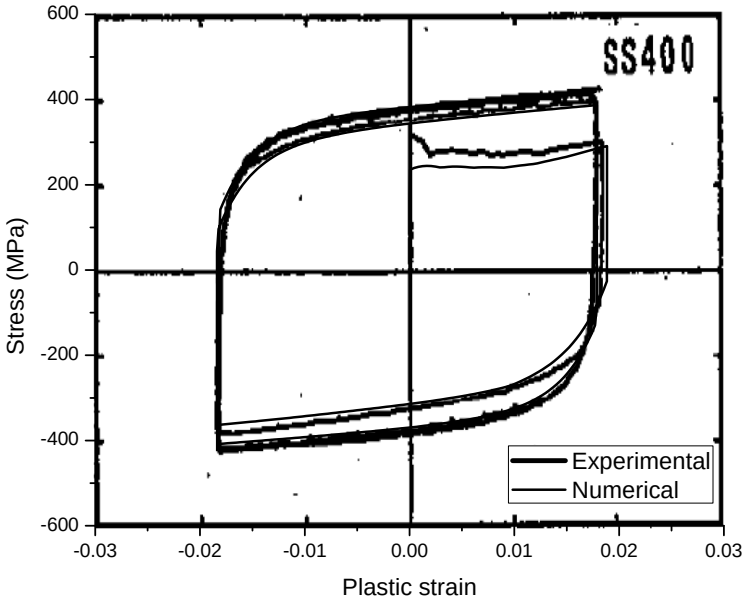

(a) Parameters Set A

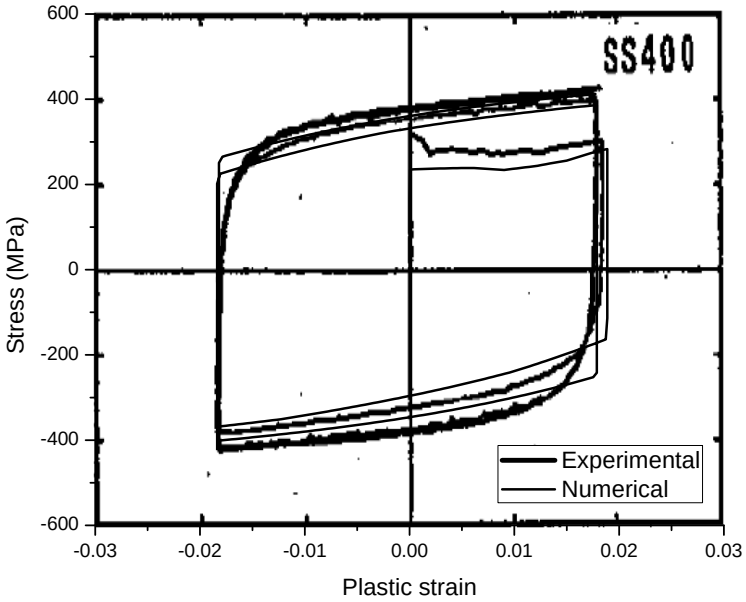

(b) Parameters Set B

[Experimental results by Nishimura *et al.* (1994)]

Figure 5.7: Experimental versus numerical results (SS440 cyclic test 2)

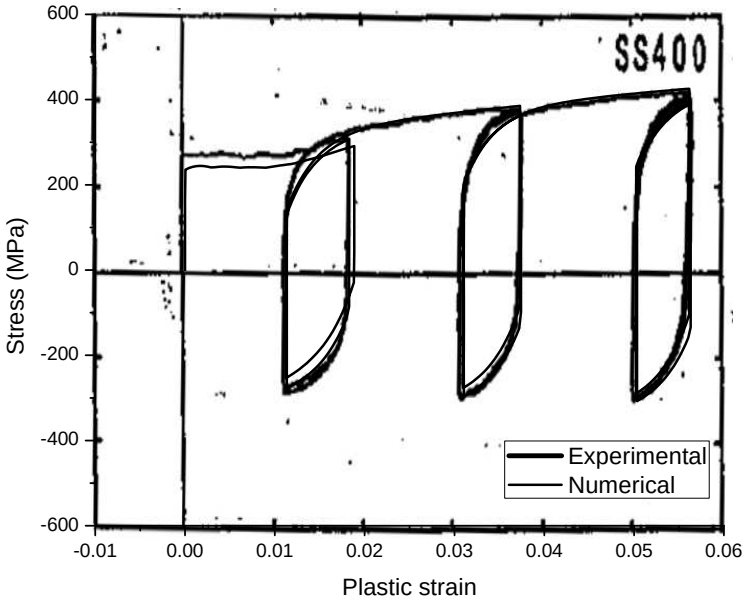

(a) Parameters Set A

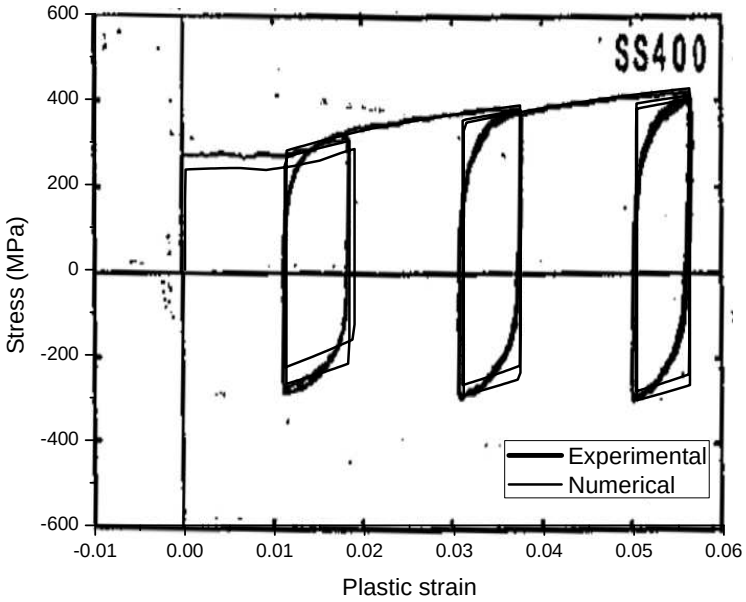

(b) Parameters Set B

[Experimental results by Nishimura *et al.* (1994)]

Figure 5.8: Experimental versus numerical results (SS440 cyclic test 3)

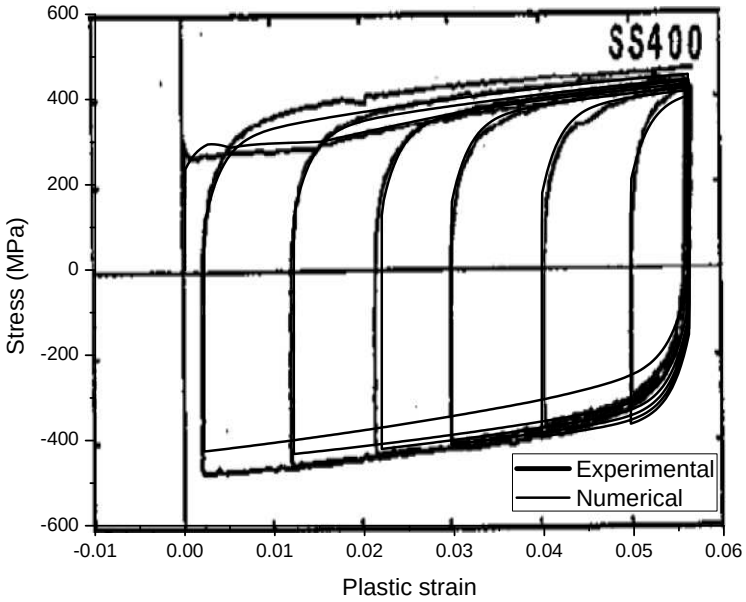

(a) Parameters Set A

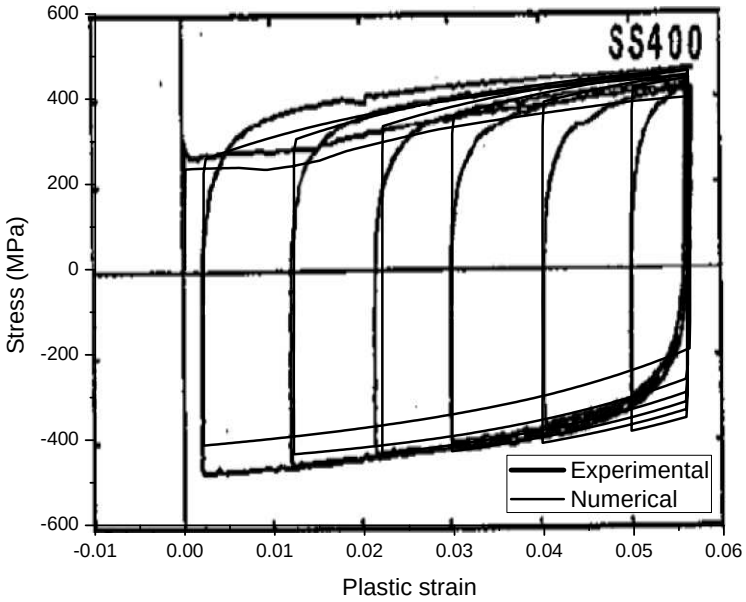

(b) Parameters Set B

[Experimental results by Nishimura *et al.* (1994)]

Figure 5.9: Experimental versus numerical results (SS440 cyclic test 4)

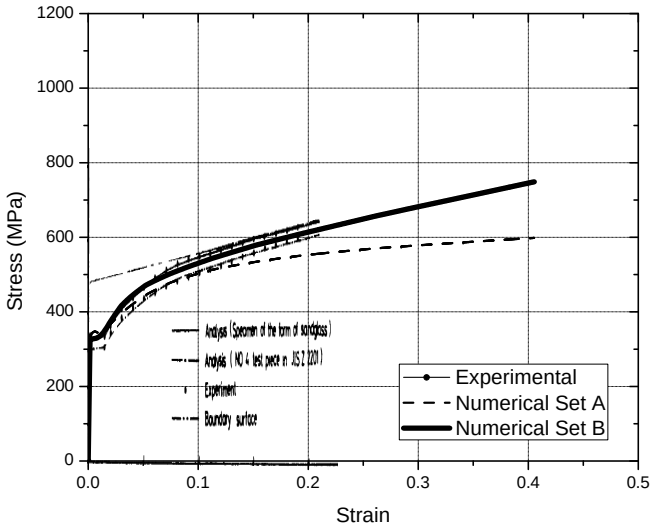

(a) SM490 steel

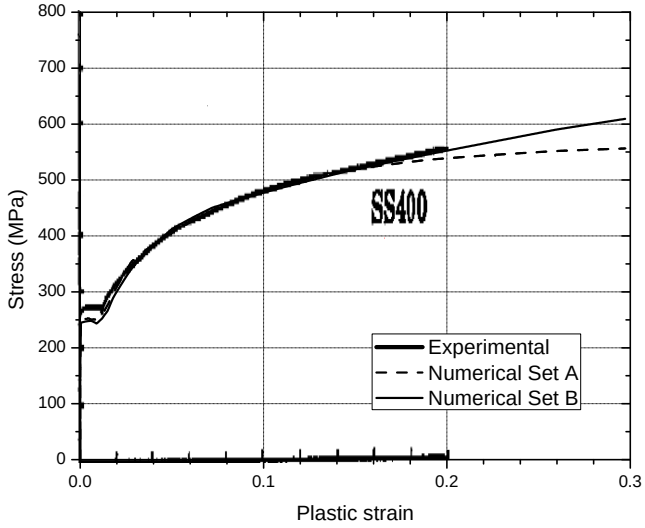

(b) SS440 steel

Figure 5.10: Experimental versus numerical results (monotonic loading)

5.2 Validation and application to components

Finite element analyses were done to assess the ability of the newly developed damage plasticity model to simulate the hysteretic behavior of braces, braced frame subassemblies, and beam-to-column connections. The focus of this investigation was to evaluate the prediction of local buckling and the evolution of damage because of low-cycle fatigue. Individual braces and beam-column connections subassemblies are described in this section and braced frame subassemblies are described in Section 5.3.

All finite element models were built using fully integrated shell elements (Engelmann *et al.,* 1989; Simo and Hughes, 1986; Pian and Sumihara, 1985) and implicit time integration. This type of shell element is based on a combined co-rotational and velocity-strain formulation. An embedded element coordinate system that deforms with the element is defined in terms of the nodal coordinates (LSTC, 2007). The Mindlin theory of plates and shells (Mindlin, 1951) is used to determine the velocity of any point in the shell.

Shell elements instead of solid elements were selected for these studies because the optimum element determined here for single braces are adopted for subsequent analyses of braced frame subassemblies and beam-column connections. Because the computational effort for complete braced frame is substantially greater than for an individual brace, efficient finite element models are preferred. A shell element is more time-consuming than a solid element in that shell elements require zero-normal stress iterations. But many more solid elements are required through the wall thickness to

capture the combined membrane and plate actions. Because shell and solid elements have the same number of degrees-of-freedom per element, more total CPU time is expected for models developed with solid elements than those with shell elements.

The choice of shell elements instead of beam elements is based on the consideration that beam elements assume that plane sections remain plane and the sectional coordinates of integration points on plane sections remain constant during the course of analysis. This assumption makes it impossible to model local buckling of a tube-section brace using beam elements. For shell elements, a tube section is built with several elements. Therefore, there are sufficient degrees-of-freedom related to local buckling deformation.

Crack initiation and propagation is modeled by element erosion (element removal). Once the material point damage parameter exceeds a critical damage state corresponding to fracture, it is considered failed and is removed from a model. Although the shell element size is much larger than the material characteristic length of deterioration ($\sim$ 0.01 inch, Kanvinde and Deierlein, 2004), the gradients of equivalent plastic strain and damage variable contours are small with respect to the characteristic length before crack initiation. Therefore, it is acceptable to have shell element sizes larger than the characteristic length, but a mesh convergence test is required. Mesh convergence for a single brace is examined in Section 5.2.1 using progressively refined finite element meshes.

5.2.1 Single brace

A finite element model was built for the single brace test specimens discussed previously in Section 2.1 (Yang and Mahin, 2005). Because the yield stress and ultimate stress were the only material properties known for the braces, the damage evolution constants for the steel material needed to be calibrated using the overall results for individual braces. The applied displacement history for each experiment was extracted and prescribed as a time-varying displacement boundary condition at one end of the brace and the other end was fixed. No initial imperfection was introduced in the finite element model. The buckling was expected to be trigged by perturbations of numerical truncation or round-off error.

The analysis results are shown in Figures 5.11 to 5.14. Global buckling (Figure 5.11), local buckling and damage localization (Figure 5.12), crack initiation (Figure 5.13), and crack propagation (Figure 5.14) were successfully simulated, demonstrating that the cyclic damage plastic model is suitable even though only basic plasticity and damage models were used. Comparisons between experimental and numerical results for the axial force-axial displacement hysteretic curves are shown in Figures 5.15 to 5.17, and the comparisons for peak loads in each half cycle are shown in Figures 5.18 to 5.20. By incorporating the damage model, the numerical analyses predict with a fair degree of accuracy the strength deterioration and the resulting force-displacement curve over the whole loading history. This makes it reasonable to extend the modeling of an individual brace to a larger model of a complete braced frame subassembly.

The mesh sensitivity of plastic strain was validated using models with successively smaller elements. Plastic strain was chosen as the index of quality because it is the major source of damage. Four different element sizes in the refined mesh region at brace mid-span (Figure 5.12) were evaluated. Figure 5.21 shows the time history of plastic strain for these four element sizes. Note both the equivalent plastic strain and the damage state are seen to converge reliably when the element size is at the order of shell thickness. Obviously after crack initiation, the gradients of both equivalent plastic strain and damage state are much higher. Mesh sizes larger than the material characteristic length combined with element erosion for crack will result in a larger energy release rate at the crack tip (Xia and Shih, 1995) and blunt the crack front to an unrealistic size, resulting in an exaggerated ductile behavior of crack tip. But this is a local behavior of crack tip, and before the crack tip behaves inelastically, the strength and stiffness of a typical brace member have significantly deteriorated because of lateral and local buckling; therefore, the exaggerated crack front blunting when using large-size shell elements should have less influence on the force-deformation performance. Note that mesh sizes at the same scale of the material characteristic length may be required for analyses of local crack tip behavior. It is believed the choice of shell element at sizes around the shell thickness achieves an overall model that is as simple as reasonably possible with reasonable accuracy for analyses of braces and braced frame subassemblies. This choice of shell element size is applied to all analyses in this research.

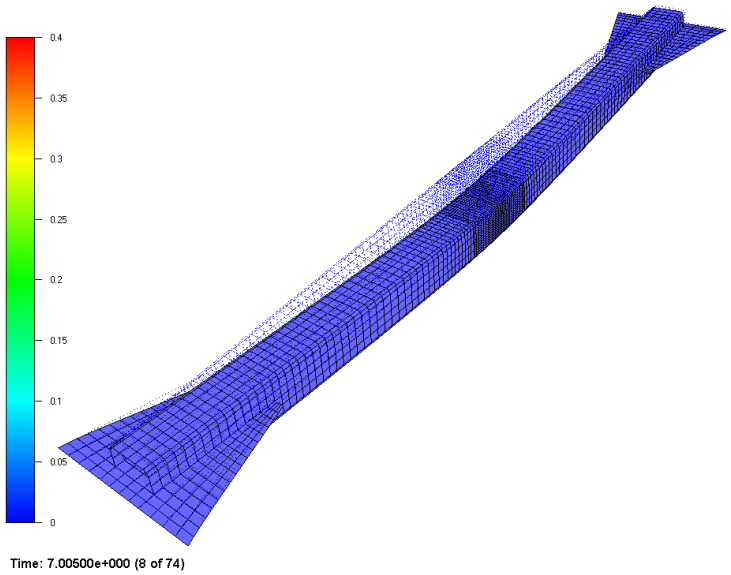

(dashed line for undeformed shape)

Figure 5.11: Global buckling of brace specimen 5 (after Yang and Mahin, 2005)

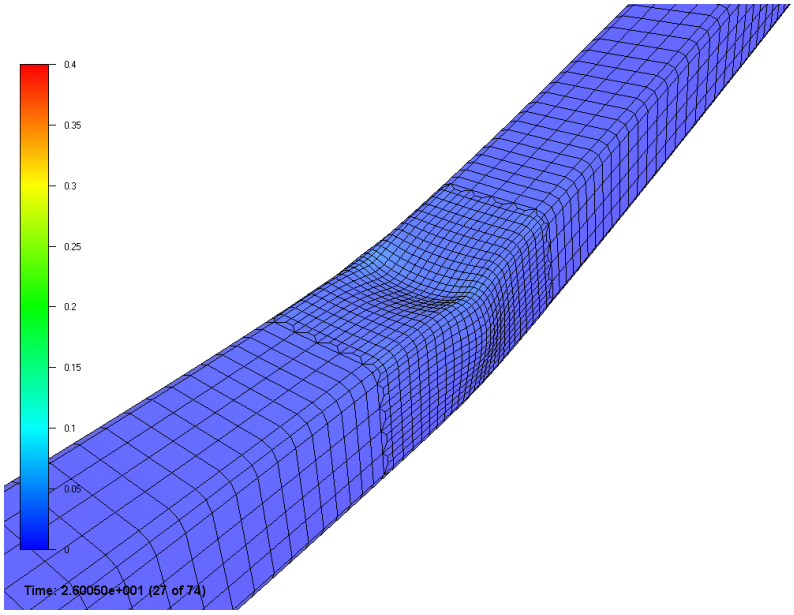

Figure 5.12: Local buckling of brace specimen 5 (after Yang and Mahin, 2005)

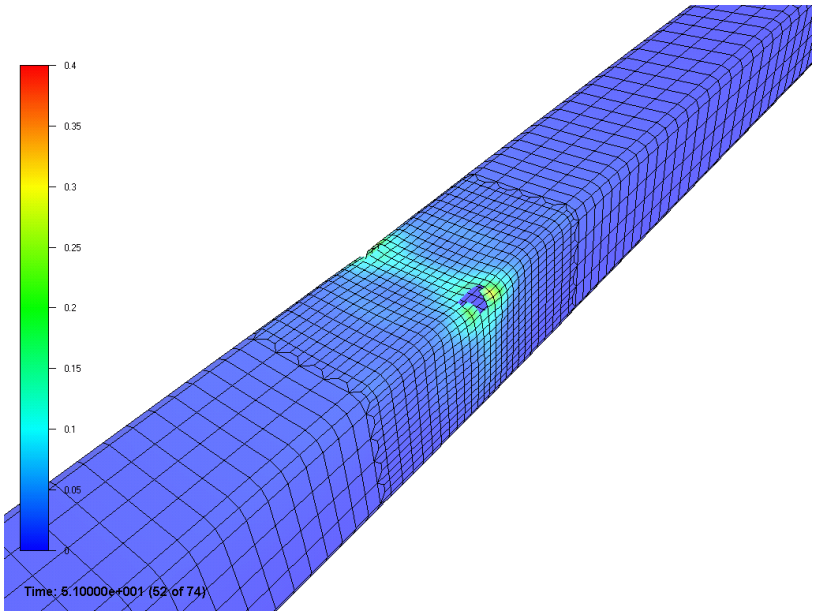

Figure 5.13: Crack initiation of brace specimen 5 (after Yang and Mahin, 2005)

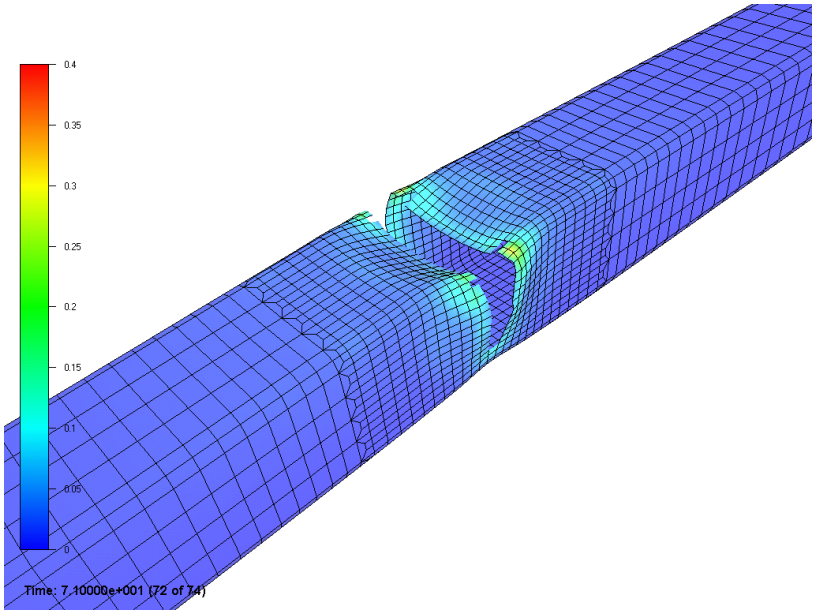

Figure 5.14: Crack propagation of brace specimen 5 (after Yang and Mahin, 2005)

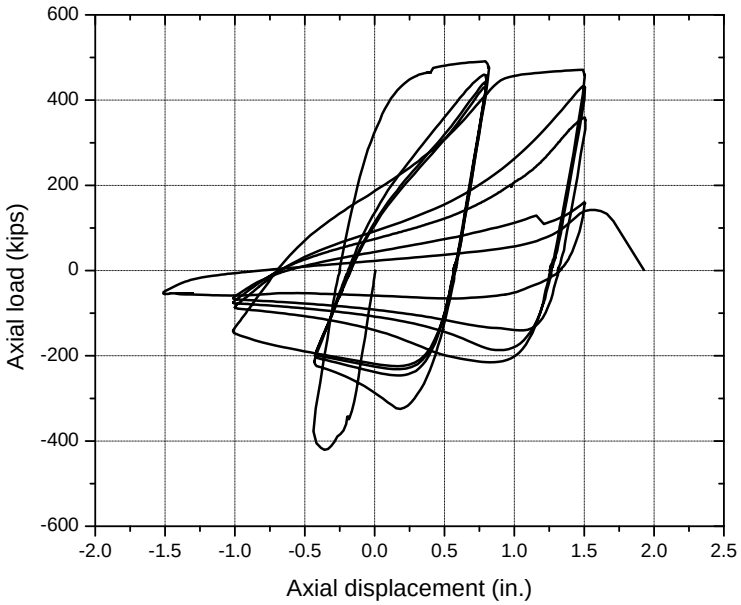

(a) Experimental result

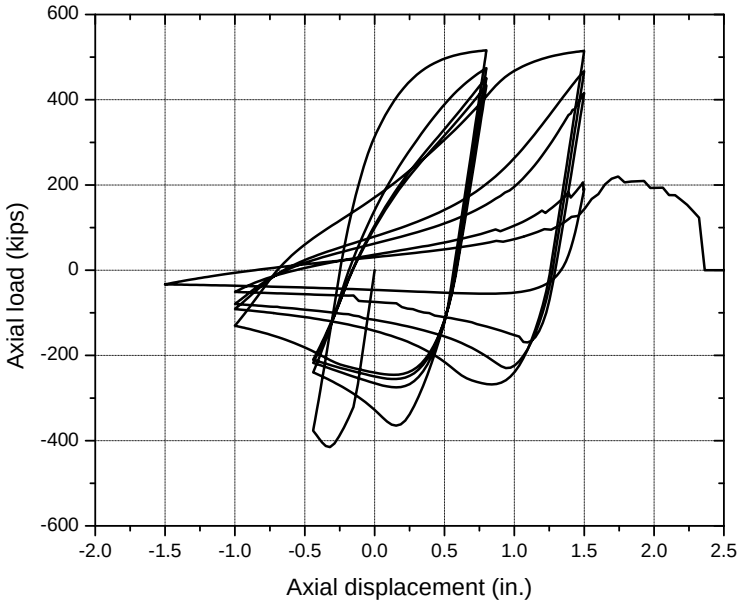

(b) Numerical result

Figure 5.15: Hysteresis loops of brace specimen 5 (after Yang and Mahin, 2005)

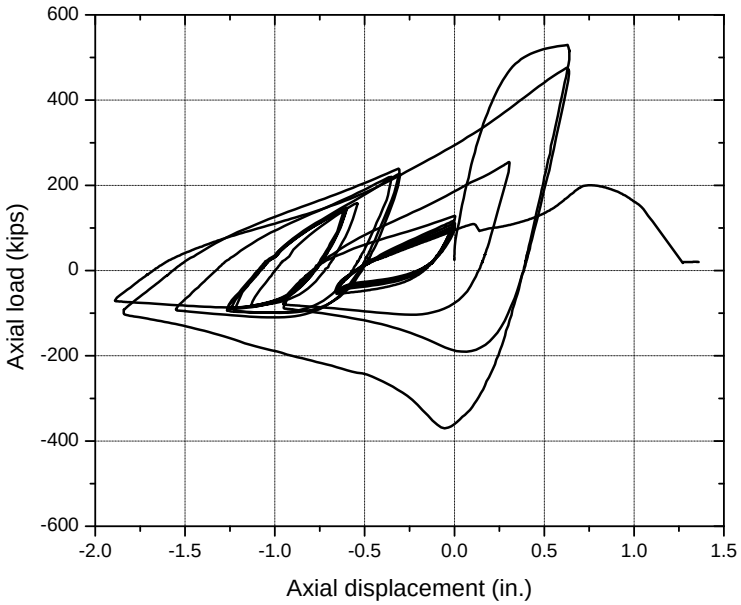

(a) Experimental result

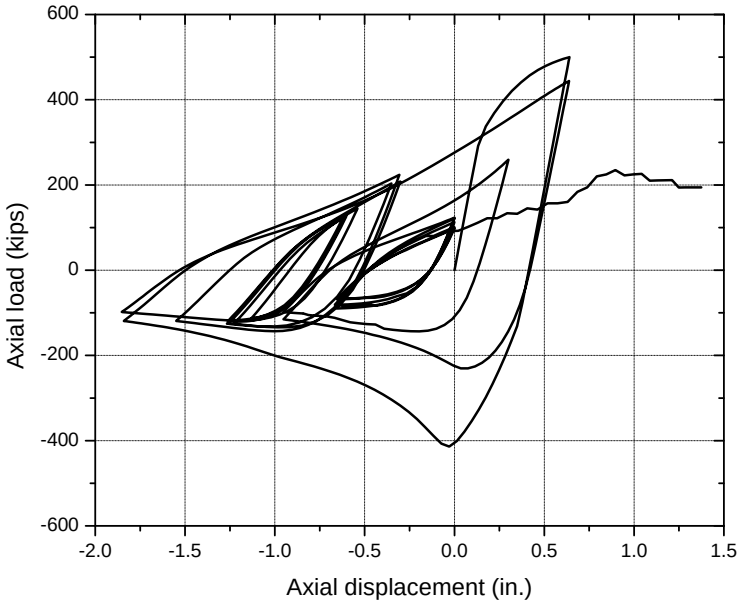

(b) Numerical result

Figure 5.16: Hysteresis loops of brace specimen 7 (after Yang and Mahin, 2005)

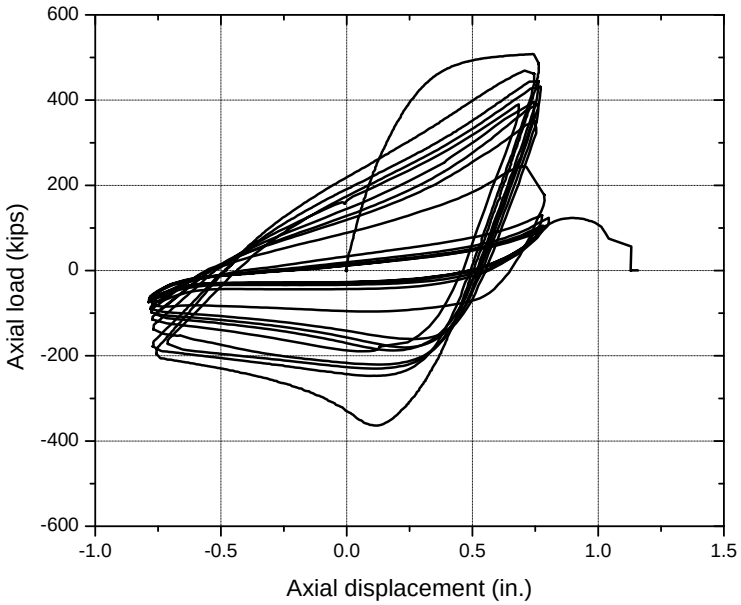

(a) Experimental result

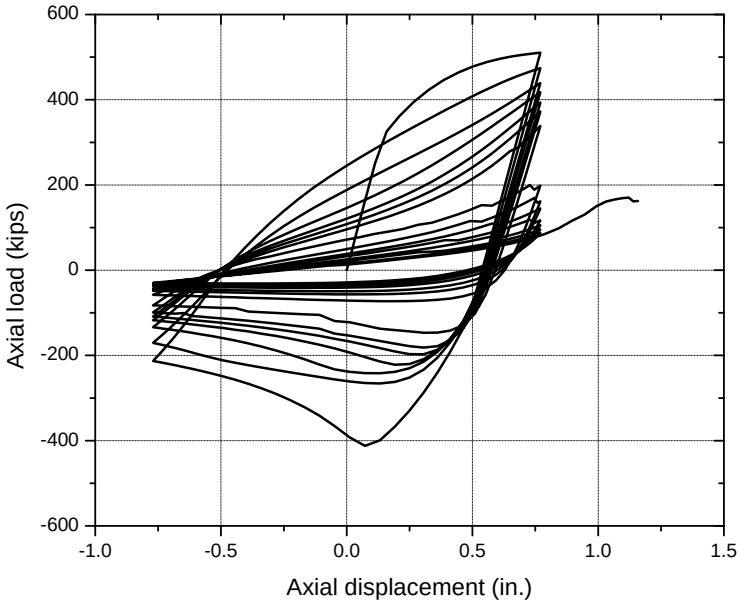

(b) Numerical result

Figure 5.17: Hysteresis loops of brace specimen 8 (after Yang and Mahin, 2005)

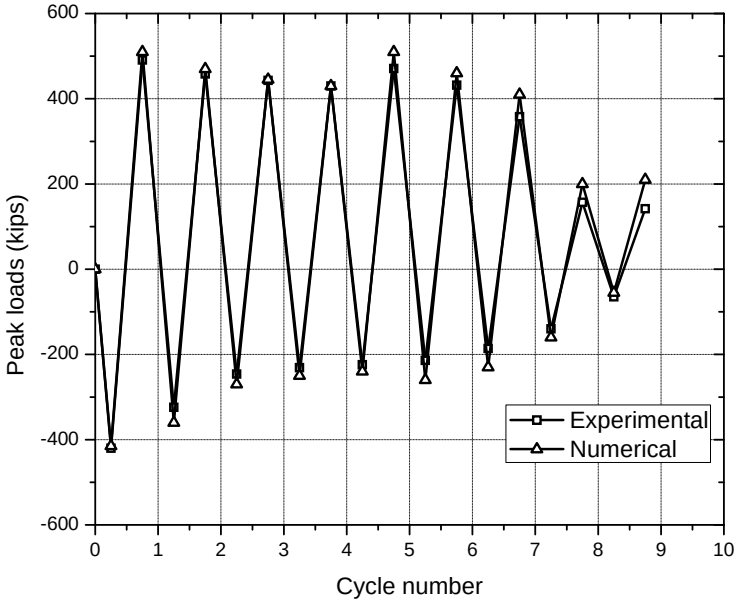

Figure 5.18: Peak loads of brace specimen 5 (after Yang and Mahin, 2005)

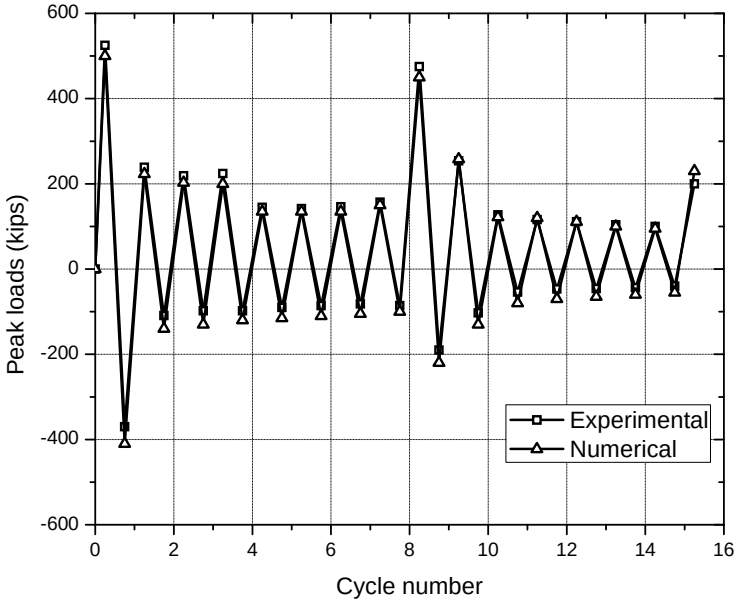

Figure 5.19: Peak loads of brace specimen 7 (after Yang and Mahin, 2005)

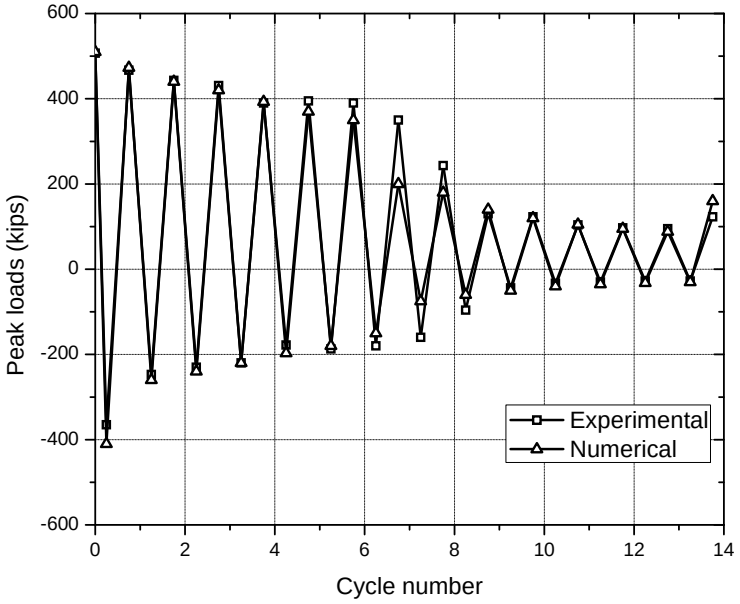

Figure 5.20: Peak loads of brace specimen 8 (after Yang and Mahin, 2005)

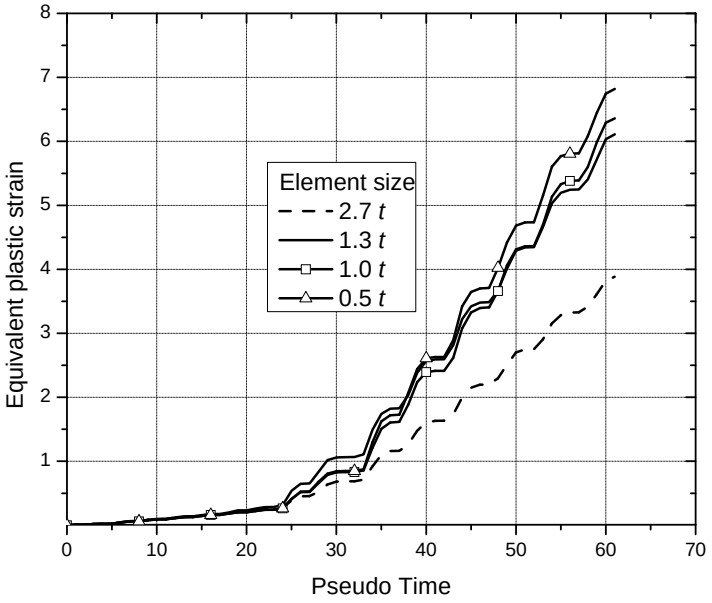

Figure 5.21: Evolution and mesh sensitivity of plastic strain (shell thickness t)

5.2.2 Single beam-column connection

A finite element model was built for the welded steel beam-column connection subassembly tested by Tanaka *et al.* (2000) and discussed previously in Section 2.4. Half of specimen is modeled and symmetry boundary conditions were applied. The finite element model is shown in Figure 5.22. The newly developed cyclic damage plasticity model was used. The parameters of combined isotropic and nonlinear kinematic hardening were calibrated against experimental data from Nishimura *et al.* (1994).

Figure 5.23 shows the numerical result of the load-displacement curve compared with the experiment. Most of the hysteretic features are well captured by the simulation. Some comparison of the buckling shape between simulations and experiments are shown in Figures 5.24 to 5.26. The simulation results match the experiment very well.

The last half cycle of experiment displacement history starts from -60 mm to 80mm. In the numerical analysis, the displacement history was extended with 10 cycles of displacement amplitude at 80 mm. Further local buckling was observed and the hysteretic loop stabilized, but no low-cycle fatigue-induced fracture was observed. In order to apply and validate the material model, beam-column connection test by Suita *et al.* (2000) was also simulated and discussed below.

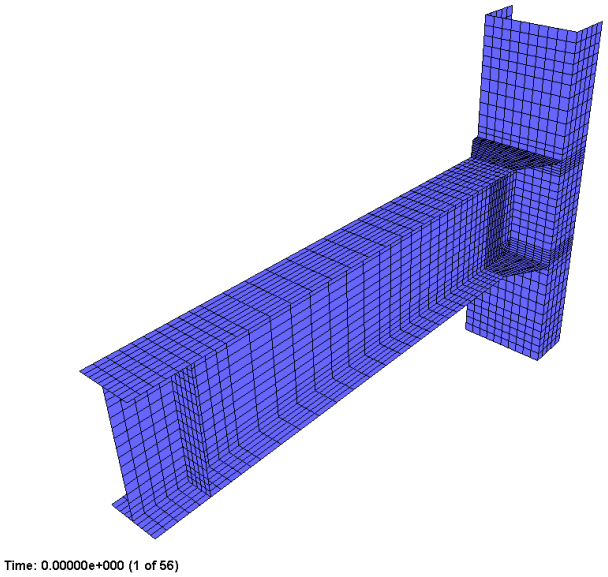

Figure 5.22: Finite element modeling of BW10 specimen

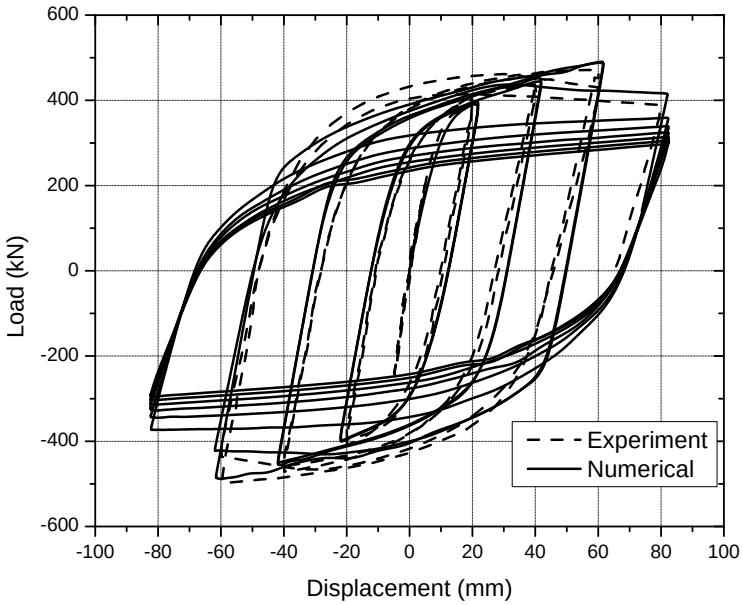

Figure 5.23: Hysteretic loop of BW10 specimen

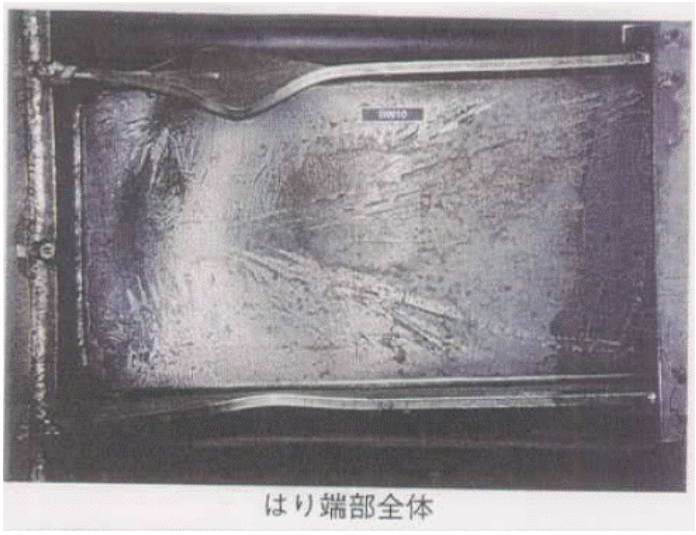

(a) Experimental result

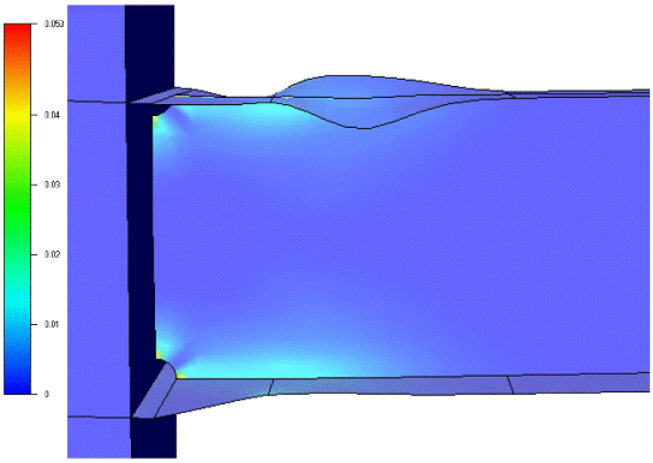

(b) Numerical result

Figure 5.24: BW10 behavior comparison 1

(a) Experimental result

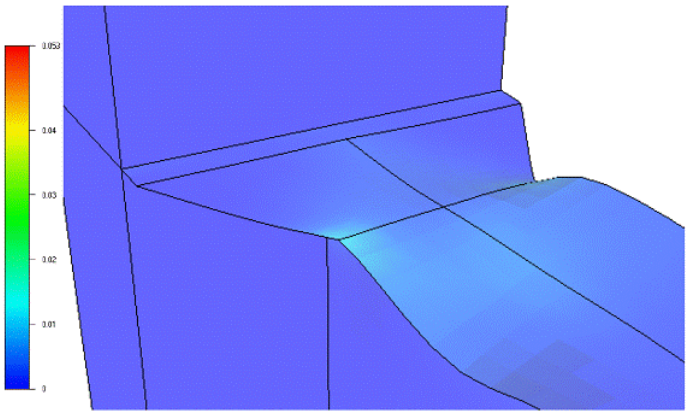

(b) Numerical result

Figure 5.25: BW10 behavior comparison 2

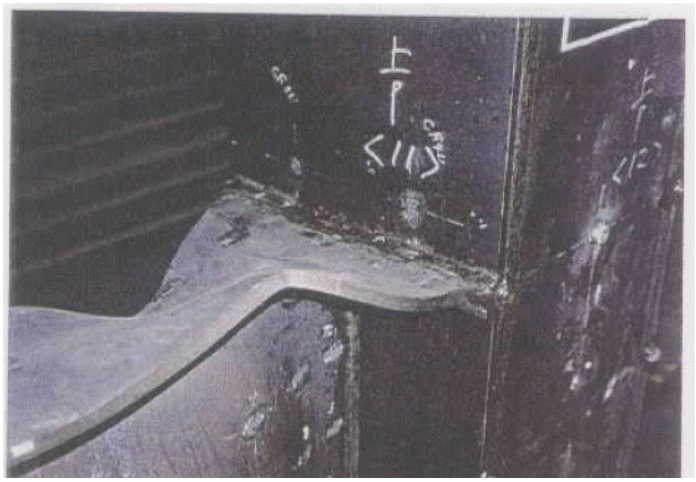

(a) Experimental result

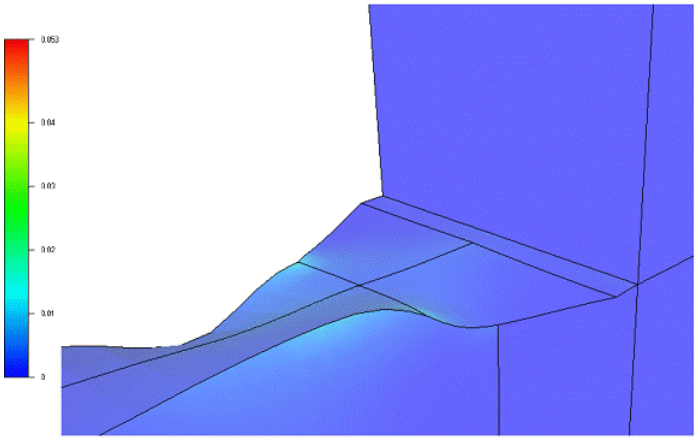

(b) Numerical result

Figure 5.26: BW10 behavior comparison 3

The beam-column connections experiment by Suita *et al.* (2000) discussed in Section 2.4 was also analyzed. The specimens ruptured because of low-cycle fatigue in a region of the beam flanges where large plastic deformation and local buckling occurred. Specimen N4 was numerically simulated and results are plotted in Figures 5.27 to 5.30.

The finite element model used is shown in Figure 5.27. Because there was no weld access hole, the structural mesh was easily established. To reduce computational costs, only the region near the face of the beam-column connection is refined. Because a single beam framed into the column, and assumptions of symmetry could not be used as in the case of the column tested by Tanaka *et al.* (2000), the whole column (instead of half) was modeled.

The newly developed cyclic damage plasticity model was used for the simulations. The initial estimate used for the material modeling parameters were almost identical to those used in BW10, except the initial yield stress was changed to match those obtained from coupon tests for Specimen N4. Damage was calculated, and the elements eroded during the analysis as damage accumulated.

Because stress-strain relations for the steel in this specimen were not available, the default damage parameter set for the material was used as an initial estimate as no detailed cyclic material stress-strain data was available for this specimen to calibrate the model. The "default" damage parameter S is around $Fy/200$ to $F_u/200$, where F_y and F_u are the yield stress and ultimate stress of the steel, respectively. For this

test specimen (N4, Set B), the reported F_y for the flange was 295 MPa and that for the web was 325 MPa.

Figure 5.28 presents and compares the numerical load-displacement curves with the experimental data. Both buckling and damage features are well captured by the analysis. The buckled shape is shown in Figure 5.29, and the final fracture pattern in the flange is shown in Figure 5.30. These results match the final damage description in Suita *et al.* (2000) very well.

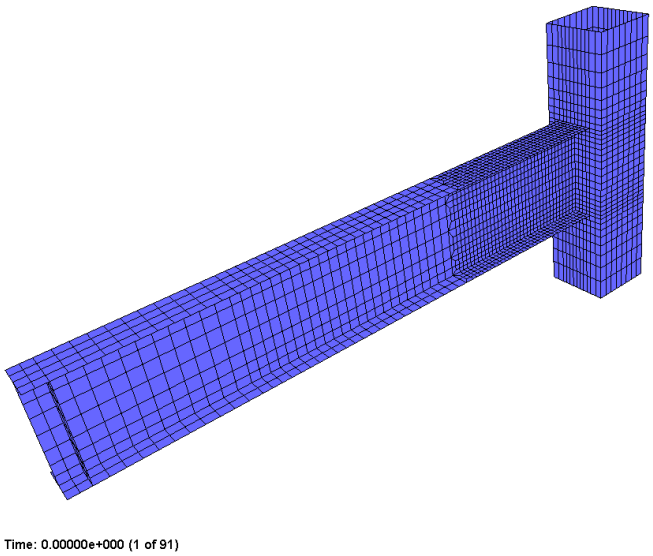

Figure 5.27: Finite element modeling of N4 specimen

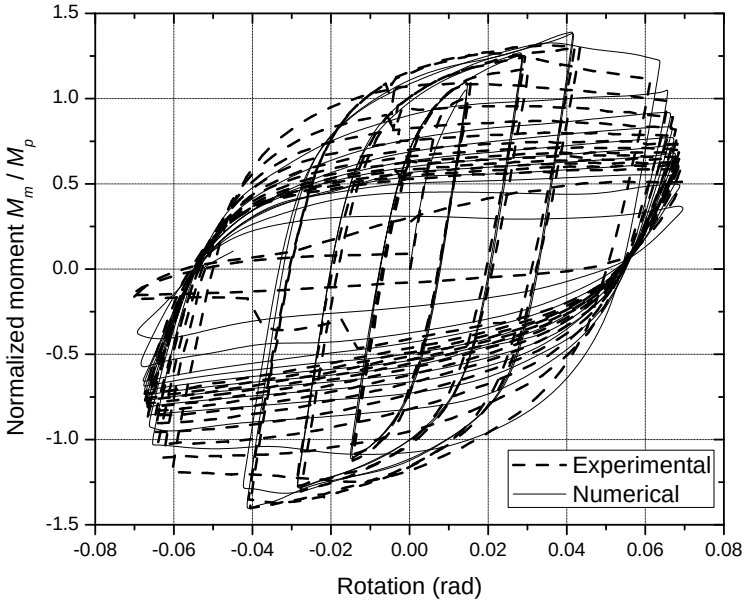

Figure 5.28: Hysteretic loop of N4 specimen

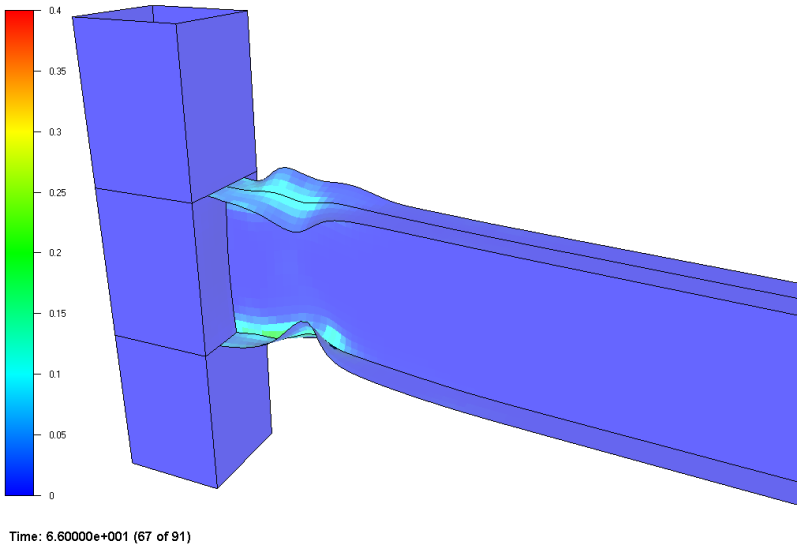

Figure 5.29: Predicted local buckling and damage

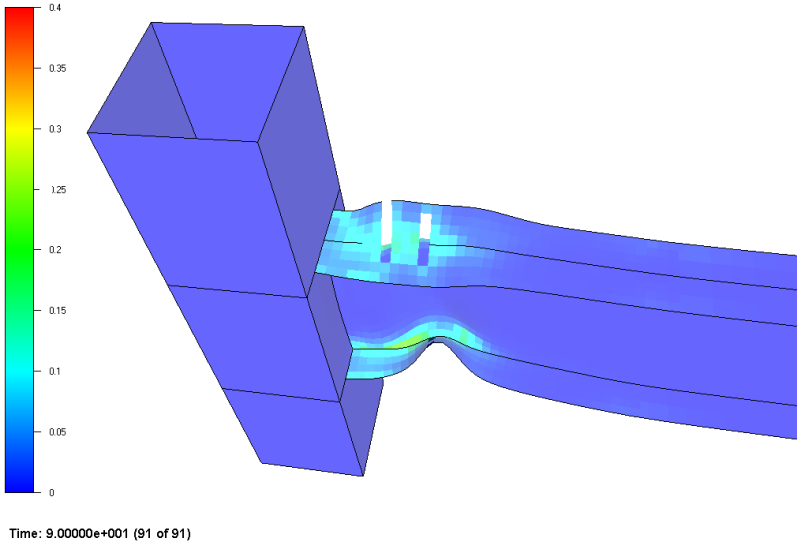

Figure 5.30: Predicted fracture in top flange

5.3 Validation and application to subassemblies

5.3.1 Subassembly subjected to quasi-static loading

A finite element model was developed for the braced frame subassembly discussed previously in Section 2.3, as an extension of the approach used to model for the individual brace discussed in Section 5.2.1. Details including the gusset plate and the shear tab in beam column connection are modeled. For the sake of simplicity, no out-of-plane offset of the shear tab is modeled. The roof level displacement was prescribed. The base was fixed and out-of-plane constraints were imposed on the column ends and beam mid-spans as they were in the experiment.

The analysis results are shown in Figures 5.31 and 5.32. The distribution of damage within the subassembly is accurately simulated (Figure 5.31). The sequence and nature of global, local buckling and fracture of braces are very similar to test results. In additional, the damage and fracture at the beam-column connection, right near the corner of the shear tab, was predicted as well (Figure 5.32). Considering the material parameters used were approximate, these results show that the cyclic damage plasticity model predicts overall response to a reasonable degree and should be useful for damage evaluation of the steel structures, especially if material properties are well defined. Figures 5.33 and 5.34 show the base shear-roof displacement hysteresis curves for the experimental and numerical analysis, respectively. Note that strength, stiffness, and deterioration in overall behavior of the braced frame is well simulated.

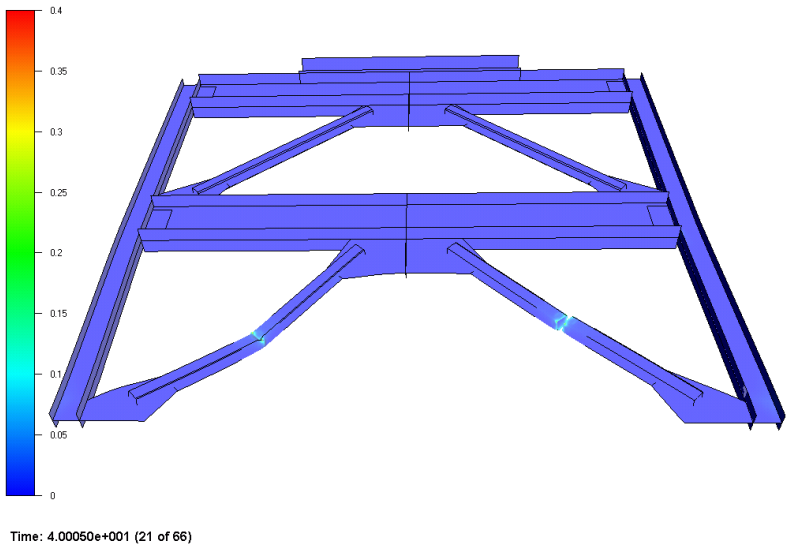

Figure 5.31: Damage and fracture of brace

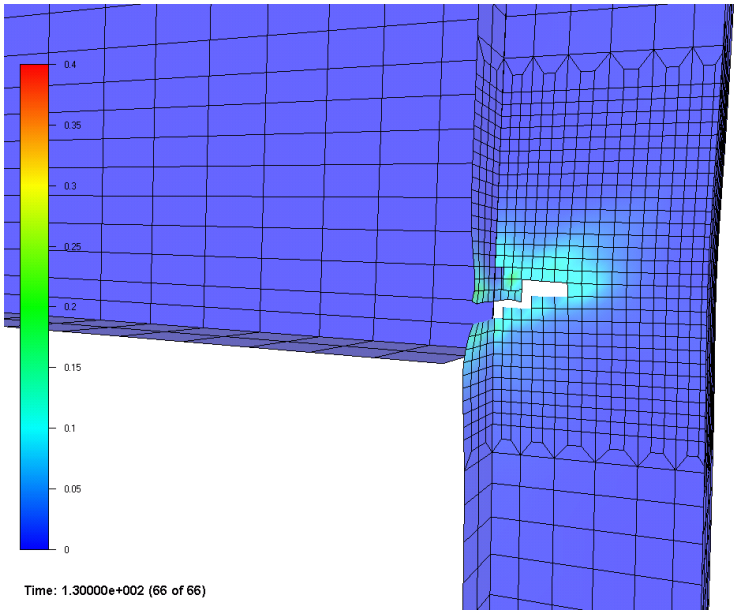

Figure 5.32: Damage and fracture of beam-column connection

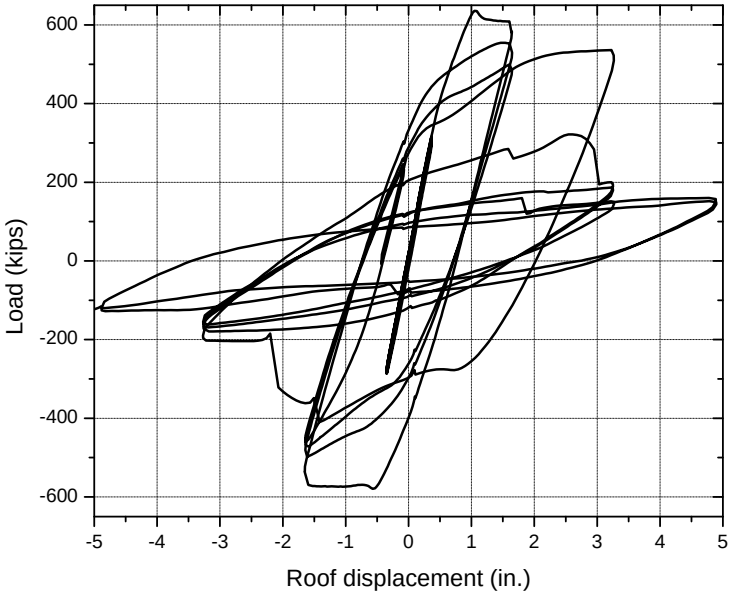

Figure 5.33: Experimental result for braced frame

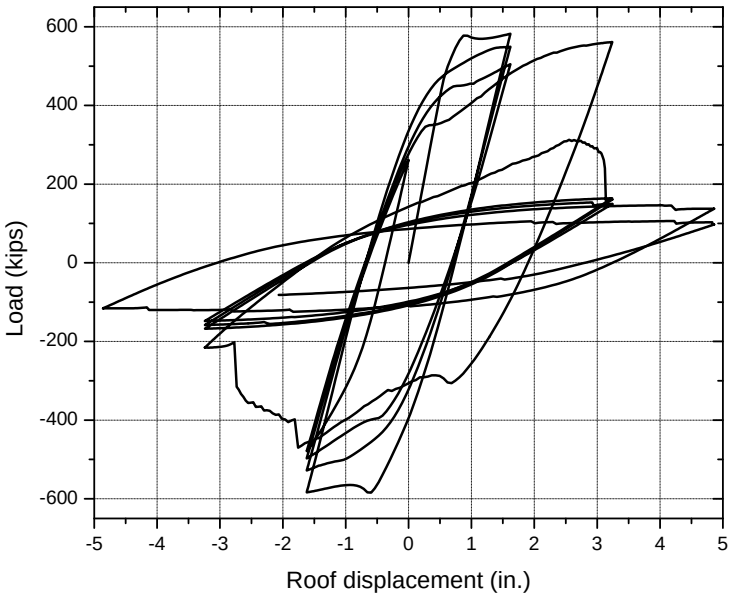

Figure 5.34: Numerical result for braced frame

5.3.2 Subassembly subjected to dynamic loading

The previous subsection simulated the subassembly subjected to quasi-static loading. To predict response under dynamic loading, masses were assigned to the floor levels, and the LA23 ground motion was imposed. LA23 is one of the 20 ground motions assembled for the SAC project (Somerville *et al.,* 1997) representing an exceedance probability of 2% in 50 years, derived from the free-field motion recorded at a distance of 3.5 km during the 1989 Loma Prieta earthquake. The design base shear capacity of the structure, based on the methods used in ASCE 7-05, was used to determine the weight of structure that the code would assume could be supported by the braced frame. The total weight was equally distributed between both floors. The model and ground motion is shown in Figure 5.35.

The failure mode at time $t = 13.8$ second is shown in Figures 5.36 to 5.38 from different points of view. The braces in the first story buckled and restraightened repeatedly, causing the bottom story to become a soft story.

From the hysteretic loops shown in Figure 5.39 and first-story drift time history shown in Figure 5.40, one can see that extremely large interstory drifts occur for the selected earthquake motion. Comparison of models with and without damage incorporated are also shown in Figures 5.39 and 5.40. For the model without damage, the structure does not collapse; for the one with damage, substantial deterioration of strength, stiffness occurs and the structure collapses. The significant difference suggests the importance of considering damage in the simulation.

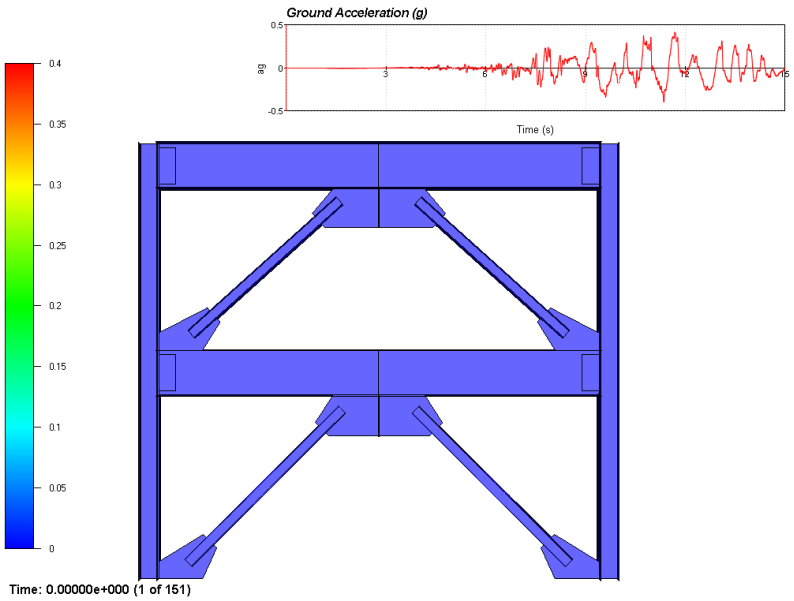

Figure 5.35: Subassembly model and ground motion

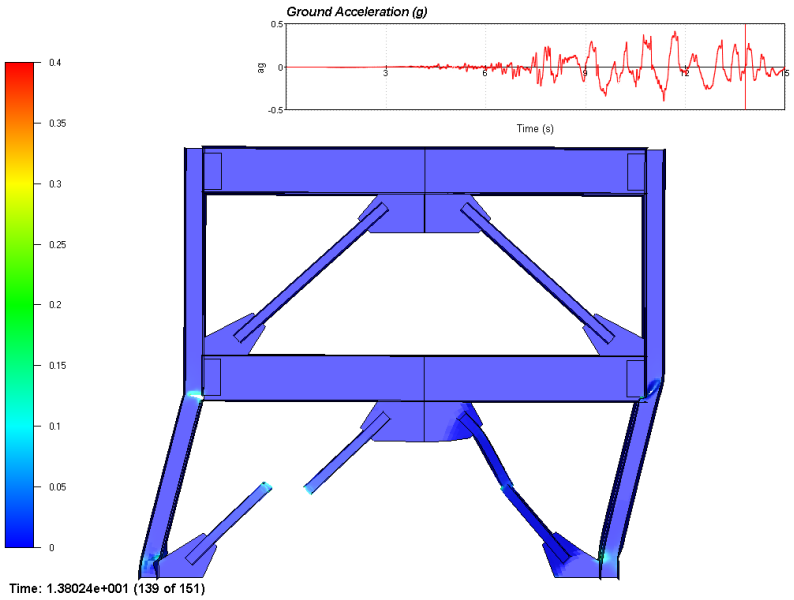

Figure 5.36: Failure mode at time $t = 13.8$ sec, global view

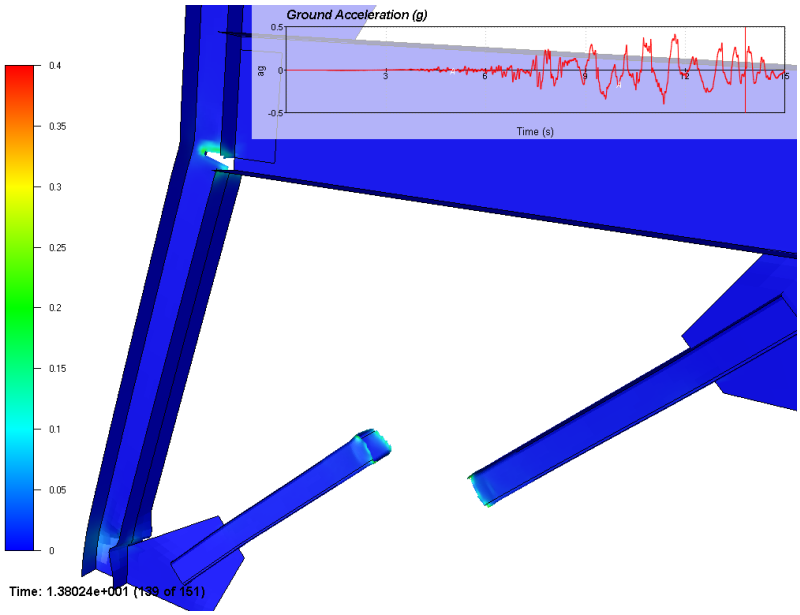

Figure 5.37: Failure mode at time $t = 13.8$ sec, local view 1

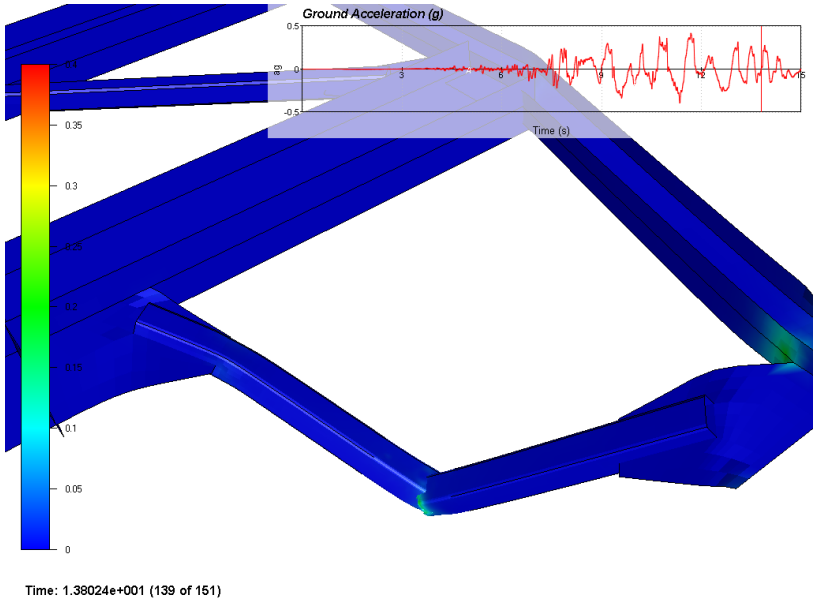

Figure 5.38: Failure mode at time $t = 13.8$ sec, local view 2

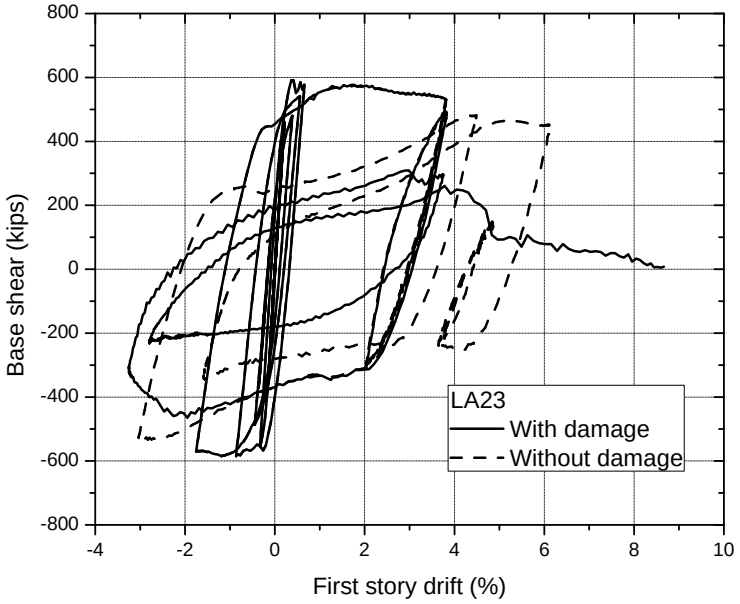

Figure 5.39: Base shear versus first-story drift

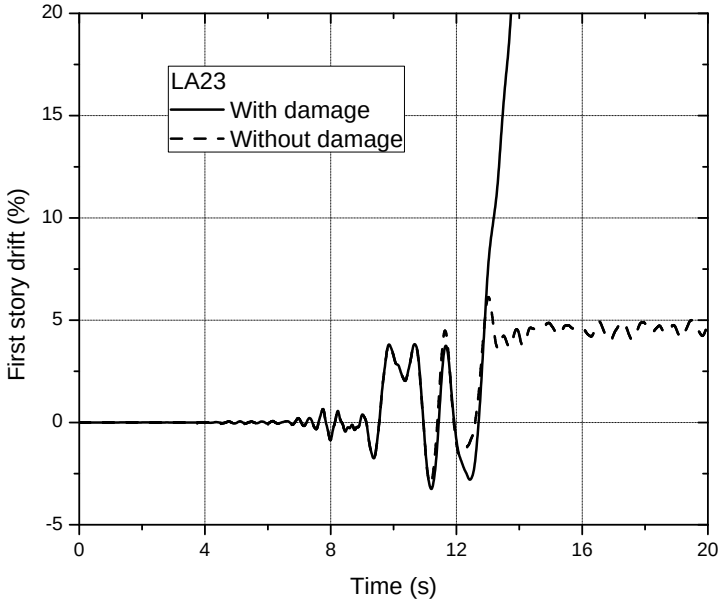

Figure 5.40: First-story drift time history

5.4 Concluding remarks

Computational results obtained with the new cyclic damage plasticity model correlate well with test results for individual braces, beam-to-column connections, and braced frame subassemblies. These applications of the model illustrate the importance of considering material nonlinearity, local and global buckling, and the exhaustion of the ability of the material to deform inelastically caused by low-cycle fatigue.

Chapter 6

Studies of Steel Braced Frame Behavior

For Special Concentrically Braced Frame (SCBF) systems, energy dissipation is achieved by tension yielding and compression buckling of the braces, and all other components are intended to remain essentially elastic. To achieve desirable ductile behavior in the braces, the AISC Seismic Provisions for Structural Steel Buildings (AISC, 2005b) have several requirements for proportions and details of SCBF systems. Requirements that are closely related to studies of steel braced frame behavior in this chapter include:

- **Slenderness of brace.** — Bracing member slenderness is quantified as the slenderness ratio KL/r, where K is the effective length factor, L is laterally unbraced length of the member, and r is governing radius of gyration. Brace

slenderness is limited to ensure adequate compressive strength and resistance to the cyclic degradation of the brace.

- **Compactness of section.** — Sections are classified as compact, noncompact, or slender-element sections. Compact sections are those capable of developing a fully plastic stress distribution and possessing a rotation capacity of approximately three before the onset of local buckling (AISC, 2005b). Compactness of section is quantified in terms of width-thickness ratios $\lambda = b/t$. For flanges of rectangular hollow structural sections, width b is the clear distance between webs less the inside corner radius on each side, and the thickness t is the design wall thickness. The post-buckling performance of the braces is also dependent on the compactness of the members. Higher width-to-thickness ratios may lead to earlier and more severe local buckling, which in turn results in premature rupture of the brace and lower energy dissipation capacity.

- **Connections.** — Connections are responsible to combine and transmit forces between the bracing element and framing beams and columns. Requirements for these connection details help realize ductility and energy dissipation of the system by preventing premature failure modes.

- **Beams.** — For V-type and inverted V-type frames, beams must be continuous between columns and must be designed for vertical unbalanced loads associated with yielding of the tensile brace and buckling of the compressive brace. Beam

top and bottom flanges must be braced at the intersection of the braces and beam.

This chapter first looks at the effect of brace proportions (slenderness ratio KL/r and width-thickness ratios b/t) on fatigue life capacity of bracing members subjected to cyclic deformation histories. Here, fatigue life demand is how much the brace needs to deform inelastically to achieve expected system performance. In contrast, fatigue life capacity is how much the brace is able to deform inelastically before failure of low-cycle fatigue. Fatigue life demand can for example be specified as the demanded deformation history of a brace corresponding to two interstory drift cycles of 2%, followed by three interstory drift cycles of 1%.

A parametric study of fatigue life demand for SCBF systems with different structural period, brace slenderness and compactness, ground motion characteristics, and so on is not considered in this research. In the current research, only fatigue life capacity is investigated. Factors affecting fatigue life capacity are discussed in Section 6.1. After fatigue life demand and capacity are both well understood, one can compare them for a given structure and to avoid fracture, adjust the design parameters of the structure such that the fatigue life demand is satisfied by the fatigue life capacity. Code requirement of braces proportions (slenderness of member and compactness of section) may be similarly determined by statistical comparison of fatigue life demand and capacity of different structures.

Next, the effect of connection details on damage accumulation in the column is studied. Although the tensile, flexural, and compressive strength requirement for connection in the AISC Seismic Provisions helps forces transfer and ensure system integrity, high local stress and large plastic deformation in the column leading to fracture may effect the performance. Some connection details may result in crack initiation and propagation in the column, as observed in Uriz (2005) (Figure 2.7), and simulated in Section 5.3 (Figure 5.32). Because damage control of columns is essential to maintain integrety of the gravity load resisting system, it is necessary to evaluate and compare damage evolution in columns for different connection details. To reduce the damage accumulation in the column, improved connection details are recommended in Section 6.2.

The position of lateral bracing for beams in V-type and inverted V-type braced frames is discussed next. The most common position for lateral bracing is at the intersection of braces and beam, *i.e.,* both top and bottom flanges are laterally braced at the section passing through the working point of braces at beams. As shown in Section 6.3, however, lateral bracing at this position may result in local buckling of gusset plates. More appropriate positions and methods to compensate for problems detected for currently recommended lateral bracing positions are suggested and evaluated.

Finnaly, Chen *et al.* (2008) found that for low-rise braced frames with short foundational periods, estimates of interstory drift based on elastic spectra diverge from

nonlinear response history analysis results for intense ground motions. An alterative interstory drift estimation method for low-rise braced frames that respond inelastically during strong earthquake ground shaking is suggested based on the Modal Pushover Analysis procedure. This method is discussed in Section 6.4.

The following questions are answered for all the four studies of steel braced frame behavior in this chapter.

1. Is fatigue life capacity of braces a function of slenderness ratios KL/r or width-thickness ratios b/t, or a function of both?

2. Which connection details mitigate damage accumulation in the columns?

3. Is there a more appropriate position of lateral bracing for beams than the intersection of braces and beam?

4. It is possible to better estimate the interstory drift for low-rise braced frames?

6.1 Brace proportions

The proportions of the braces in a SCBF system, including their slenderness and compactness, are critical when considering compressive buckling strength and, more importantly, the post-bucking hysteresis performance of brace members. It is well established that overall instability of braces, including overall compressive buckling strength and cyclic strength degradation, are mostly dependent on slenderness ratios

KL/r (Bruneau *et al.,* 1998; Galambos, 1998). In addition, the width-thickness ratio b/t has been shown to be a significant factor for fracture because of local instability, including local buckling and low-cycle fatigue (Goel, 1992; Hassan and Goel, 1991; Tang and Goel, 1989). Despite these advances, it is still unclear whether and how slenderness ratios KL/r affect the fatigue life capacity of braces, which is closely related to local instability.

Tremblay (2000) demonstrated that frames with very slender braces designed for compression strength behavior behave well because of the system overstrength inherent with their tension yielding, which results in a reduction in the fatigue life demand. Higher overstrength factor reducing the demand of fatigue life can be explained intuitively by Newmark and Hall's energy preservation for short period systems (Newmark and Hall, 1982); if the strength increases, the deformation and ductility demand decreases. Besides the overstrength factor, it is believed that fatigue life demand also depends on period and hysteresis of the structure, characteristics of ground motion, contribution of framing actions, *etc.* A separate systematic research on fatigue life demand is expected to be carried out and not considered in this research.

Regarding the fatigue life capacity, dependence on different factors has been proposed in existing literature: dependence on slenderness ratios KL/r only, dependence on width-thickness ratios b/t only, and dependence on both. Goel and his colleagues showed that the fatigue life capacity of a brace member depends on both slenderness ratios KL/r and width-thickness ratios $(b' - 2t)/t$ (equivalent to b/t in AISC Specifi-

cations). The fatigue life capacity is generally constant when slenderness ratios KL/r are smaller than 60 but increases with an increase in slenderness ratios KL/r when it is larger than 60 (Tang and Goel, 1987, 1989). They give:

$$N_f = \begin{cases} 262\dfrac{(b'/d')\,(60)}{[(b'-2t)/t]^2} & (KL/r \le 60) \\ 262\dfrac{(b'/d')\,(KL/r)}{[(b'-2t)/t]^2} & (KL/r > 60) \end{cases} \tag{6.1}$$

where N_f is accumulated tensile deformation normalized by tensile yield deformation, the width b' is the clear distance between webs and the depth d' is the clear distance between flanges. Based on the test results of Lee and Goel (1987) and Liu and Goel (1987), Tang and Goel (1987, 1989) observed that a larger slenderness ratio KL/r resulted in less severe local buckling and proposed that overall buckling also affects the fracture life capacity of the bracing members. Based on study of hysteresis behavior of bracing members in Jain and Goel (1978), Tang and Goel (1987, 1989) also proposed that the effect of the slenderness ratio KL/r is not considered in the fatigue life capacity when it is less than 60.

Lee and Goel (1987) proposed a refined fatigue life capacity formula, suggesting that the ductility depends on only compactness:

$$\Delta_f = 1335\frac{(46/F_y)^{1.2}}{[(b'-2t)/t]^{1.6}}\left(\frac{4b'/d'+1}{5}\right) \tag{6.2}$$

where Δ_f is the accumulated effective tension excursion of braces, defined as

$$\Delta_f = \sum (0.1\Delta_1 + \Delta_2) \tag{6.3}$$

In a tension half cycle of load-deformation loops of braces, Δ_1 is tension deformation from load reversal point to one third of tension yield strength of the brace $P_y/3$, and Δ_2 is tension deformation from one third of tension yield strength of the brace $P_y/3$ to end point of the tension half cycle.

Tremblay (2002) analyzed existing experimental data for braces with various slenderness and compactness ratios. He proposed that the normalized range in a cycle deformation history is a linear function of slenderness ratio KL/r.

$$\mu_f = 2.4 + 8.3\frac{kL}{r}\sqrt{\frac{F_y}{\pi^2 E}} \tag{6.4}$$

where μ_f is the peak-to-peak deformation range normalized by tensile yield deformation. Tremblay *et al.* (2003) later proposed that

$$\mu_f = 1 + \frac{2L}{D_y}\left[0.0455\left(\frac{b}{t}\frac{d}{t}\right)^{-0.1}\left(\frac{KL}{r}\right)^{0.3}\right] \tag{6.5}$$

where D_y is tensile yield deformation of the braces. These two equations suggest either no or little dependence on width-thickness ratios b/t.

Recently, Fell (2008) analyzed almost the same set of experimental data for braces, but proposed that the maximum range in a cyclic deformation history is a function of width-thickness ratios b/t:

$$\Delta'_f = \frac{L}{2}\left[\alpha\left(\frac{b'/2 + md'}{d'}\right)\left(\frac{b}{t}\right)^{\beta}\right]^2 \tag{6.6}$$

where Δ'_f is the peak-to-peak deformation range of braces, the width b' is the clear distance between webs, and the depth d' is the clear distance between flanges. Based

on experimental data, Fell (2008) suggested the plastic hinge length is given by $L_h = b'/2 + md'$, $m = 0.5$, $\alpha = 0.9$, and $\beta = -0.53$.

These conflicts of opinion regarding factors controlling fatigue life capacity arise from several reasons, the primary one being the characteristic of the experimental data itself. A comparison of the statistical data in Tremblay (2002) and Fell (2008) demonstrates that the specimens with higher ductility have larger slenderness ratios and smaller width-thickness ratios, and the specimens with lower ductility have smaller slenderness ratios and larger width-thickness ratios.

It is difficult to distinguish the contributions of these two parameters: does the ductility comes from larger slenderness ratios or smaller width-thickness ratios? The dispersion of ductility may also be attributed to variation of ductility measure, variation of deformation histories, and probable variations of steel fatigue properties. Clearly, more research is needed on this issue.

Therefore, in order to get a better understanding of how proportions and deformation histories effect ductility, experiments with one parameter altered at each step in the study would be necessary. This type of experiment is conducted numerically and presented in this section. The numerical perameter matrix is shown is Table 6.1. The first two parameters are width-thickness ratios b/t and slenderness ratios KL/r. For the hollow square section, the radius of gyration is proportional to the width b. Thus by changing thickness t and fixing width b, it is possible to vary b/t while keeping KL/r constant, and vice versa. The third parameter is the number of cycles

per deformation level. The forth parameter is the tension/compression asymmetry ratio. For a T/C asymmetry ratio of 3:1 and deformation range of 1.0, the peak tensile deformation is 0.75 and peak compressive deformation is 0.25. The deformation history imposed has an increasing amplitude level series of 0.5, 0.75, 1.0, 1.5, 2.0, 3.0, 4.5, 6.0, 7.5, 9.0, 10.5, and 12.0 times tensile yield displacement (range series of 1.0, 1.5, 3.0, 4.0, 6.0, 9.0, 12.0, 15.0, 18.0, and 21.0 times tensile yield displacement). Therefore, the fatigue life can be uniquely identified for a given deformation level to failure, where "failure" is defined here as cracking of three sides of a brace section and significant loss of strength (Figure 5.14).

Brace 1 in Table 6.1 used as the reference in these analyses is same size as the single brace described in the previous chapter (Section 5.2.1), with a b/t of 14.2 and KL/r of 50. The number of cycles per deformation level for the reference case is two, the tension/compression asymmetry ratio is 1:1. The corresponding deformation history is shown in Figure 6.1, and the deformation level to failure for the reference brace is $\mu_f/2 = 7.5$ (Figures 6.3b, 6.4b, 6.5b, 6.6b, and Table 6.1). Note that μ_f is the deformation range to failure normalized by tensile yield deformation, and $\mu_f/2$ is deformation level (deformation amplitude) to failure normalized by tensile yield deformation.

Numerical results are grouped and displayed in Figures 6.3 to 6.6, and deformation level to failure are summarized in Table 6.1. The influence of width-thickness ratios b/t is shown in Figure 6.3 demonstrating clearly that the width-thickness ratios b/t

have a pronounced effect on ductility capacity: the smaller the width-thickness ratios, the higher the ductility. As shown in Figure 6.4, however, even though it is clear that specimens with smaller KL/r have higher compressive buckling strength and tend to dissipate more energy within each cycle, it is more noticeable that they have an almost identical deformation level at failure. In other words, slenderness ratios have little effect on ductility capacity.

The number of cycles per deformation level also plays an important role (Figure 6.5). Obviously, increasing the number of cycles at a deformation level causes more cumulative plastic deformation (and thus more damage). This suggests that for a given ground motion, structures with shorter periods may experience more cycles and, thus, more damage for the same maximum drift is expected. Finally, for the asymmetry deformation history, bias in terms of compression leads to less ductility, as shown in Figure 6.6 which may be because compressive deformation is concentrated at the mid-span of the brace where local buckling occurs, but tensile deformation is distributed along the length of brace.

Based on numerical analysis, it is evident that fatigue life capacity is heavily dependent on width-thickness ratios b/t and deformation histories. Slenderness ratios KL/r appear to have negligible, if any, effect on fatigue life capacity. It is worth noting that slenderness ratios KL/r may reduce fatigue life demand (Tremblay 2000; Uriz 2005). Careful experimental validation of these observations from numerical simulations is advised.

Based on the above discussion and evaluation on fatigue life capacity, the following important parameters for its counterpart, fatigue life demand, are suggested. Fatigue life demand may be specified as the demanded deformation history of a brace, *e.g.,* corresponding to two interstory drift cycles of 2% followed by three interstory drift cycles of 1%. In this sense, the fatigue life demand is, essentially, a loading protocol for braces. The four most important basic parameters for realistic loading protocols are numbers, amplitudes, sequence and asymmetry of cycles.

These four parameters depend on many factors:

- First, they depend on intensity [*e.g.,* peak ground acceleration (PGA) and duration] and frequency content of ground motion, which in turn depend on magnitude of the earthquake, distance from epicenter, soil type at the site, etc.

- Second, they depend on configuration, strength, stiffness, and modal properties (periods and participation factors) of the structure, as well as the contribution of framing beam and column members, and the effects of response modification coefficients (R factors) and system overstrength factors (Ω_0 factors) (ASCE 7-05).

- Third, they depend on the deterioration characteristics of the structure. For braces frames, compressive strength, overstrength factor and resistance to the cyclic degradation of braces may depend on the slenderness ratios KL/r as well as steel yield strength F_y. All these factors are equally important and interact

with each other. For example, the period of a structure has a significant effect on the response to near-fault ground motions; compressive strength, overstrength factor, and slenderness ratios KL/r may be not fully independent of each other and they may be reduced to a smaller number of independent factors.

There are many decisions and judgements to be made in developing a loading history that is statistically representative of the full range of ground motions and structural characteristics. A detailed discussion of the development of loading histories for steel moment frames and wood frames structure which are good guidelines for future development of fatigue life demand for braced frame systems can be found in Krawinkler *et al.* (2000a, b). For braced frame systems, it is recommended that several variations be considered, including consideration of both "ordinary" and near-fault ground motions, the duration of earthquake versus the period of structure, the slenderness ratios KL/r and resulting overstrength factor, and steel yield strength F_y and hardening properties. Other variation of parameters should also be considered, with the cumulative damage concepts kept in mind. Considering both a series of response history analyses of single-story braced frame systems and a statistical analysis of the response history of brace deformation, a representative loading history can be developed with proper numbers, amplitudes, sequence, and asymmetry of cycles.

Once the deformation history or the fatigue life demand is developed, code requirements for brace proportions can be determined. For example, if the following assumptions are met:

1. The reference history in this parametric study (Figure 6.1) is a typical deformation history.

2. The plasticity and damage properties calibrated against Yang and Mahin (2005) in this research are typical material properties for ASTM A500 Grade B steel.

3. The braced frames have 45 degrees brace orientation, and the nominal yield strain of braces is $\varepsilon_y = 0.16\%$ approximately.

then from a normalized deformation level to failure for different width-thickness ratios b/t summarized in Table 6.1, a relationship can be developed between interstory drift ratios to failure and width-thickness ratios b/t. For example, for $b/t = 14.2$, the deformation level to failure is 7.5 times the yield deformation. by assuming 45-degree braces, the interstory drift to failure is $2 \times \varepsilon_y \times 7.5 = 2.4\%$. This relationship is shown in Figure 6.2. Based on this relationship, in order to achieve interstory drift capacity without failure at 2.5%, the limiting width-thickness ratio b/t is 13.1.

Alternatively, test protocols of the "pass or fail" type proposed by Tremblay and Bouatay (2002) may be used to determine the limiting with-thickness ratios b/t. In this type of test, a brace system is said to be adequate if it survives the applied displacement history. The largest width-thickness ratio b/t of survivals is the critical factor. Tremblay and Bouatay's deformation histories do not include all the variations discussed herein. In particular, they are independent of structural properties (such as the slenderness ratios KL/r), which may be important based on observations

by Tremblay (2000); the histories were proposed with careful consideration of the individual effects of four ground motion types.

The four proposed deformation histories adopted in current research represent crustal (intra-plate) rich high frequency earthquakes that occur in Eastern North America that are richer in high frequency, crustal earthquake occurring along the Pacific coast, west coast near-field ground motions that are characterized by large acceleration pulses leading to high ground velocity and displacement, and earthquakes occurring along the Cascadia subduction zone. These four deformation histories are shown in Figure 6.7. In order to show clearly the failure of unsatisfying braces, a tensile excursion is appended at the end of the original histories. "Failure" is defined here as cracking of three sides of a brace section and a significant drop of strength, and the appended tensile excursion and corresponding resistance response are purely for visual demonstration of the failure ("strength lost" or "strength recovered" annotated in Figures 6.8 to 6.11).

When a braced frame is subjected to a interstory drift history, one brace in the pair is in tensile deformation while the other is in compressive deformation — and vice versa — if deformation of beam is ignored. Based on the previous parametric analysis in this section, compressive asymmetry causes more damage. Therefore, the deformation histories applied to braces are the ones biased in terms of compression, *i.e.,* only the braces with greater compressive deformation are analyzed, as they are related to the limiting width-thickness ratios.

Braces with different width-thickness ratios b/t are analyzed using these four "pass or fail" type loading protocols. The results are shown in Figures 6.8 to 6.11 for four loading histories, respectively. For both west crustal events at distance and west near-field events, the critical width-thickness ratios b/t are 13.2. Braces with width-thickness ratios less than 13.2 will survive the applied displacement history. For east crustal events at distance and west subduction events, the critical width-thickness ratios b/t are 16.4 and 15.9, respectively. The critical width-thickness ratios for four loading histories are summarized in Table 6.2.

	b/t	KL/r	No. of cycle	T/C	$\mu_f/2$
1	14.2	51	2	1/1	7.5
2	8.1	51	2	1/1	10.5
3	28.2	51	2	1/1	6.0
4	14.2	32	2	1/1	7.5
5	14.2	70	2	1/1	7.5
6	14.2	100	2	1/1	7.5
7	14.2	51	1	1/1	9.0
8	14.2	51	3	1/1	6.0
9	14.2	51	2	3/1	7.5
10	14	51	2	1/3	6.0

Table 6.1: Numerical experiment matrix for brace proportion

Event	b/t	Pass/Fail	Peak Def.	Peak IDR*
East crustal events at distance	15.3	Pass	$5D_y$	1.6%
	16.4	Pass		
	17.6	Fail		
West crustal events at distance	12.5	Pass	$7D_y$	2.2%
	13.2	Pass		
	14.2	Fail		
West near-field events	12.5	Pass	$12D_y$	3.8%
	13.2	Pass		
	14.2	Fail		
West subduction events	14.9	Pass	$5D_y$	1.6%
	15.9	Pass		
	17.0	Fail		

* Peak Interstory Drift Ratios are calculated by assuming the angle of braces are 45 degrees and the nominal yield strain of braces is $\varepsilon_y = 0.16\%$

Table 6.2: Numerical results of "pass or fail" type loading histories

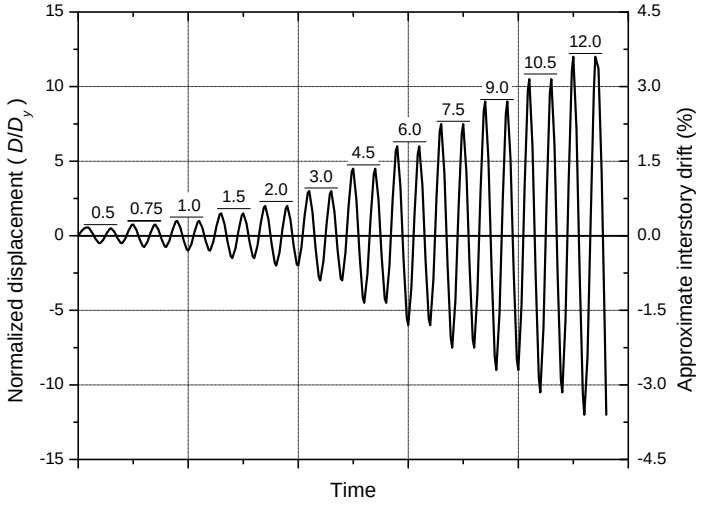

Figure 6.1: Deformation history for reference brace

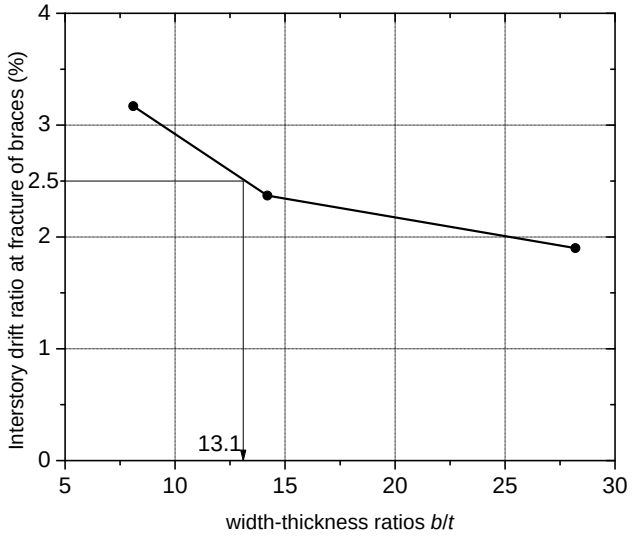

Figure 6.2: Interstory drift ratios to failure versus width-thickness ratios

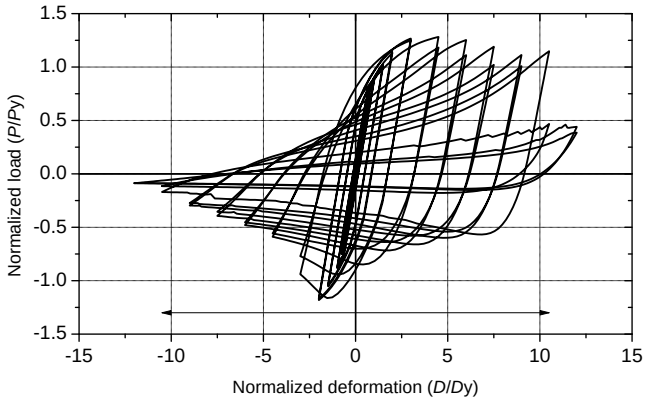

(a) $b/t = 8.1$

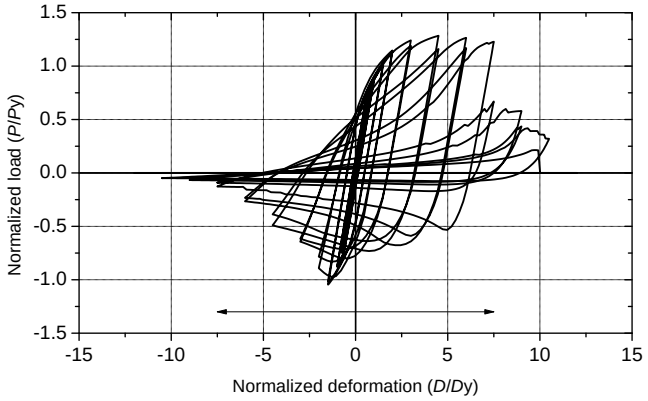

(b) $b/t = 14.2$

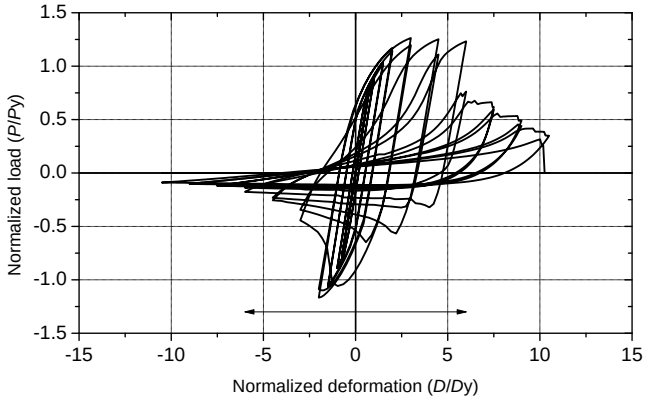

(c) $b/t = 28.2$

Figure 6.3: Influence of width-thickness ratios b/t ($KL/r = 51$)

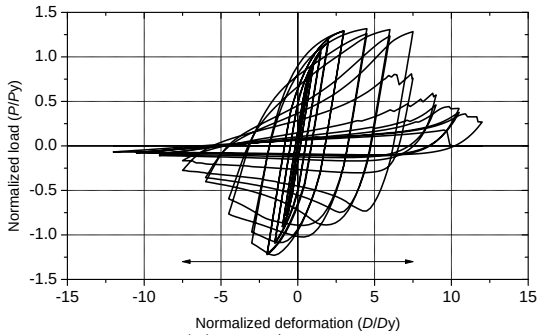

(a) $KL/r = 32$

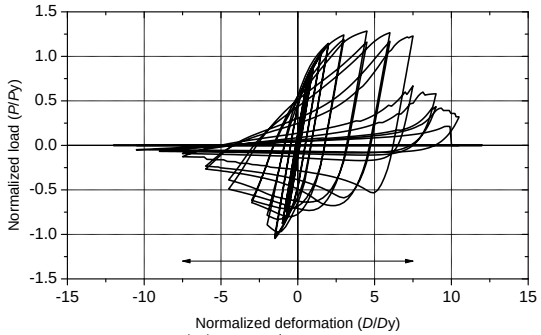

(b) $KL/r = 51$

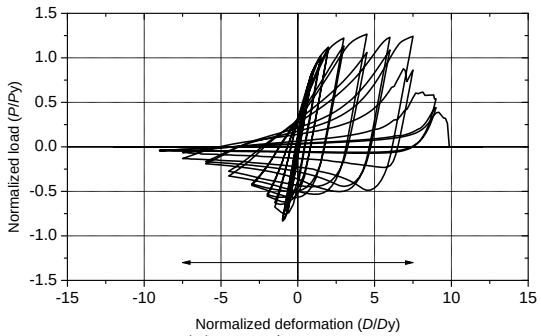

(c) $KL/r = 70$

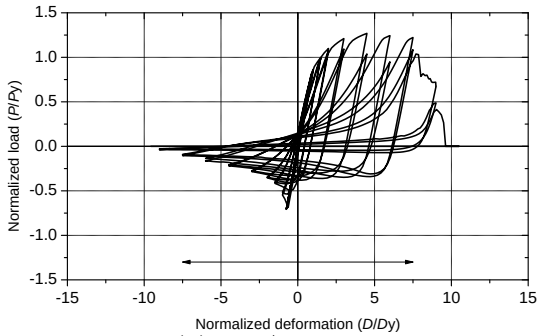

(d) $KL/r = 100$

Figure 6.4: Influence of slenderness ratio KL/r ($b/t = 14.2$)

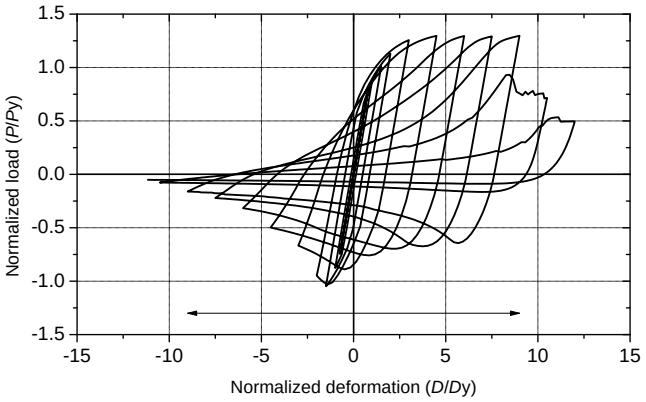

(a) 1 cycle per deformation level

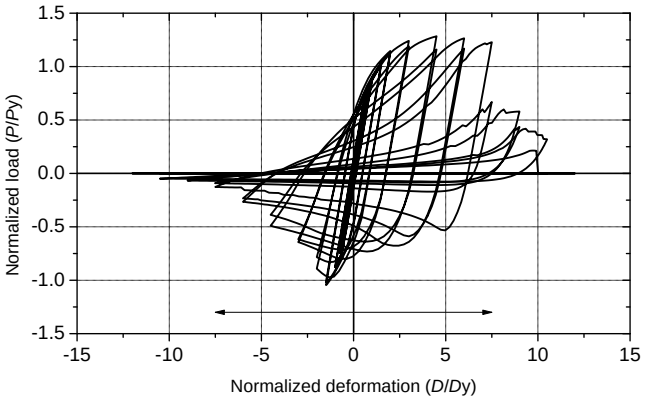

(b) 2 cycles per deformation level

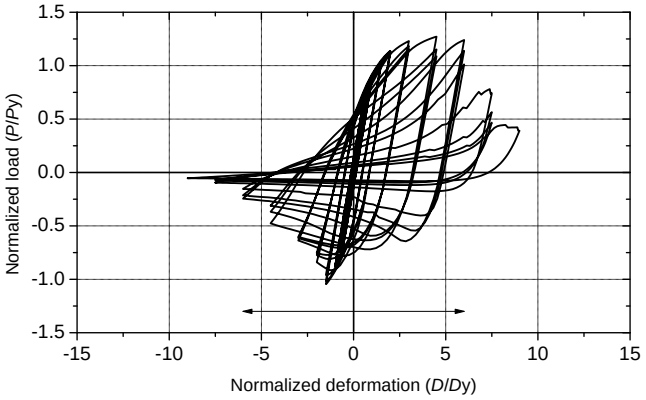

(c) 3 cycles per deformation level

($b/t = 14.2$, $KL/r = 51$)

Figure 6.5: Influence of number of cycles per deformation level

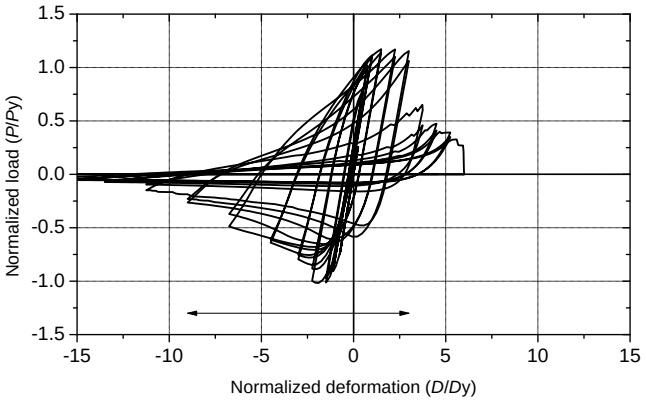

(a) tension:compression=1:3

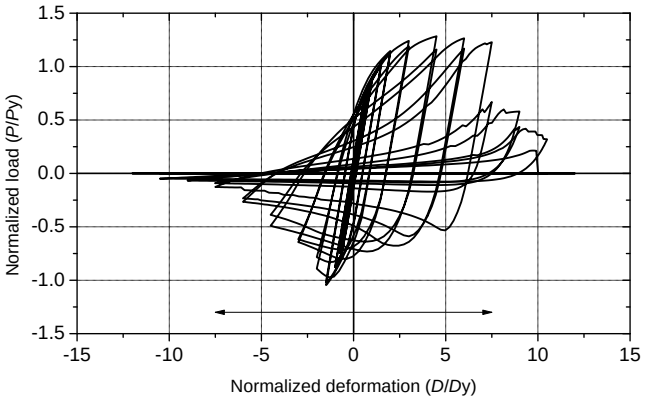

(b) tension:compression=1:1

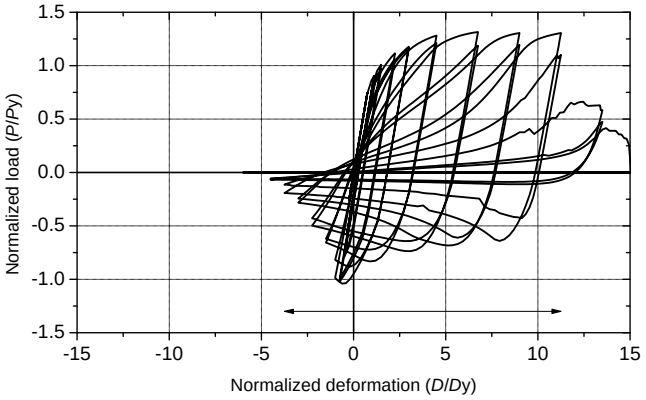

(c) tension:compression=3:1

($b/t = 14.2$, $KL/r = 51$)

Figure 6.6: Influence of tension/compression asymmetry ratio

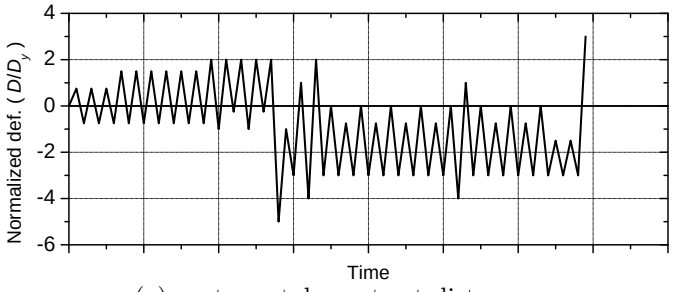

(a) east crustal events at distance

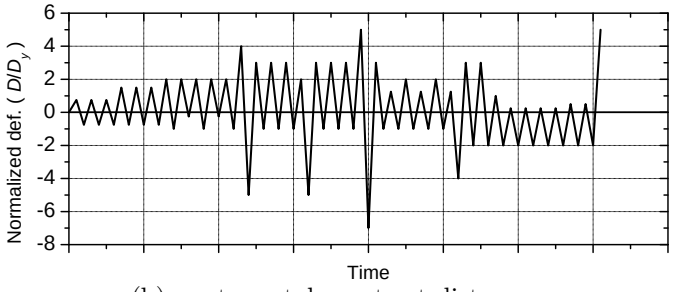

(b) west crustal events at distance

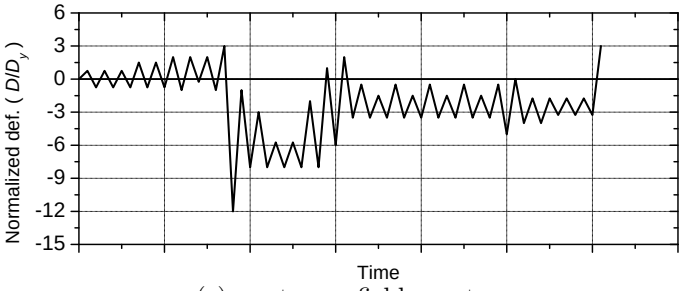

(c) west near-field events

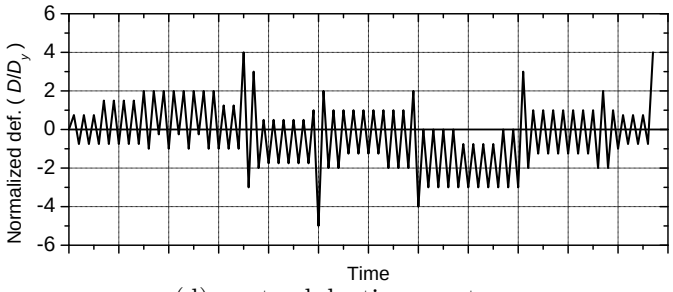

(d) west subduction events

Figure 6.7: Deformation histories (Tremblay and Bouatay, 2002)

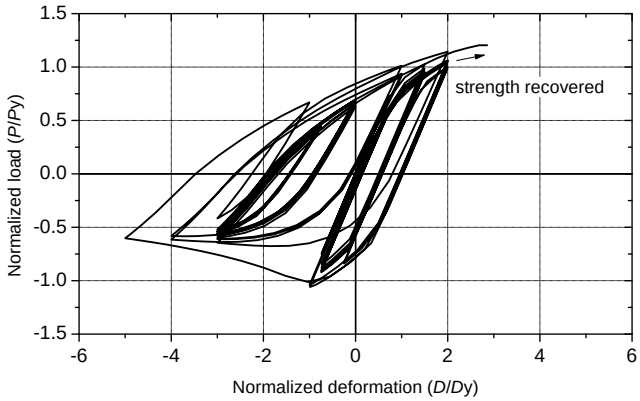

(a) $b/t = 15.3$, pass

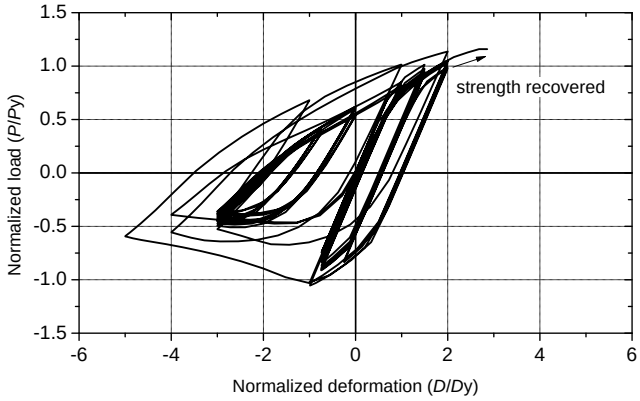

(b) $b/t = 16.4$, pass

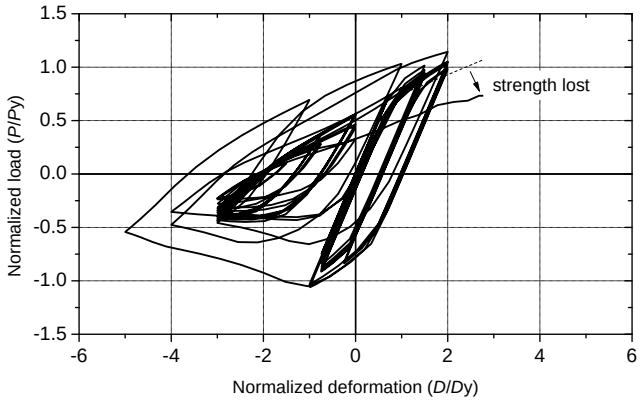

(c) $b/t = 17.6$, fail

Figure 6.8: Critical width-thickness ratios b/t for east crustal events at distance

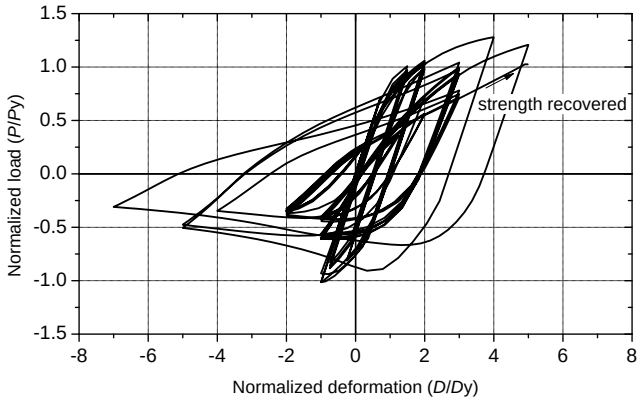

(a) $b/t = 12.5$, pass

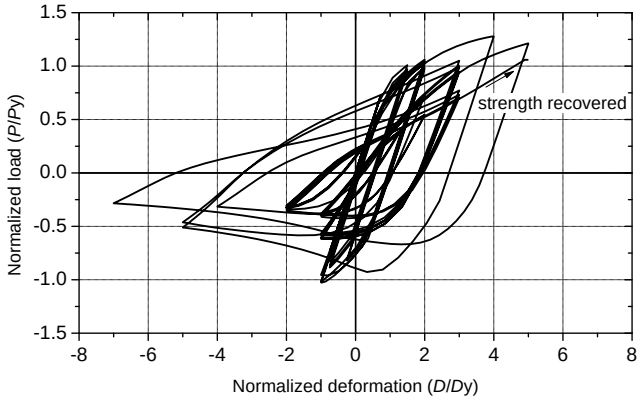

(b) $b/t = 13.2$, pass

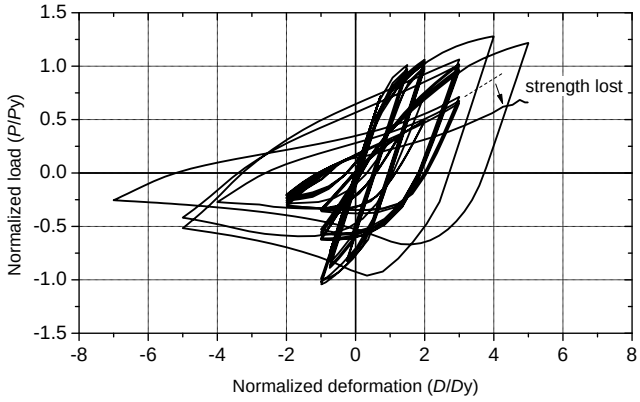

(c) $b/t = 14.2$, fail

Figure 6.9: Critical width-thickness ratios b/t for west crustal events at distance

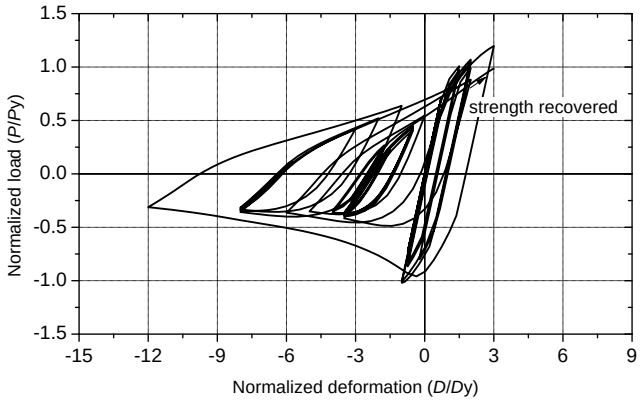

(a) $b/t = 12.5$, pass

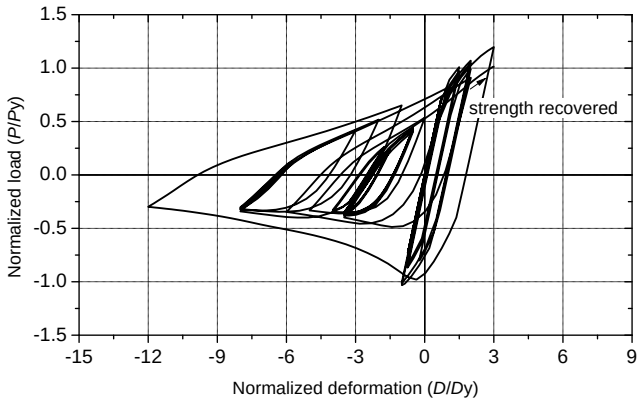

(b) $b/t = 13.2$, pass

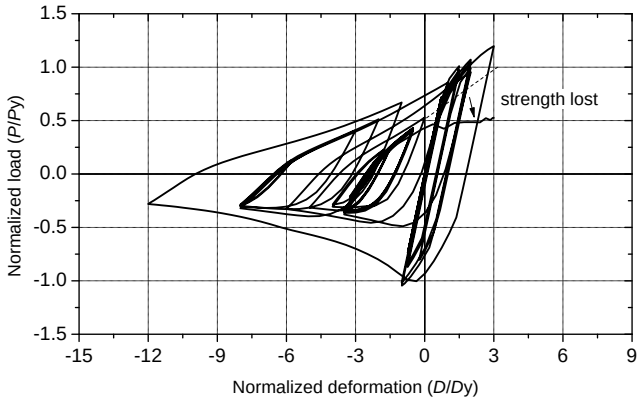

(c) $b/t = 14.2$, fail

Figure 6.10: Critical width-thickness ratios b/t for west near-field events

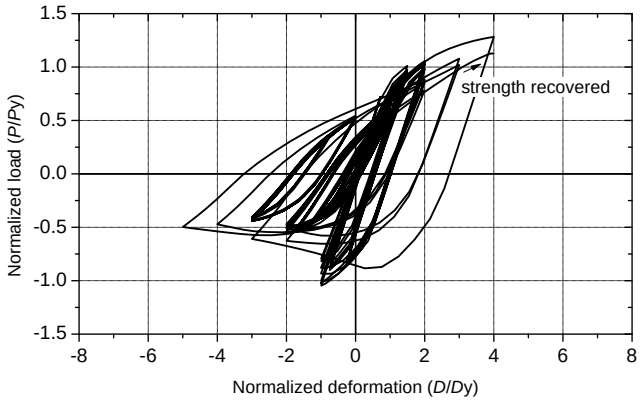

(a) $b/t = 14.9$, pass

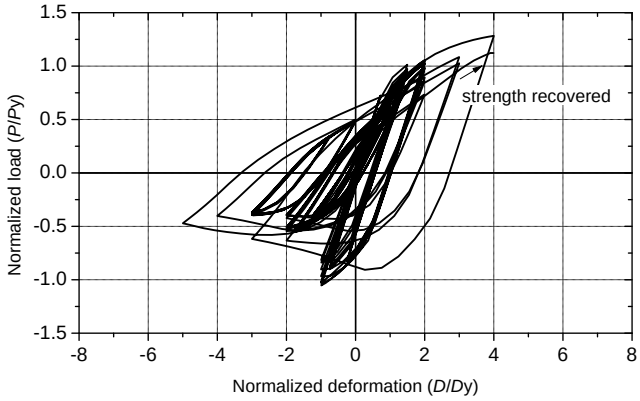

(b) $b/t = 15.9$, pass

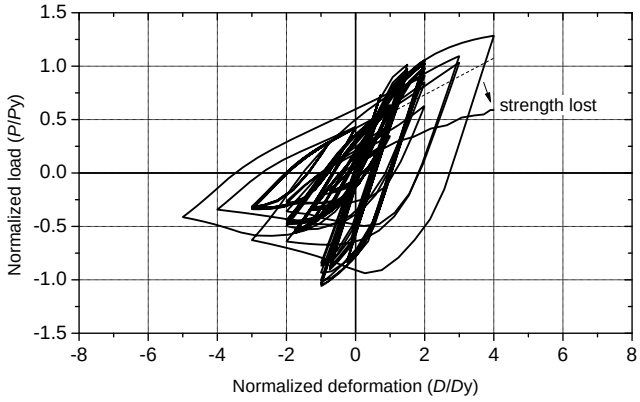

(c) $b/t = 17.0$, fail

Figure 6.11: Critical width-thickness ratios b/t for west subduction events

6.2 Connection details

The AISC Provisions place a great deal of emphasis on brace-to-gusset connection details. Although the connection between brace and the frame is strengthen by the gusset, the "rigid" zone created by the beam-column connection and the gusset plate generate more deformation and damage to member immediately surrounding the zone: the column and the beam. This may result in cracks in column flanges and webs, as seen in the inverted-V type SCBF test discussed in previous chapter, or cracks in beam flanges and webs, as seen in BRBF test in Uriz (2005).

Several methods for reducing damage accumulation in the column are analyzed in this section, including:

1. Reduced depth (Figure 6.14). When the depth of column is reduced, there are two effects. First, the stiffness and strength of the column is reduced; second, for the a given curvature, the strain at outer fiber will decrease with decreasing section depth. These two effects counteract each other, and together may help alleviate damage in the column.

2. Thickened web (Figure 6.15). Thickening the web increases the stiffness and strength of the column. Stiffness and a stronger column will have less deformation and damage.

3. Thickened flanges (Figure 6.16). Thickening the flanges has similar effect as the thickened web. Because the flange has more outer fibers, thickening the flanges

are expected to be more effective.

4. Stiffener (Figure 6.18). There is a tensile component of interface force between beam and column. A stiffener may distribute the tensile force and reduce damage at the column.

5. Reinforcing plates at the flanges (Figure 6.19). The reinforcing plates locally strengthen the damage zone of the column.

6. T-shear tab (Figure 6.20). A T-section shear tab is a variation of the reinforcing plate, but easier to manufacture and install.

7. Welded flanges (Figure 6.21). After the flanges of beam and column are welded, it provides a more uniform interface force transfer than a shear tab.

8. Stiffener and welded flanges (Figure 6.22). Combine the stiffener and welded flanges and create a standard moment connection.

The two-story SCBF used in this numerical analysis is identical to the one discussed in previous chapter, which was subjected to a displacement history at the top of the frame. Critical damage state of steel material was 0.5 (typical value, Lemaitre, 1992), beyond which is considered failure. The history of maximum damage at the column was recorded and compared in Figure 6.12. Modification methods listed in the legend are sorted by damage state, with the largest damage state history at the top.

The numerical analysis shows that strengthening the column uniformly (reduced depth, thickened web, and thickened flanges) is, in general, less effective than strengthening the column locally at the damage zone. Reinforcing plates are the most effective method. Unfortunately, this is the least feasible method because it is difficult to access the weld near beam web. The use of a stiffener and a combination of stiffener and welded flanges are good candidates for effective damage reduction methods.

The combination of stiffener and welded flanges results in more damage than using the stiffener by itself because the connection becomes more rigid. As displacement history at the top of frame is prescribed, rigid connections lead to more deformation at the column. For structures subjected to earthquake ground motion, more rigid connections lead to higher stiffness, which generally results in less overall deformation. Therefore the difference between using a stiffener and a combination of a stiffener and welded flanges are expected to be less. Finally, the combination of a stiffener and welded flanges is a standard moment connection, which can be easily designed by structural engineers. Based on these considerations, the combination of a stiffener and welded flanges are recommended.

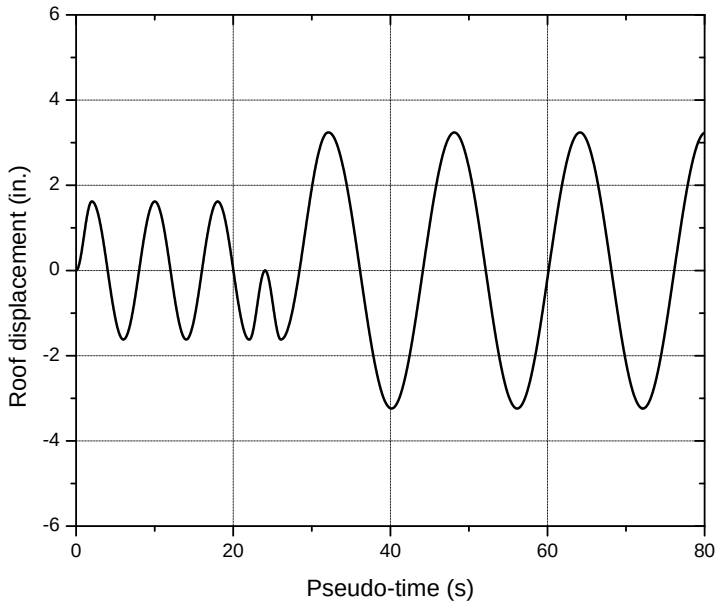

(a) Displacement history

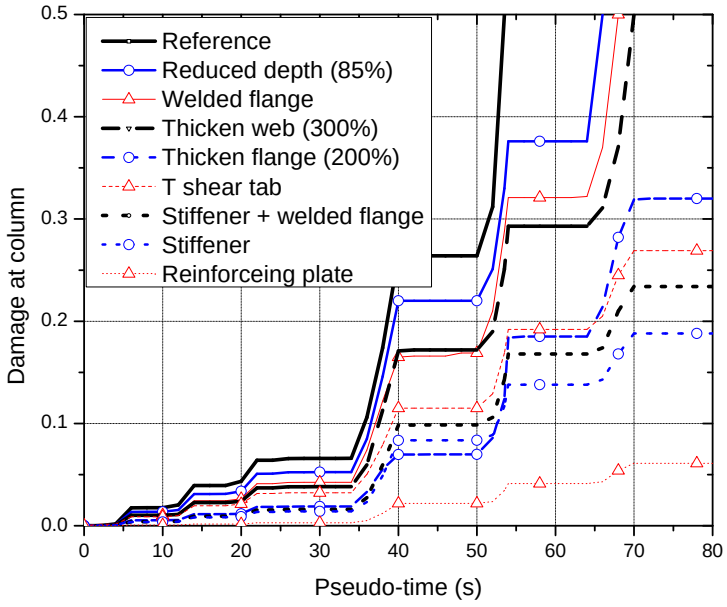

(b) Damage history

Figure 6.12: Damage evolution for different strengthening methods

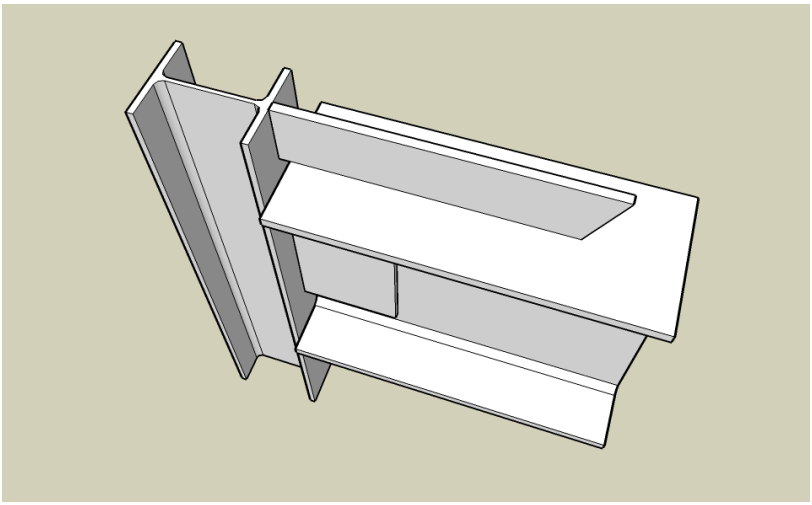

Figure 6.13: Details of column: reference

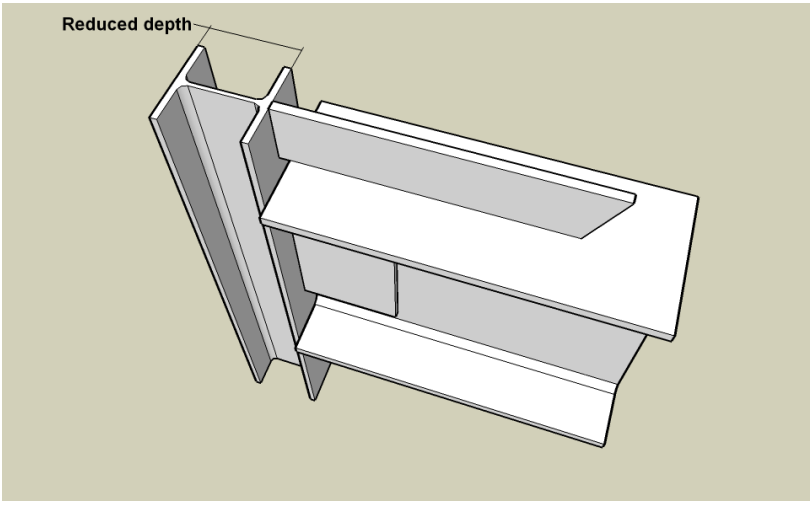

Figure 6.14: Details of column: reduced depth

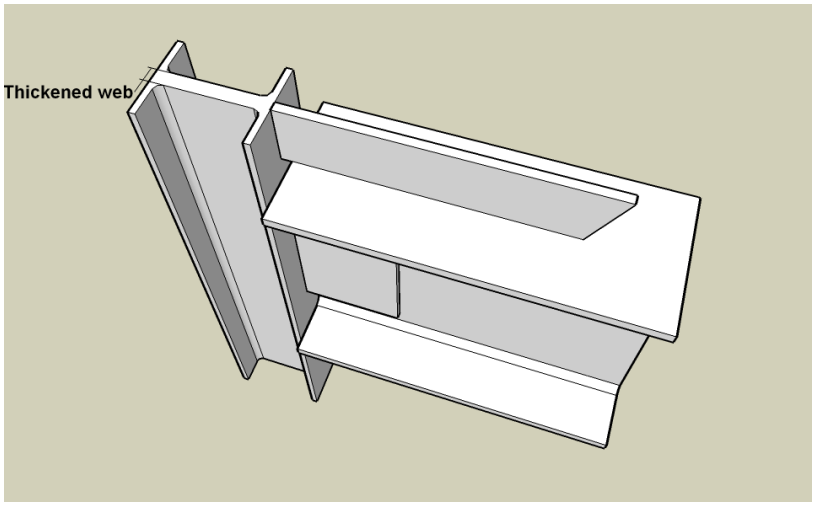

Figure 6.15: Details of column: thickened web

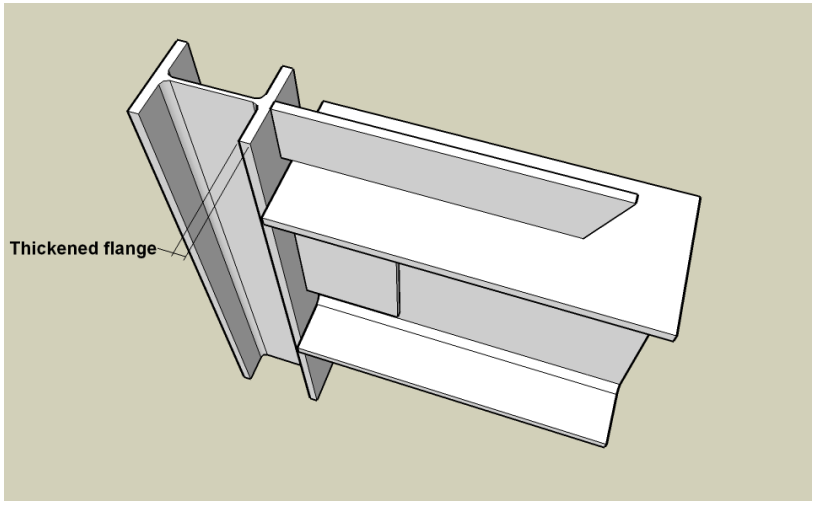

Figure 6.16: Details of column: thickened flange

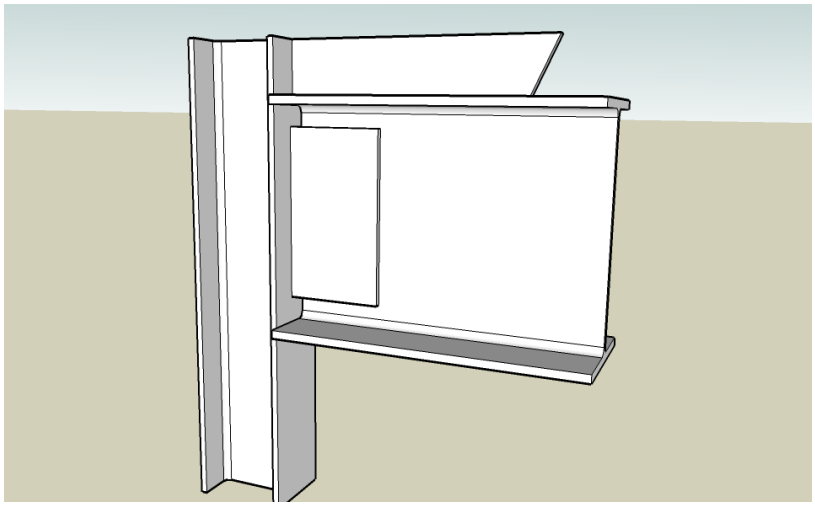

Figure 6.17: Details of reinforcement: reference

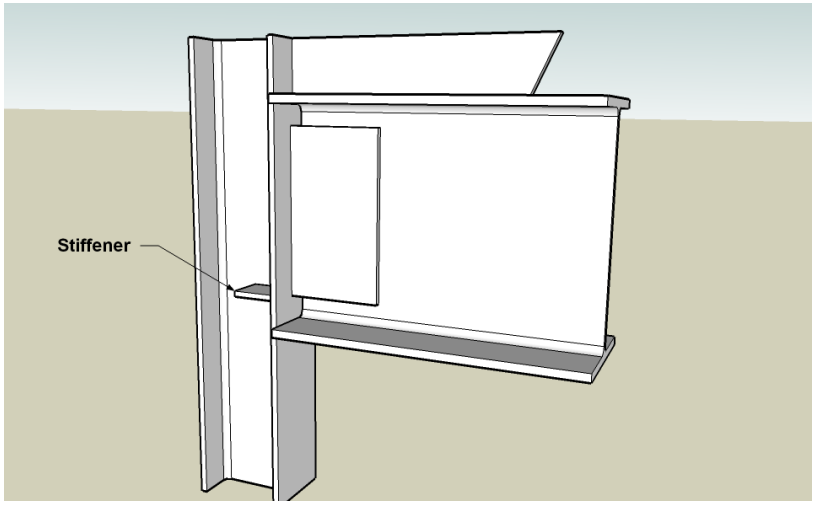

Figure 6.18: Details of reinforcement: stiffener

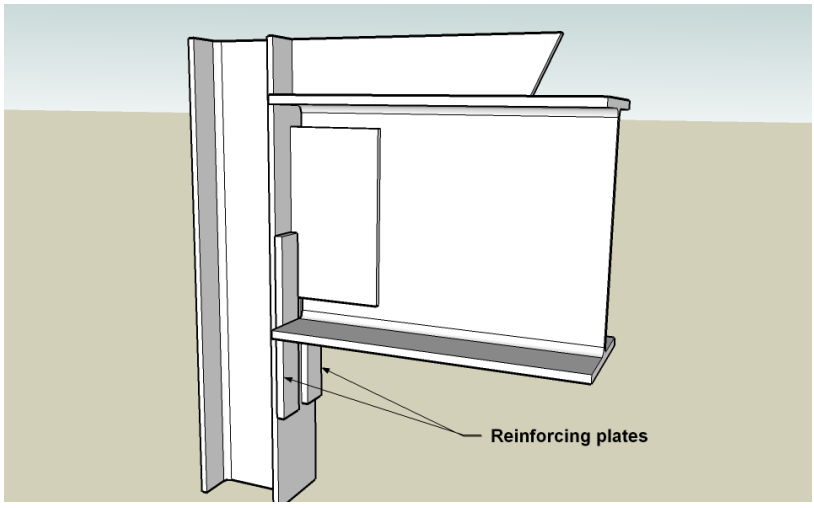

Figure 6.19: Details of reinforcement: reinforcing plates

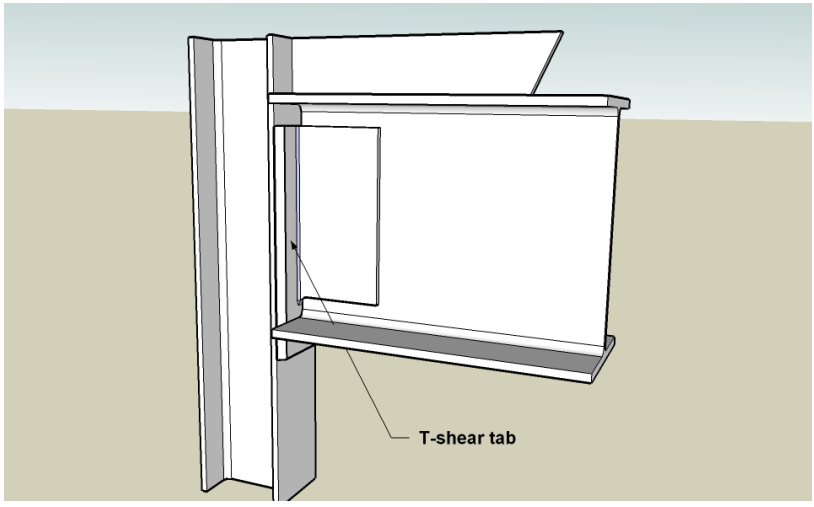

Figure 6.20: Details of reinforcement: T-shear tab

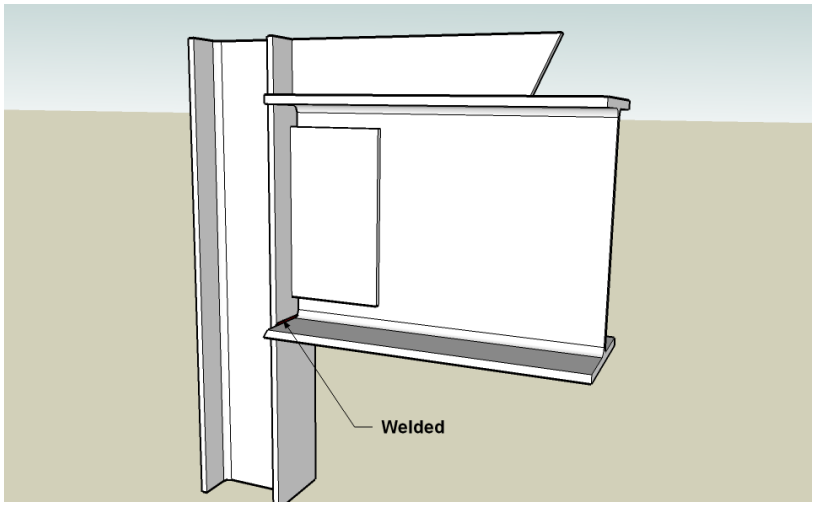

Figure 6.21: Details of reinforcement: welded flanges

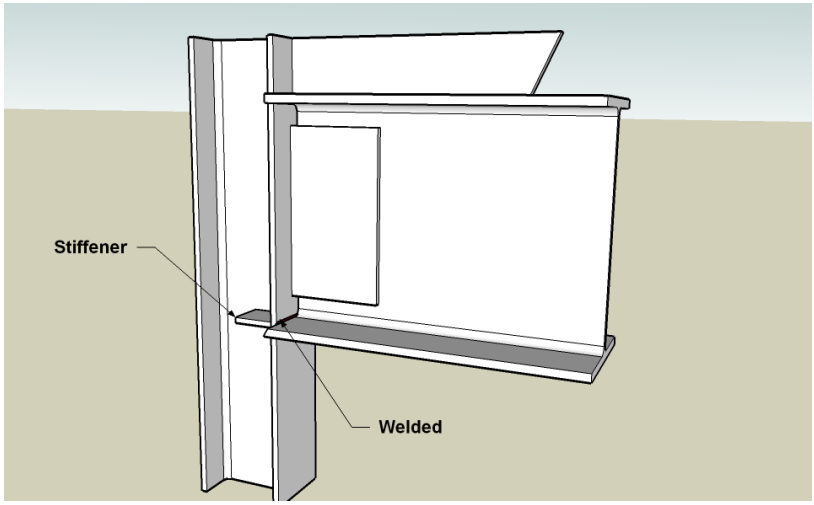

Figure 6.22: Details of reinforcement: stiffener and welded flanges

6.3 Lateral bracing for beams

For V-type and inverted V-type braced frames, beam top and bottom flanges must be laterally braced at the intersection of the braces and beam. Bracing is to resist the beams rotation about its longitudinal axis (lateral-torsional buckling), in accordance with the AISC Seismic Provisions. Although AISC specifies the required brace strength and stiffness, the term "intersection of braces and beam" is not precisely defined. In an idealistic model, braces are pin-connected to beam at the mid-span point. But in reality, the brace-gusset-beam connection is not a point but a region. Thus, there are at least two bracing configurations: one where the lateral bracing is at the middle of the beam, and another where two lateral bracing members are provided, one at each end of the gusset plate (Figure 6.23). Note that the lateral bracing members at the top flanges and continuous bracing by the slab are not shown in the figures. Although the first configuration is most common in structural engineering practice, the second one might be more appropriate. For example, consider:

1. For special moment frames, the Seismic Provisions (Section 9.8) require that lateral bracing members for beams shall be placed at locations where changes in cross-section occur and where analysis indicates formation of a plastic hinge. For SCBFs, at the edges of the gusset plate, the cross section changes because the gusset plates enhance beam bending stiffness. Moreover, because of the vertical unbalanced load, it is possible that a plastic hinge in the beam will form at the ends of the gusset plate during inelastic deformation of the braced

frame. To this end, placing lateral bracing members at the gusset plate edges would be consistent with practices for special moment frames.

2. Gussets are typically detailed in accordance with Seismic Provisions Commentary Section C13.1. This results in a fixed-fixed with sidesway buckling configuration for the gussets, with coefficient $K = 1.2$ (AISC 2006). As the brace-gusset-beam connection is not rigid region out-of-plane, the configuration with lateral bracing members at the edge of the gusset (Figure 6.23b) is more likely to satisfy the fixed-end condition, typically assumed in design practice.

Analysis results of braced frames with the two types of bracing configurations subjected to earthquake ground motion are compared. Structural parameters of the braced frame are described in Section 6.4. The SAC LA32 ground motion that was randomly chosen and is large enough to buckle the braces, was applied to the structure. The comparison of first-story hysteretic loops is shown in Figure 6.24 and comparison of behaviors is shown in Figure 6.25 and 6.26. As can be seen, the gusset with lateral bracing member at the middle buckled out of plane, and then lead to lateral torsional buckling of beam, as well as a plastic hinge at the beam right next to the connection (Figures 6.25b, 6.26b). The configuration with two lateral bracing members at the edges of gusset provided sufficient stiffness against torsion of beam and boundary rotation of gusset buckling configuration; therefore, energy dissipation was localized at braces, which is ideal for SCBFs.

A braced frame with only one lateral bracing member at the middle, but with a thicker gusset design with fixed-pin with sidesway buckling assumption was also analyzed. The result is similar to the two-lateral-bracing-member configuration, with buckling localized in braces.

Alternatively, in-plane buckling connection might be used to reduce twisting forces on the beam. An example of this kind of connection (Rutherford and Chekene, 2008) is shown in Figure 6.27. In order to eliminate the out-of-plane buckling mode of the gusset-brace-gusset component, the out-of-plane bending stiffness at the ends of the component has to be increased. Here, stiffeners are used strengthen the gusset and prevent it from compression buckling. Thickening of the gusset and incorporating a gusset stiffener effectively increase the out-of-plane radius of gyration, thereby increasing its compression buckling strength. Thus, the in-plane bucking connection is also helpful when only one lateral bracing member at the middle is feasible. Analysis results of the same braced frame but with in-plane buckling connection include is shown is Figure 6.28. The energy dissipation is again localized in the braces, and buckling of gusset is prevented.

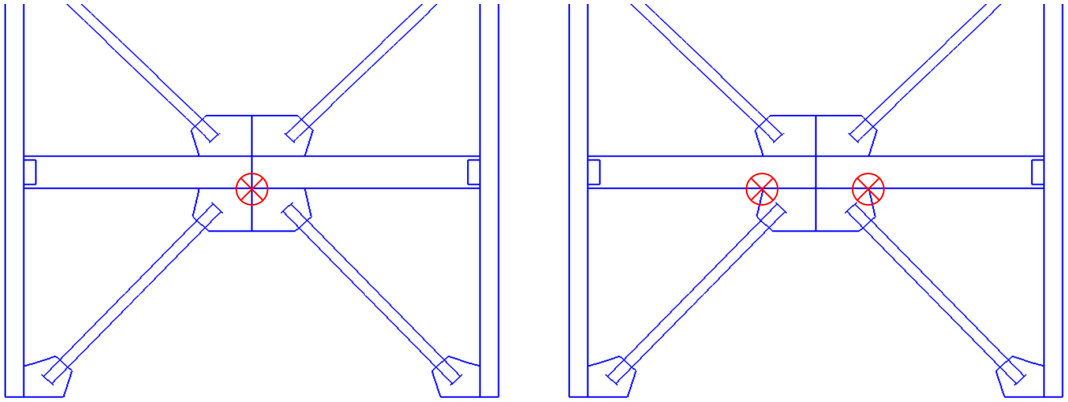

(a) At the middle of the beam (b) At each end of the gusset plate

Figure 6.23: Schematics of two lateral bracing configurations

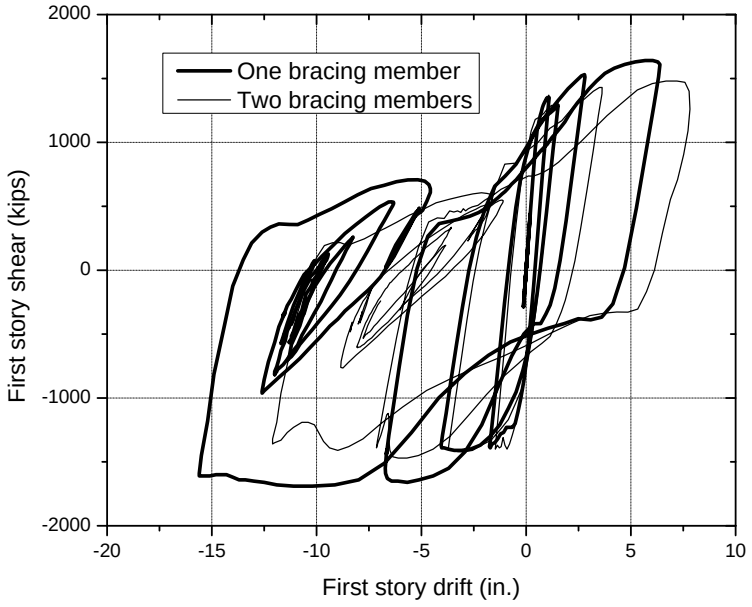

Figure 6.24: Comparison of first-story hysteretic loops

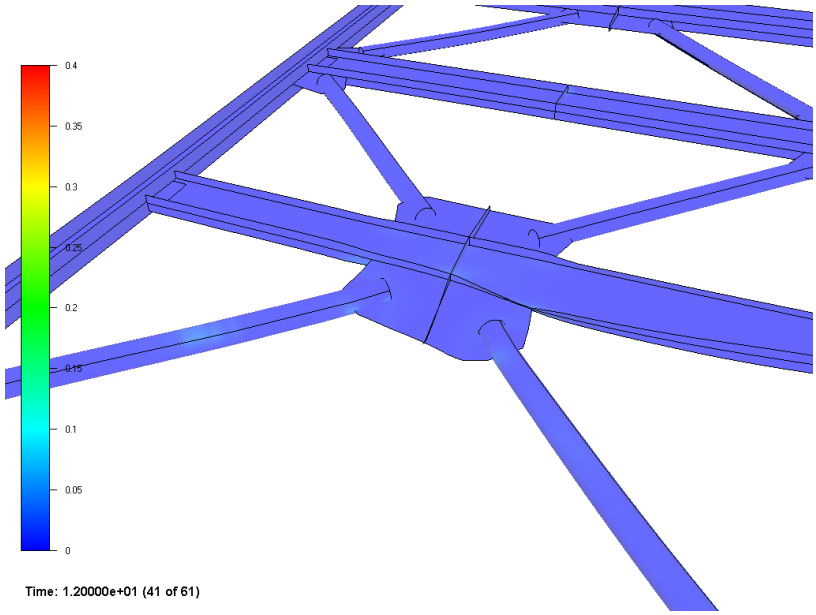

(a) One lateral bracing member at the middle

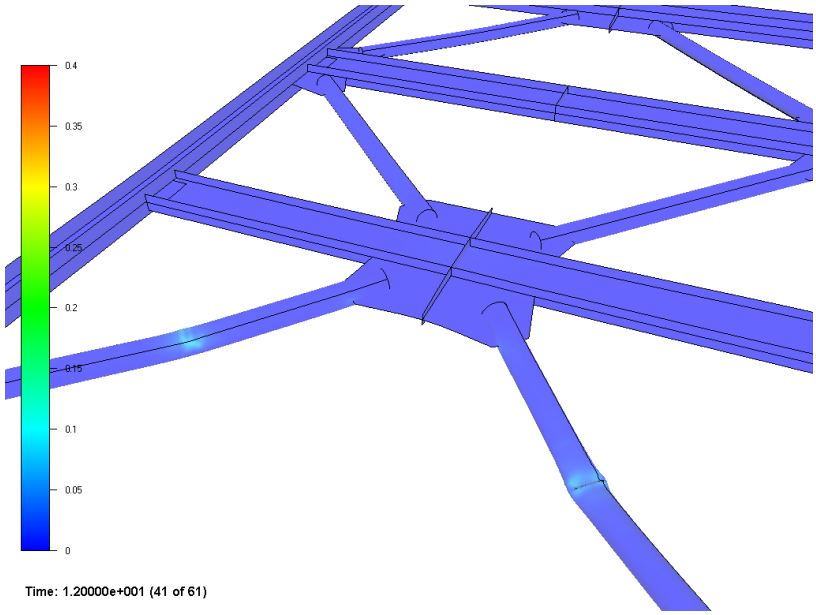

(b) Two lateral bracing members at the edge of gusset plate

Figure 6.25: Damage modes for drift to the right

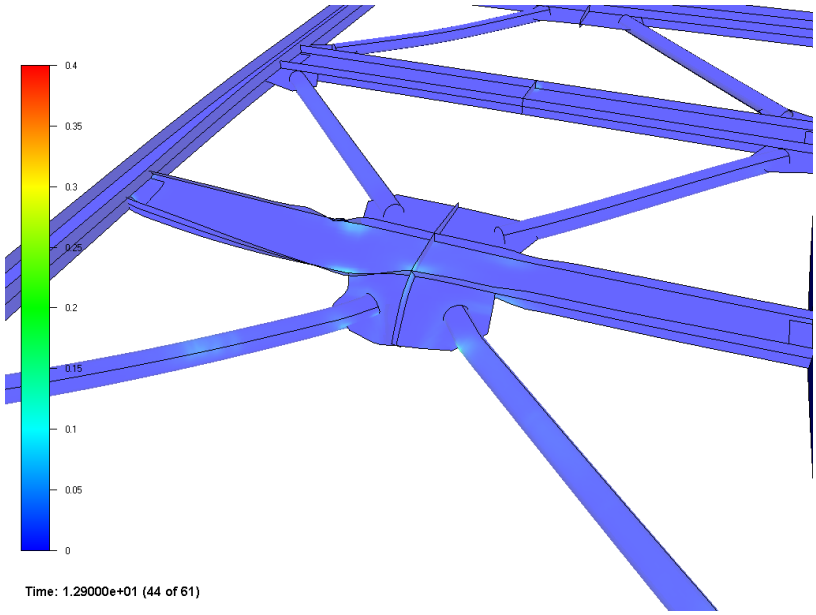

(a) One lateral bracing member at the middle

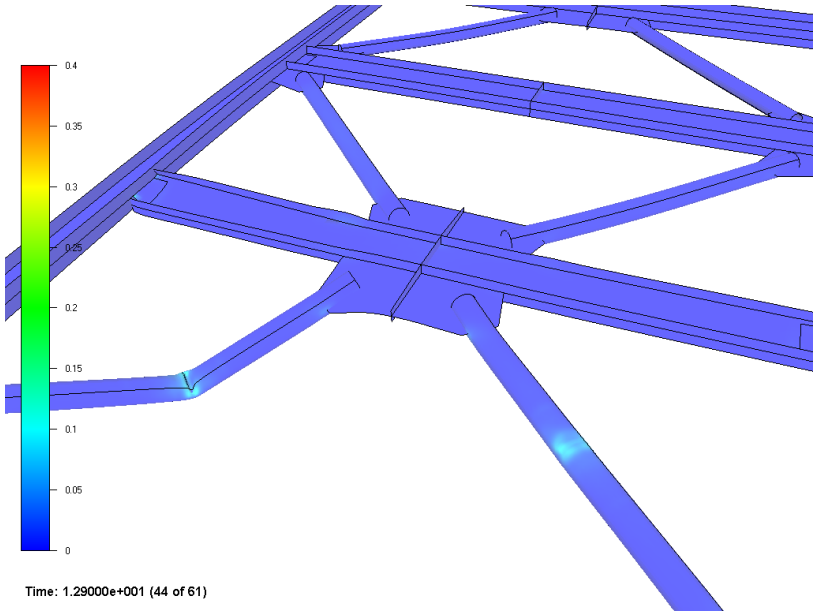

(b) Two lateral bracing members at the edge of gusset plate

Figure 6.26: Damage modes for drift to the left

Figure 6.27: Detail used to induce in-plane buckling of braces

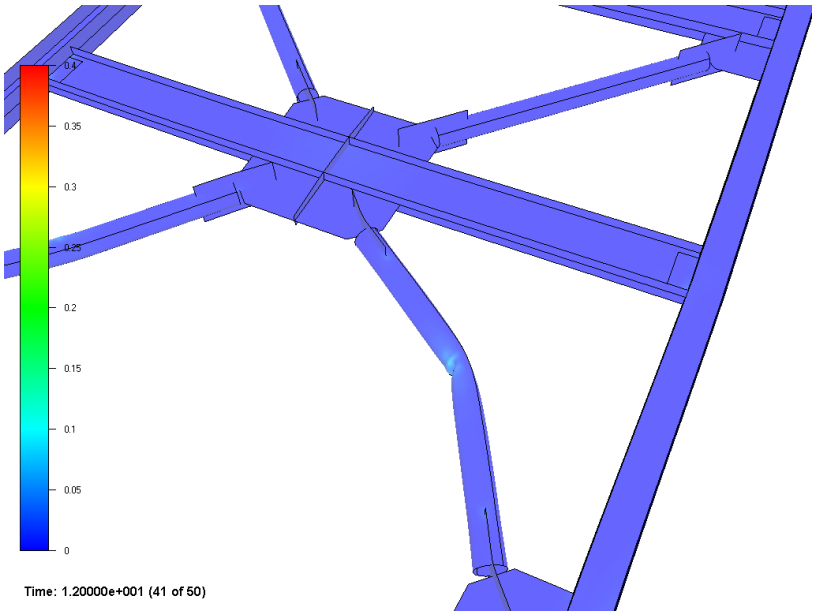

Figure 6.28: Analysis result of in-plane buckling of braces

6.4 Estimate of interstory drift demands

For moment frames, and tall braced frames, which have relatively long fundamental periods falling into the Newmark and Hall displacement-preserved range (Newmark and Hall, 1982), the elastic spectral analysis may give a reasonably conservative estimate of average drift demands for inelastic systems. In other words, for short period braced frames, the estimation based on elastic spectra is relatively poor. It is not clear whether equivalent nonlinear modal analysis, namely Modal Pushover Analysis (MPA), can be used to realistic estimate interstory drift for low-rise braced frames. In this section, a three-story SCBF structure is evaluated using nonlinear response history analysis (RHA) and MPA, and results compared. A new method for pushover analysis using a multiple point constraint is derived based on the principle of virtual work and presented in Appendix A.

The nonlinear static procedure or pushover analysis (FEMA 273, FEMA 356) has been adopted by structural engineers as a building evaluation tool for seismic demands estimations. Based on structural dynamics theory, while retaining the simplicity of existing pushover analysis, the MPA procedure was developed to include modal contributions that may be significant to seismic demands (Chopra and Goel, 2002). The procedure has been applied to SAC buildings (Goel and Chopra, 2004), heightwise regular generic frames (Chintanapakdee and Chopra, 2003) and irregular generic frames (Chintanapakdee and Chopra, 2004). The goal of this section is to bridge the gap between computationally intensive RHA and efficiency-demanding design practice

based on a comparison of results for low-rise braced frames with short fundamental periods. Results in terms of maximum interstory drift ratios (IDRs) are compared, and the method to estimate interstory drift demands is suggested based on these analyses.

The model building (DASSE, 2007) developed to investigate the SCBF systems is a rectangular structure with four perimeter braced frame subassemblies. Braces are arranged as a double story X-type. The building was designed in conformance with the provisions of 2006 IBC, ASCE 7-05, and AISC 341-05. A typical building floor plan and frame elevation are shown in Figure 6.29. A finite element model was developed for the braced frame subassembly, using shell elements and the cyclic damage plasticity model. The finite element model is shown in Figure 6.30.

First, the model building was subjected to the sixty ground motions that were assembled for the SAC project (Somerville *et al.,* 1997), representing seismic events ranging from the frequently occurring to those that are very rare, and was evaluated using RHA procedure. In all sixty analyses, the maximum interstory drift occurs in the first story, thus, hereinafter maximum interstory drift ratios refer to those ratios in the first story. In the RHA, a standard Newmark integrator is adopted. Discussion on instability of Newmark integrator can be found in Appendix B.

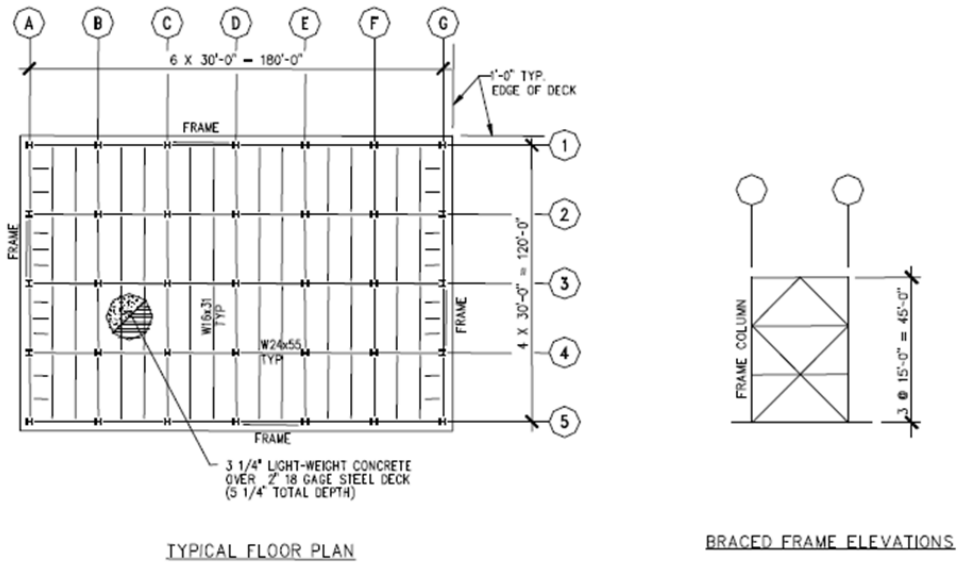

Figure 6.29: Model building floor plan and braced frame elevations

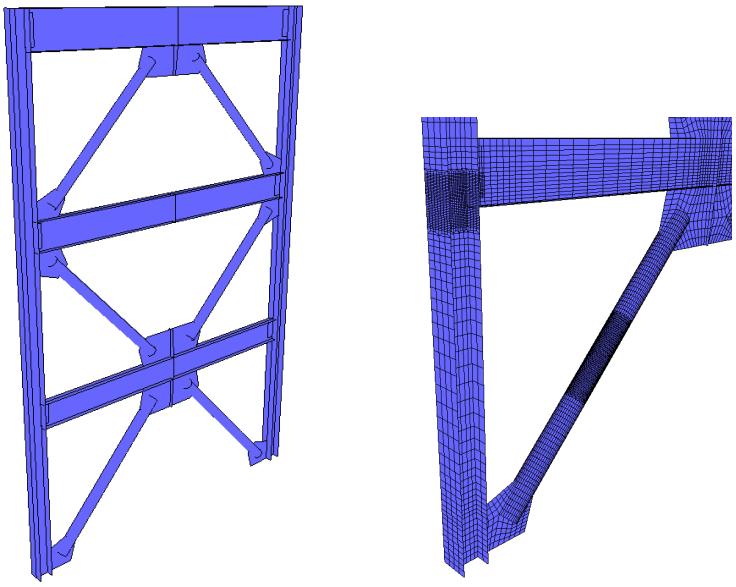

Figure 6.30: Finite element model and refined regions of the building

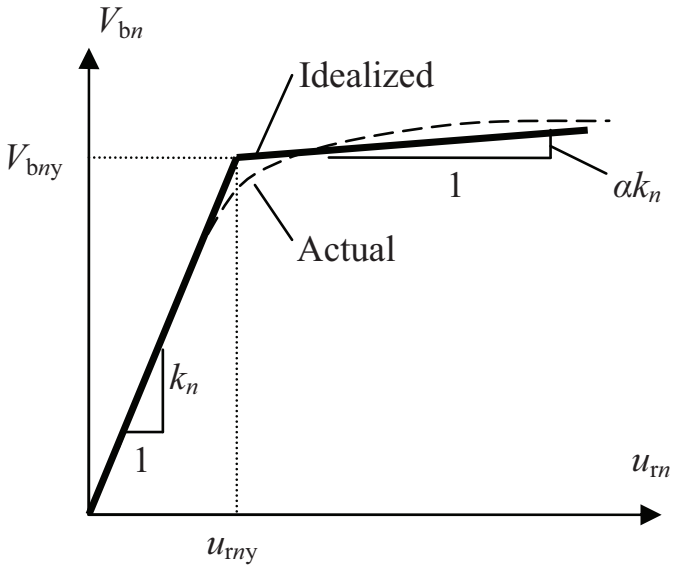

(a) An nth-mode pushover curve and its idealization

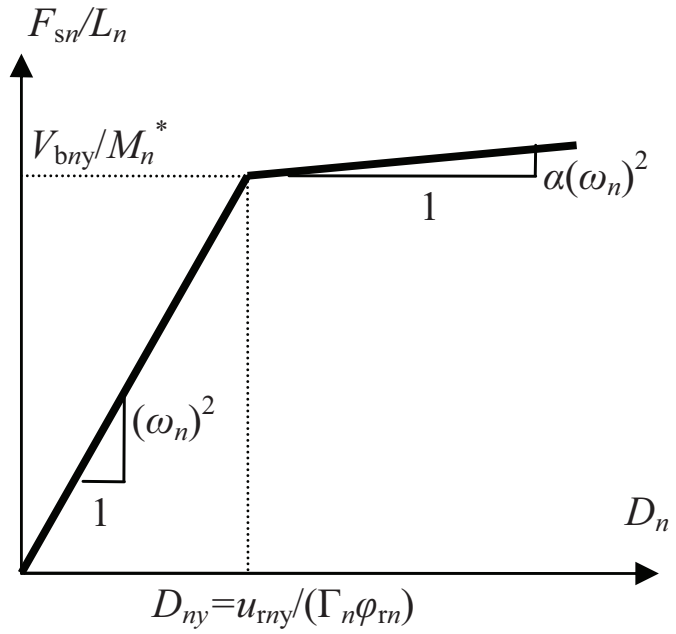

(b) Force-deformation curve for nth-mode SDF system

Figure 6.31: Conversion to nth-mode SDF system

Then the model building was evaluated using MPA:

1. The natural frequencies ω_i, and modes $\boldsymbol{\phi}_i$, were computed with modal analysis.

2. For the nth mode, the base-shear-roof displacement, V_{bn}-u_{rn}, pushover curve by nonlinear static analysis of the building using lateral force distributions $\boldsymbol{s} = \boldsymbol{m}\boldsymbol{\phi}_n$ was developed. The structural deformation history is saved. A new pushover method using constraints (Appendix A) is adopted in this research.

3. The V_{bn}-u_{rn} pushover curve was converted to the force-deformation, F_{sn}/L_n-D_n, relation for the nth-mode equivalent inelastic single-degree-of-freedom system with unit mass. This step is illustrated in Figure 6.31, where M_n^* is the nth-mode effective modal mass.

4. The force-deformation hysteresis relation for the nth-mode single-degree-of-freedom system was idealized. In this analysis, a peak-oriented stiffness deteriorating hysteresis type was chosen based on comparison of monotonic and cyclic pushover curves for Mode 1, shown in Figure 6.32.

5. The peak deformation D_n of the nth-model inelastic single-degree-of-freedom system defined by the hysteretic force-deformation relation developed in Step 4 with response history analysis was computed.

6. The peak roof displacement u_{rn} associated with the nth-mode inelastic system from $u_{rn} = \Gamma_n \phi_{rn} D_n$ was computed.

7. From the structural deformation history obtained in Step 2, the story displacements vector at roof displacement equal to u_{rn} was extracted.

8. Steps 3 to 7 were repeated for all modes to be included.

9. The total responses by combining the peak modal responses using an appropriate model combination rule was determined. The SRSS rule was used in this paper. Some modal properties are listed in Table 6.3.

In Step 5, the behavior of second and third mode inelastic single-degree-of-freedom system was essentially elastic because of their relative high yield forces compared to the first mode (Table 6.3).

n	T_n (s)	$\boldsymbol{\phi}_n$	Γ_n	V_{bn}/M_n^* (in/sec^2)
1	0.521	$[0.32, 0.71, 1.00]^T$	1.26	200
2	0.204	$[1.00, 0.95, -1.00]^T$	0.33	1300
3	0.146	$[1.00, -0.80, 0.25]^T$	0.26	4000

Table 6.3: Elastic modal properties of the 3-story SCBF subassembly

Maximum interstory drifts (in Story 1) from elastic spectral analysis and RHA are compared in Figure 6.33. Estimates of interstory drift based on elastic spectra substantially diverge from nonlinear RHA results for intense ground motions. This is similar to observation reported by Chen *et al.* (2008). Maximum interstory drifts (in Story 1) from MPA and RHA are then compared in Figure 6.34. In contrast to estimates using elastic spectra, good agreement is observed between predictions using MPA as proposed above (with inelastic spectra) and simulations using RHA,

for MPA of both the first mode and the first three modes. Results of MPA for the first three modes are slightly better than those of MPA of the first mode in terms of the coefficient of determination R^2 (0.9568 versus 0.9651). The reason why the improvement is small is again because of the elastic behavior of second and third modal single-degree-of-freedom system, as well as smaller modal contribution factors for higher modes. Thus, the dominant interstory drift response is that for the first mode.

As demonstrate above, for low-rise braced frames with short fundamental periods that do not fall into the Newmark and Hall displacement-preserved range, the MPA procedure estimates interstory drift with reasonable accuracy.

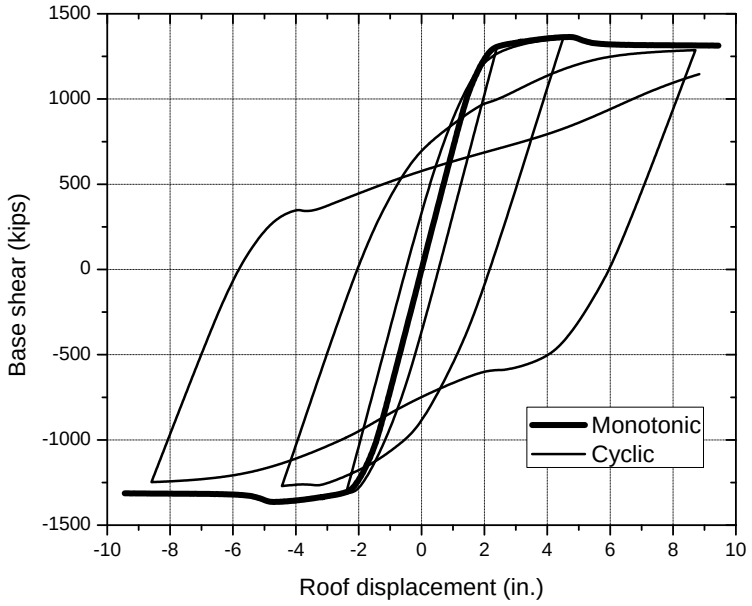

Figure 6.32: Monotonic and cyclic pushover curves for Mode 1

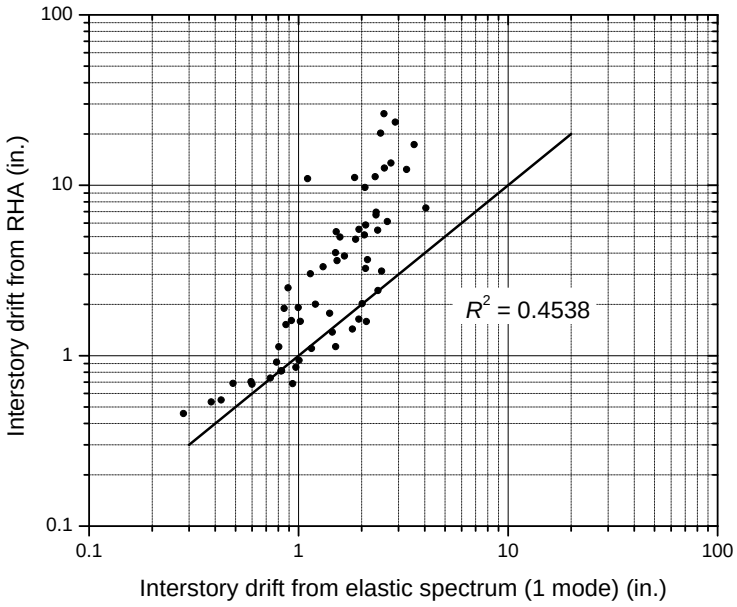

(a) Elastic spectrum of 1 mode

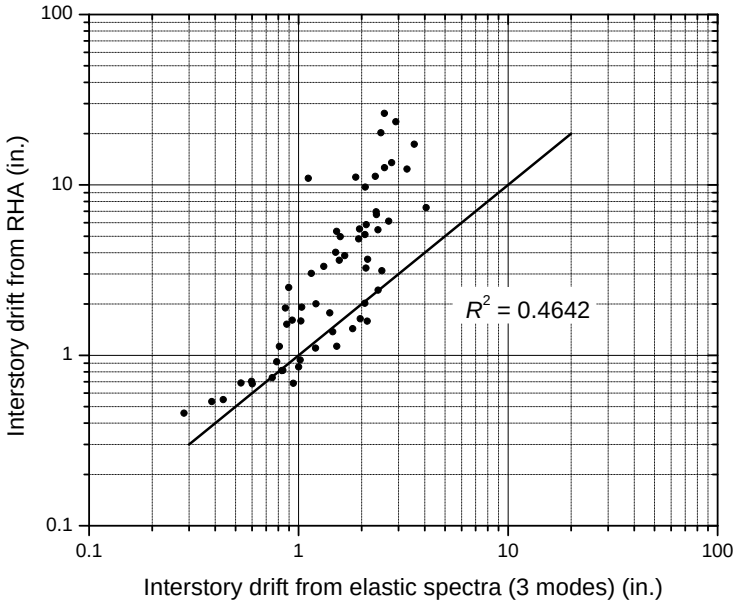

(b) Elastic spectra of 3 modes

Figure 6.33: Interstory drifts by elastic spectral and response history analysis

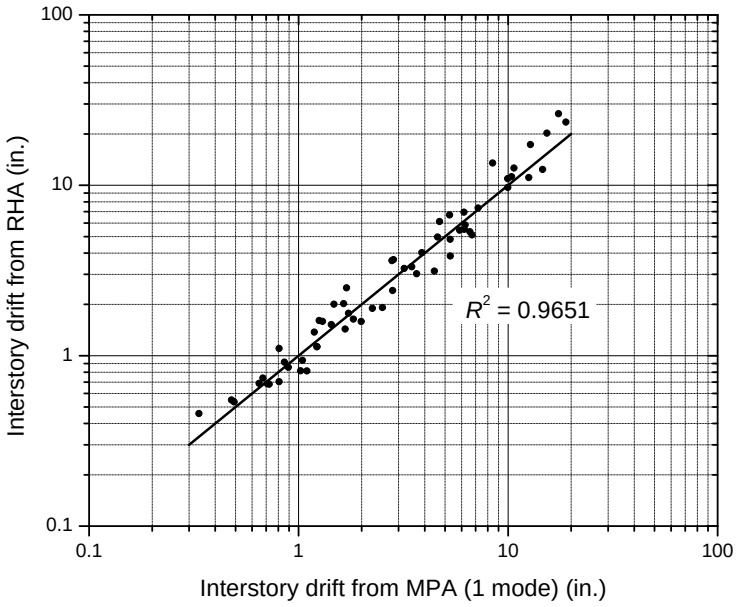

(a) MPA of 1 mode

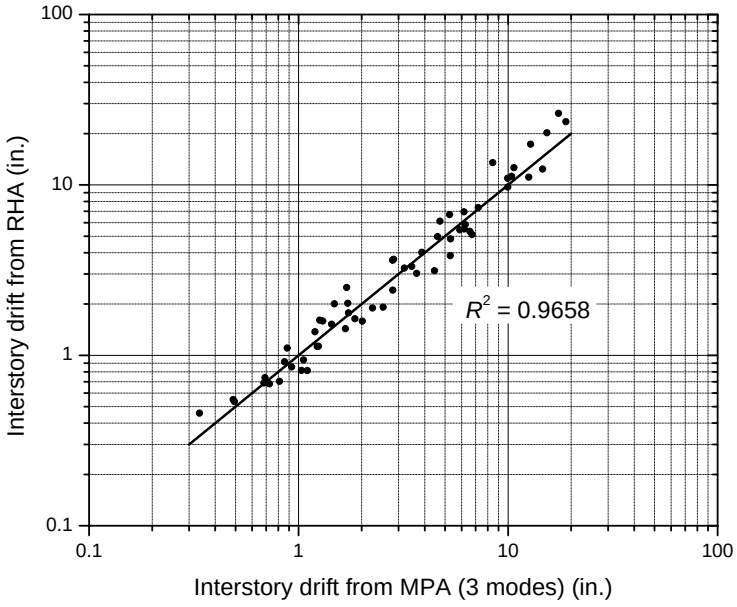

(b) MPA of 3 modes

Figure 6.34: Interstory drifts by modal pushover and response history analysis

6.5 Concluding remarks

A series of analyses are presented that evaluate and refine several requirements for detailing and analyzing special concentrically braced steel frame buildings. Numerical simulations demonstrate that the fatigue life capacity of braces is heavily dependent on width-thickness ratios and deformation histories. Recommendations are presented for developing fatigue life demand or loading protocols for use in numerical and experimental investigations. Improved beam-column connection details are recommended to reduce the damage accumulation. More appropriate lateral bracing positions for beams in V-type and inverted V-type braced frames are suggested and evaluated. An method to estimate interstory drift demands for low-rise braced frame is suggested based on the Modal Pushover Analysis procedure.

Chapter 7

Conclusions

This research focuses on simulations of the inelastic seismic behavior of steel braced frames including the effects of low-cycle fatigue. Numerical models that assess the initiation and propagation of failure during cyclic loading need to account for multi-axial states of material nonlinearity, local and global buckling, and the inability of the material to deform inelastically because of low-cycle fatigue. This study simulates failures caused by low-cycle fatigue using finite element models. Compared to phenomenological models, finite element models require more computational effort, but incorporate more realistic physical representations of members and materials, including the initiation and evolution of damage through complete failure. In addition to examining the inelastic behavior and failure of traditional steel beam-to-column connections, members and connections in concentrically braced frames were investigated to better understand the influence of global and local buckling on member

deterioration and failure.

Following a review of existing material models for simulating structural steel deterioration, a series of investigations are conducted using finite element modeling techniques. Finite element methods can directly account for complex states of stress and changes in deformed shape. And material models are critical for constitutive behavior at integration points of the finite element models. However, available material models tend to emphasize behavior associated with ideal ductile response or with failure occurring under monotonic loading conditions (*e.g.,* during metal-forming processes or vehicle collision). These models are not suitable for progressive collapse analysis under cyclic loading where the consequence of this adverse behavior on the subsequent response or integrity of the structure is of interest.

Therefore, a new, numerically efficient continuum damage mechanics material model capable of simulating inelastic behavior and deterioration of mechanical properties because of low-cycle fatigue has been devised and implemented in a finite element software LS-DYNA (LSTC 2007). Computational results obtained with this new material model correlate well with test results for several beam-to-column connections, individual braces, and braced frame subassemblies. These applications of the finite element model to realistic cases involving progressive collapse illustrate the importance of material deterioration and rupture. Unfortunately, the ability of the material model to predict ultimate behavior depends heavily on the material modeling properties specified. Recommendations for characterizing material properties for

these types of analysis are developed and presented.

A series of analyses are presented that evaluate and refine several requirements for detailing and analyzing special concentrically braced steel frame buildings, demonstrating that the fatigue life capacity of braces is heavily dependent on width-thickness ratios and deformation histories. Member slenderness ratios are shown to have negligible effect on fatigue life capacity. Therefore, recommendations are presented for developing fatigue life demand or loading protocols for use in numerical and experimental investigations. Next, damage evolution in gusseted beam-to-column connections is evaluated and compared for different connection details, and improved connection details are recommended to reduce the damage accumulation. The position of lateral bracing members for beams in V-type and inverted V-type braced frames are also examined. More appropriate positions and methods to compensate for problems detected for currently recommended lateral bracing member positions are suggested and evaluated. Finally, for low-rise braced frames that respond inelastically during strong earthquake ground shaking, an alterative method to estimate interstory drift demands is suggested based on the Modal Pushover Analysis procedure.

Additional research work is needed to develop improved guidelines for modeling. These depend on having high-quality data on the cyclic hysteretic properties of the materials being analyzed and on their low-cycle fatigue characteristics. In addition, more experience with the new continuum damage mechanics model is required, including analysis of systems with high axial loads in members, considering a wider

range of behavior. For such elements to become more useful and reliable, it is essential to obtain additional high-quality data for evaluation and calibration. When such models can be implemented with confidence, they can be used to improve structural details, assess the behavior of structures subjected to unusual loading, and provide a mechanism for calibrating simpler numerical (phenomenological or physical theory) models that can be applied to large structures where computational costs prohibit the use of finite element models.

Bibliography

[1] American Institute of Steel Construction, Inc. (AISC) (2005a). *Steel Construction Manual,* AISC, Chicago, IL.

[2] American Institute of Steel Construction, Inc. (AISC) (2005b). *Seismic Provisions for Structural Steel Buildings, ANSI/AISC 341-05,* AISC, Chicago, IL.

[3] American Institute of Steel Construction, Inc. (AISC) (2006). *Seismic Design Manual,* American Institute of Steel Construction, Inc. and Structural Steel Educational Council, Chicago, IL.

[4] Anderson, T. L. (1995). *Fracture Mechanics, Fundamentals and Applications,* Second Edition, CRC Press.

[5] Armstrong, P. J., and Frederick, C. O. (1966). "A Mathematical Representation of the Multiaxial Bauschinger Effect." *CEGB Report RD/B/NN/731,* Berkeley Laboratories, R&D Department, CA.

[6] Besson, J., and Guillemer-Neel, C. (2003). "An Extension of the Green and Gurson Models to Kinematic Hardening." *Mechanics of Materials,* 35, 1–18.

[7] Bridgman, P. W. (1952). *Large Plastic Flow and Fracture,* McGraw-Hill.

[8] Bruneau, M., Uang, C. M., and Whittaker, A. (1998). *Ductile Design of Steel Structures,* McGraw Hill.

[9] Cedergren, J., Melin, S., and Lidstroḿ, P. (2004). "Numerical Modelling of P/M Steel Bars Subjected to Fatigue Loading using an Extended Gurson Model." *European Journal of Mechanics — A/Solids,* 23, 899–908.

[10] Chaboche, J.-L. (1986). "Time-Independent Constitutive Theories for Cyclic Plasticity." *International Journal of Plasticity,* 2(2), 149–188.

[11] Chaboche, J.-L. (1989). "Constitutive Equations for Cyclic Plasticity and Cyclic Visco-Plasticity." *International Journal of Plasticity,* 5(3), 247–302.

[12] Chambers, J. J., and Ernst, C. J. (2005). "Brace Frame Gusset Plate Research: Phase I Literature Review." American Institute of Steel Construction.

[13] Chen, C.-H., Lai, J.-W., and Mahin, S. A. (2008). "Numerical Modeling and Performance Assessment of Concentrically Braced Steel Frames." *Proceedings of the 2008 Structures Congress,* April 24–26, 2008, Vancouver, BC, Canada.

[14] Chintanapakdee, C., and Chopra, A. K. (2003). "Evaluation of Modal Pushover

Analysis using Generic Frames." *Earthquake Engineering and Structural Dynamics,* 32, 417–442.

[15] Chintanapakdee, C., and Chopra, A. K. (2004). "Seismic Response of Vertically Irregular Frames: Response History and Modal Pushover Analyses." *Journal of Structural Engineering,* ASCE, 130(8), 1177–1185.

[16] Chopra, A. K., and Goel, R. K. (2002). "A Modal Pushover Analysis Procedure for Estimating Seismic Demands for Buildings." *Earthquake Engineering and Structural Dynamics,* 31, 561–582.

[17] Clarke, M. J., and Hancock, G. J. (1990). "A Study of Incremental-Iterative Strategies for Non-linear Analyses." *International Journal for Numerical Methods in Engineering,* 29, 1365–1391.

[18] Coffin, L. F. (1954). "A Study of the Effects of Cyclic Thermal Stresses on a Ductile Metal." *Transations,* ASME, 76, 931–950.

[19] Crisfield, M. A. (1981). "A Fast Incremental/Iteration Solution Procedure that Handles 'Snap-Through'." *Computers and Structures,* 13, 55–62.

[20] DASSE (2007). "Cost Advantages of Buckling Restrained Braced Frame Buildings." DASSE Design Inc, private communication.

[21] Dufailly, J., and Lemaitre, J. (1995). "Modeling Very Low Cycle Fatigue." *International Journal of Damage Mechanics,* 4, 153–170.

[22] Elchalakani, M., Zhao, X.-L., and Grzebieta, R. (2003). "Tests on Cold-Formed Circular Tubular Braces under Cyclic Axial Loading." *Journal of Structural Engineering,* ASCE, 129(4), 507–514.

[23] Englemann, B. E., Whirley, R. G., and Goudreau, G. L. (1989). "A Simple Shell Element Formulation for Large-Scale Elastoplastic Analysis." *Analytical and Computational Models of Shells,* ASME, New York.

[24] Fell, B. V., Kanvinde, A. M., Deierlein, G. G., Myers, A. M., and Fu, X. (2006). "Buckling and fracture of concentric braces under inelastic cyclic loading." SteelTIPS, Technical Information and Product Service, Structural Steel Educational Council, Moraga, CA.

[25] Fell, B. V. (2008). "Large-Scale Testing and Simulation of Earthquake-Induced Ultra Low Cycle Fatigue in Bracing Members Subjected to Cyclic Inelastic Buckling." Doctoral Dissertation, University of California at Davis.

[26] Foutch, D. A., Goel, S. C., and Roeder, C. W. (1986). "Seismic Testing of Full-Scale Steel Building — Part I." *Journal of the Structural Division,* ASCE, 113, 2111–2129.

[27] Fujimoto, M., Hashimoto, A., Nakagomi, T., and Yamada, T. (1985). "Study on Fracture of Welded Connections in Steel Structures under Cyclic Loads Based on Nonlinear Fracture Mechanics." *Journal of Structural and Construction Engineering,* Transactions of AIJ, 356, 93–102.

[28] Galambos, T. V. (1998). *Guide to Stability Design Criteria for Metal Structures,* Fifth Edition, John Wiley and Sons, Inc.

[29] Goggins, J. M., Broderick, B. M., Elghazouli, A. Y., and Lucas, A. S. (2005). "Experimental Cyclic Response of Cold-Formed Hollow Steel Bracing Members." *Engineering Structures,* 27(7), 977–989.

[30] Gurson, A. L. (1977). "Continuum Theory of Ductile Rupture by Void Nucleation and Growth: Part I — Yield Criteria and Flow Rules for Porous Ductile Media." *Journal of Engineering Materials and Technology,* ASME, 99, 2–15.

[31] Goel, S. C. (1992). "Cyclic Post Buckling Behavior of Steel Bracing Members." *Stability and Ductility of Steel Structures under Cyclic Loading, 75–104,* CRC Press, Boca Raton, FL.

[32] Goel, R. K., and Chopra, A. K. (2004). "Evaluation of Modal and FEMA Pushover Analyses: SAC Buildings." *Earthquake Spectra,* 20, 225–254.

[33] Han, S.-W., Kim, W. T., and Foutch, D. A. (2007). "Seismic Behavior of HSS Bracing Members According to Width-Thickness Ratio under Symmetric Cyclic Loading." *Journal of Structural Engineering,* ASCE, 133 (2), 264–273.

[34] Harris, H. G., and Muskivitch, J. C. (1980). "Models of Precast Concrete Large Panel Buildings." *Journal of the Structural Division,* ASCE, 106, 545–565.

[35] Harris, H. G., and Sabnis, G. M. (1990). *Structural Modeling and Experimental Techniques,* CRC Press LLC.

[36] Hassan, O., and Goel, S. C. (1991). "Seismic Behavior and Design of Concentrically Braced Steel Structures." *Report UMCE 91-1*, University of Michigan, Department of Civil and Environmental Engineering, Ann Arbor, MI.

[37] Hughes, T. J. R. (1987). *Finite Element Method, Linear Static and Dynamic Finite Element Analysis,* Prentice-Hall, Englewood Cliffs.

[38] Ikeda, K., Mahin, S. A., and Dermitzakis, S. N. (1984). "Phenomenological Modeling of Steel Braces under Cyclic Loading." *UCB/EERC-84/09,* Earthquake Engineering Research Center, Berkeley, CA.

[39] Ikeda, K., and Mahin S. A. (1984). "A Refined Physical Theory Model for Predicting the Seismic Behavior of Braced Steel Frames." *Report UCB/EERC-84/12,* Earthquake Engineering Research Center, Berkeley, CA.

[40] Iserles, A. (1996). *A First Course in the Numerical Analysis of Differential Equations,* Cambridge University Press, New York.

[41] Jain, A. K., and Goel, S. (1978). "Hysteresis Models for Steel Members Subjected to Cyclic Buckling or Cyclic End Moments and Buckling — Users Guide for DRAIN-2D: EL9 AND EL10." *Report UMEE 78-6,* University of Michigan, College of Engineering, Ann Arbor, MI.

[42] Kachanov, L. M. (1958). "Time of Rupture Process under Creep Conditions." *Ievestiva Akademii Navk SSSR Odtelemie Tekhniheskikh Nauk*, 8, 26–31.

[43] Kanvinde, A., and Deierlein, G. G. (2004). "Micromechanical Simulation of Earthquake Induced Fractures in Steel Structures." *Blume Earthquake Engineering Center Report No. 145,* Stanford University, Stanford, CA.

[44] Kishiki, S., Yamada, S., and Wada, A. (2008). "Experimental Evaluation of Structural Behavior of Gusset Plate Connection in BRB Frame System." *Proceedings of 14th World Conference on Earthquake Engineering,* October 12–17, 2008, Beijing, China.

[45] Krawinkler, H., Gupta, A., Medina, R., and Luco, N. (2000a). "Development of Loading Histories for Testing of Steel Beam-to-Column Assemblies." *SAC Background Report SAC/BD-00/10.*

[46] Krawinkler, H., Parisi, F., Ibarra, L., Ayoub, A., and Medina, R. (2000b). "Development of a Testing Protocol for Woodframe Structures." *CUREE Publication No. W-02.*

[47] Leblond, J.-B., Perrin, G., and Devaux, J. (1995). "An Improved Gurson-type Model for Hardenable Ductile Metals." *European Journal of Mechanics — A/Solids,* 14, 499–527.

[48] Lee, K., and Bruneau, M. (2005). "Energy Dissipation of Compression Members

in Concentrically Braced Frames: Review of Experimental Data." *Journal of Structural Engineering,* ASCE, 131(4), 552–559.

[49] Lee, S., and Goel, S. C. (1987). "Investigation of Concrete-Filled Steel Tubular Cyclic Bending Buckling Members." *Report UMCE 87-3,* University of Michigan, Department of Civil and Environmental Engineering, Ann Arbor, MI.

[50] Lehman, D. E., Roeder, C. W., Herman, D., Johnson, S., and Kotulka, B. (2008). "Improved Seismic Performance of Gusset Plate Connections." *Journal of Structural Engineering,* ASCE, 134(6), 890–901.

[51] Lemaitre, J. (1971). "Evaluation of Dissipation and Damage in Metals Submitted to Dynamic Loading." *Mechanical Behavior of Materials: Proceedings of 1st International Conference,* August 5–20, 1971, Kyoto, Japan, 540–549.

[52] Lemaitre, J. (1992). *A Course on Damage Mechanics,* Springer-Verlag.

[53] Lemaitre, J., and Chaboche, J.-L. (1990). *Mechanics of Solid Materials,* Cambridge University Press.

[54] Lignos, D., and Krawinkler, H. (2007). "Contributions to Collapse Prediction of Frame Structures." Kajima-CUREE Joint Research Program, Phase VI: Investigation of Factors Leading to Progressive Collapse of Structures, Category II: Analysis of Structural Component Failure.

[55] Liu, Z., and Goel, S. C. (1987). "Seismic Behavior of Hollow and Concrete-Filled Tabular Bracing Members." *Report UMCE 87-11,* University of Michigan, Department of Civil and Environmental Engineering, Ann Arbor, MI.

[56] LSTC (2007). *LS-DYNA Keyword User's Manual,* Livermore Software Technology Corporation, CA, US.

[57] Manson, S. S. (1953). "Behavior of Materials Under conditions of Thermal Stress." *Heat Transfer Symposium,* University of Michigan Engineering Research Institute, 9–75.

[58] Manson, S. S., Halford, G. R., and Hirschberg, M. H. (1971). "Creep Fatigue Analysis by Strain Range Partitioning." *Symposium on Design for Elevated Temperature Environment,* ASME, NASA, TMX.

[59] Marini, B., Mudry, F., and Pineau, A. (1985). "Ductile Rupture of A508 Steel under Nonradial Loading." *Engineering Fracture Mechanics,* 22(3), 375–386.

[60] Markarian, A., and Mahin, S. (2004). "Tests of a Gusset Plate Connection for Concentric Braced Frames." EERI Student Paper.

[61] Matsuishi M, and Endo T. (1968). "Fatigue of Metals Subjected to Varying Stresses." Paper Presented to Japan Society of Mechanical Engineers.

[62] McClintock, F. A. (1968). "A Criterion for Ductile Fracture by the Growth of Holes." *Journal of Applied Mechanics,* 35, 363–371.

[63] Midorikawa, M., Nishiyama, I., and Yamanouchi, H. (1988). "Static and Dynamic Analysis of Full-Scale Concentrically K-Braced Steel Building." *Proceedings of 9th World Conference on Earthquake Engineering,* Tokyo, Japan, 255–260.

[64] Mindlin, R. D. (1951). "Influence of Rotary Inertia and Shear on Flexural Motions of Isotropic Elastic Plates." *Journal of Applied Mechanics,* 18, 31–38.

[65] Miner, M. A. (1945). "Cumulative Damage in Fatigue." *Journal of Applied Mechanics,* ASME, 67, A159–A164.

[66] Morrow, J. D. (1964). "Cyclic Plastic Strain Energy and Fatigue of Metals." *Symposium,* ASTM, Chicago.

[67] Newmark, N. M. (1959). "A Method of Computation for Structural Dynamics." *Journal of the Engineering Mechanics Division,* ASCE, 85, 67–94.

[68] Newmark, N. M., and Hall, W. J. (1982). *Earthquake Spectra and Design,* EERI Monograph Series, Earthquake Engineering Research Institute, Oakland, CA.

[69] Nishimura, N., Ono, K., Ikeuchi, T., and Shinke, T. (1994). "Experimental Investigation on Hysteretic Behavior of Structural Steels in Plastic Range." *Steel Construction Engineering,* 1, 173–182.

[70] Okamoto, S., Nakata, S., Kitagawa, Y., Yoshimura M., and Kaminosono T. (1982). "A Progress Report on the Full-scale Seismic Experiment of a Seven-

story Reinforced Concrete Building — Part of the U.S.-Japan Cooperative Program." *BRI Research Paper No. 94,* Building Research Institute, Ministry of Construction, Japan.

[71] Palmgren, A. (1924). "Die Lebensdauer von Kugellagern." *Zeitschrift des Vereines Deutscher Ingenieure,* 68(14), 339–341.

[72] Pian, T. H. H., and Sumihara, K. (1985). "Rational Approach for Assumed Stress Elements." *International Journal for Numerical Methods in Engineering,* 20, 1685–1695.

[73] Pirondi, A., and Bonora, N. (2003). "Modeling Ductile Damage under Fully Reversed Cycling." *Computational Materials Science,* 26, 129–141.

[74] Powell, J., Clark, K., Lehman, D. E., and Roeder, C. W. (2008). "Test of a Full Scale Concentrically Braced Frame with Multi-Story X-Bracing." *Proceedings of the 2008 Structures Congress,* April 24–26, 2008, Vancouver, BC, Canada.

[75] Prager, W. (1956). "A New Method of Analyzing Stress and Strains in Work-Hardening Plastic Solids." *Journal of Applied Mechanics,* 23, 493–496.

[76] Puttick, K. E. (1959). "Ductile Fracture in Metals." *Philosophical Magazine,* 4, 964–969.

[77] Ramm, E. (1981). "Strategies for Tracing the Nonlinear Response near Limit

Points." *Nonlinear Finite Element Analysis in Structural Mechanics,* Edited by E. Wunderlich, E. Stein, and K. J. Bathe, Springer-Verlag, Berlin.

[78] Rice, J. R., and Tracey, D. M. (1969). "On the Ductile Enlargement of Voids in Triaxial Stress Fields." *Journal of the Mechanics and Physics of Solids,* 17, 201–217.

[79] Roeder, C. W., Lehman, D. E., Johnson, S., Herman D., and Yoo J. H. (2006). "Seismic Performance of SCBF Braced Frame Gusset Plate Connections." *Proceedings of 4th International Conference on Earthquake Engineering,* October 12–13, 2006, Taipei, Taiwan.

[80] Rousselier, G. (1987). "Ductile Fracture Models and Their Potential in Local Approach of Fracture." *Nuclear Engineering and Design,* 105, 97–111.

[81] Somerville, P. G., Smith, N. F., Punyamurthula, S., and Sun, J. (1997). "Development of Ground Motion Time Histories for Phase 2 of the FEMA/SAC Steel Project." *SAC Background Report SAC BD/97-04,* SAC Steel Joint Venture, Sacramento, California.

[82] Simo, J. C., and Hughes, T. J. R. (1986). "On the Variational Foundations of Assumed Strain methods." *Journal of Applied Mechanics,* 53, 1685–1695.

[83] Simo, J. C., and Hughes, T. J. R. (1998). *Computational Inelasticity,* Springer-Verlag.

[84] Sivaselvan, M., Lavan, O., Dargush, G., Oren, L., and Reinhorn, A. (2007). "Toward Analysis of Full System Failure of Structures." Kajima-CUREE Joint Research Program, Phase VI: Investigation of Factors Leading to Progressive Collapse of Structures, Category I: Evaluation and Development of Analytical Tools.

[85] Steglich, D., Pirondi, A., Bonora, N., and Brocks, W. (2005). "Micromechanical Modelling of Cyclic Plasticity Incorporating Damage." *International Journal of Solids and Structures,* 42, 337–351.

[86] Suita, K., Nakashima M., and Engelhardt M. D. (2000). "Comparison of Seismic Capacity between Post-Northridge and Post-Kobe Beam-to-Column Connections." *Behaviour of Steel Structures in Seismic Areas: Proceedings of 3rd International Conference,* August 21–24, 2000, Montreal, Canada, 527–534.

[87] Tanaka, N., Sawamoto, Y., and Saeki, T. (2000). "Elasto-Plastic Behavior of Beam-Column Connections." *Proceedings of 12th World Conference on Earthquake Engineering,* New Zealand.

[88] Tang, X., and Goel, S. C. (1987). "Seismic Analysis and Design Considerations of Braced Steel Structures." *Report UMCE 87-4,* University of Michigan, Department of Civil and Environmental Engineering, Ann Arbor, MI.

[89] Tang, X., and Goel, S. C. (1989). "Brace Fractures and Analysis of Phase I Structure." *Journal of Structural Engineering,* ASCE, 115(8), 1960–1976.

[90] Thomason, P. F. (1990). *Ductile Fracture of Metals,* Pergamon Press.

[91] Thornton, W. A. (1991). "On the Analysis and Design of Bracing Connections." Proceedings of National Steel Contruction Conference, AISC, Chicago, IL, 26.1–26.33.

[92] Tremblay, R. (2000). "Influence of Brace Slenderness on the Seismic Response of Concentrically Braced Steel Frames." *Behaviour of Steel Structures in Seismic Areas: Proceedings of 3rd International Conference,* August 21–24, 2000, Montreal, Canada, 527–534.

[93] Tremblay, R. (2002). "Inelastic Seismic Response of Steel Bracing Members." *Journal of Constructional Steel Research,* 58, 665–701.

[94] Tremblay, R., and Bouatay, N. (2002). "Loading Protocols for the Seismic Testing of Ductile Bracing Members in Concentrically Braced Steel Frames." *Proceeding of 12th European Conference on Earthquake Engineering,* London, UK, Paper No. 480.

[95] Tremblay, R., Archambault, M. H., and Filiatrault, A. (2003). "Seismic Performance of Concentrically Braced Steel Frames made with Rectangular Hollow Bracing Members." *Journal of Structural Engineering,* ASCE, 129(12), 1626–1636.

[96] Tremblay, R., Haddad, M., Martinez, G., Richard, J., and Moffatt, K. (2008).

"Inelastic Cyclic Testing of Large Size Steel Bracing Members." *Proceedings of 14th World Conference on Earthquake Engineering,* October 12–17, 2008, Beijing, China.

[97] Tsai, K. C., Hsiao, P. C., Chen, C. H., Lai, J. W., Lin, M. L., and Weng, Y. T. (2004). "Pseudo Dynamic Tests of a Full Scale CFT/BRB Composite Frame.", *Proceedings of the 2004 Structures Congress,* May 22–26, 2004, Nashville, TN.

[98] Tsai, K. C., Weng, Y. T., Wang, K. J., Tsai, C. Y., and Lai, J. W. (2006). "Bi-Directional Sub-Structural Pseudo-Dynamic Tests of a Full-Scale 2-Story BRBF, Part I: Seismic Design, Analytical and Experimental Performance Assessments." *Proceedings of 8th U.S. National Conference on Earthquake Engineering,* EERI, April 18–22, 2006, San Francisco, CA.

[99] Tvergaard, V., and Needleman, A. (1984). "Analysis of the Cup-Cone Fracture in a Round Tensile Bar." *Acta Metallurgica,* 32(1), 157–169.

[100] Tvernelli, J. F., and Coffin, L. F. (1959). "A Compilation and Interpretation of Cyclic Strain Fatigue Tests on Metals." *Transations*, ASM, 51, 438–453.

[101] Uriz, P. (2005). "Towards Earthquake Resistant Design of Concentrically Braced Steel Structures." Doctoral Dissertation, University of California at Berkeley.

[102] Whitmore, R. E. (1952). "Experimental Investigation of Stresses in Gusset

Plates." *Bulletin No. 16,* Civil Engineering, The University of Tennessee Engineering Experiment Station, Knoxville, TN.

[103] Whittaker, A. S., Uang, C. M., and Bertero, V. V. (1989). "Experimental Behavior of a Dual Steel System." *Journal of the Structural Division,* ASCE, 115.

[104] Xia, L., and Shih, C. F. (1995). "Ductile Crack Growth — I. A Numerical Study Using Computational Cells with Microstructurally-Based Length Scales." *Journal of the Mechanics and Physics of Solids,* 43(2), 233–259.

[105] Yang, F., and Mahin, S. (2005). "Limiting Net Section Fracture in Slotted Tube Braces." Steel Tips, Structural Steel Education Council, Orinda, CA.

[106] Ziegler, H. (1959). "A Modification of Prager's Hardening rule." *Quarterly of Applied Mechanics,* 17, 55–65.

Appendix A

Applying Proportional Loads using Constraints

A.1 Introduction

Several structural analyses require a fixed load pattern, with all load magnitudes varying with a single scalar parameter. This is known as "proportional loading". One example of a analysis that requires proportional loading is a pushover analysis in which loads are applied at some or all stories. Another example is multiaxial compression — or tension — of concrete specimens in which two or three surface loads are applied.

One source of difficulty in performing such analysis is that part of structure,

or the whole structure, may undergo softening because of mechanical deterioration and/or large deformations. For such conditions, the load factor must decrease to maintain equilibrium as the structure softens. To conduct these types of analyses, a sophisticated load-adjusting scheme is necessary with an accompanying solution procedure.

Several such schemes have been proposed, including the well known arc-length method (Crisfield, 1981; Ramm, 1981). A comprehensive discussion of load-adjusting schemes can be found in Clarke and Hancock (1990).

Load-adjusting schemes are useful for solving an equilibrium state with global instability, which manifests itself in a global load-displacement response that has a negative tangent stiffness and a smooth equilibrium path in load-displacement space. However, typical global load-adjusting schemes may not work if the instability is localized because of a severe local nonlinearity and the equilibrium path is no longer smooth. An example of an analysis that may address the limitation of such a load-adjusting scheme would be an analysis of a reinforced concrete structure, where tensile cracks of the concrete result in randomly distributed local instabilities.

When an external load is applied at only one degree-of-freedom of a structure, it is convenient to prescribe incremental displacement at this degree-of-freedom — making the structural response stable — thereby making it easier to evaluate the load-displacement behavior of the structure. However, if loads

are to be applied at multiple degrees-of-freedom, prescribing displacements at all these degrees-of-freedom is not applicable for proportional loads; *a priori* displacements needed to maintain the proportional load pattern are unknown for a nonlinear structure.

For laboratory experiments, several well-developed methods for applying proportional loads exist. Inspired by these laboratory methods, a new numerical method is developed for application of proportional loads. The degrees-of-freedom corresponding to the prescribed proportional loads are called "target degrees-of-freedom". In the proposed method, an additional control degree-of-freedom is introduced, and a multiple point constraint (MPC) involving the control degree-of-freedom and the target degrees-of-freedom is formulated. By prescribing the displacement of the control degree-of-freedom, proportional loads can be applied at target degrees-of-freedom without applying a load-adjusting scheme.

A.2 Experiments with proportional loading

One method used by laboratories to apply proportional loads is through multiple actuators. Displacement of one actuator is prescribed and the resistance of this actuator is measured. The loads to be applied at other degrees-of-freedom are calculated using predefined load proportionality, and then these forces are

applied by other actuators to maintain the prescribed load distribution. This method of laboratory testing is described by Okamoto *et al.* (1982). However, this method is not suitable for numerical analysis because it needs feedback control, which does not fit into the standard numerical analysis procedure.

Another method is the Whiffle-Tree load system (Harris and Muskivitch, 1980; Harris and Sabnis, 1999). This mechanical system involves an articulated set of load distribution bars and one actuator to apply a single concentrated load (Figure A.1).

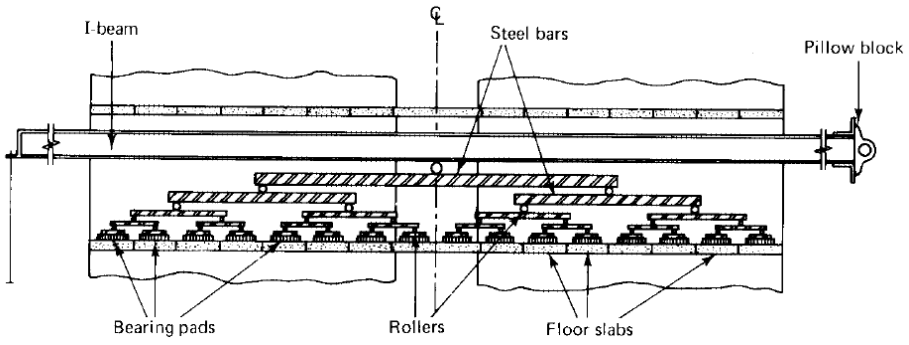

Figure A.1: Whiffle-Tree load system (Harris and Muskivitch, 1980)

Note that the articulated system of the Whiffle-Tree is statically determinate. To apply proportional loading with proportions $(p_1, p_2, p_3, \cdots, p_n)$, where n is the number of the loads, a Whiffle-Tree load system may be designed as follows: first, Loads 1 and 2 are combined with a loading beam at one level below the test structure. At the level below this, another loading beam carries the previously combined Loads of 1 and 2 on one end, and Load 3 on the other

end with a resultant of the sum of the first three loads, as shown in Figure A.2. This procedure can be repeated to include all loads.

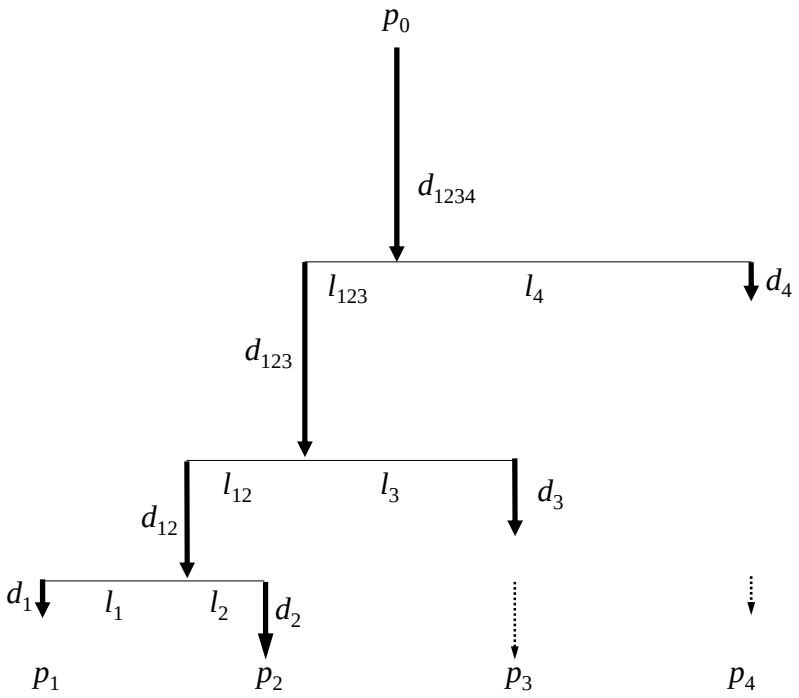

Figure A.2: Articulated system of the Whiffle-Tree

Given that all loading beams are pin-connected, the proportionality of length can be obtained from moment equilibrium:

$$\frac{l_1}{l_2} = \frac{p_2}{p_1}, \quad \frac{l_{12}}{l_3} = \frac{p_3}{p_1 + p_2}, \quad \frac{l_{123}}{l_4} = \frac{p_4}{p_1 + p_2 + p_3} \tag{A.1}$$

The loading beams can be flexible, and as long as the length proportionalities are maintained, the load distribution will be maintained even if the loading beams deform, translate, or rotate. If the loading beams are stiff enough as to be considered rigid, the relations between displacements can be derived.

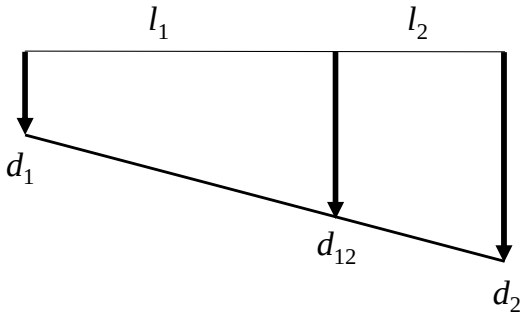

Figure A.3: Interpolation relation for displacements

From Figure A.3 we write

$$\begin{aligned} d_{12} &= \frac{l_2 d_1 + l_1 d_2}{l_1 + l_2} = \frac{p_1 d_1 + p_2 d_2}{p_1 + p_2} \\ d_{123} &= \frac{l_3 d_{12} + l_{12} d_3}{l_{12} + l_3} = \frac{(p_1 + p_2)\, d_{12} + p_3 d_3}{p_1 + p_2 + p_3} = \frac{p_1 d_1 + p_2 d_2 + p_3 d_3}{p_1 + p_2 + p_3} \end{aligned} \tag{A.2}$$

Continuing this derivation reveals that an interesting relation of displacements implied by the Whiffle-Tree System:

$$d_{1234} = \frac{p_1 d_1 + p_2 d_2 + p_3 d_3 + p_4 d_4}{p_1 + p_2 + p_3 + p_4} \tag{A.3}$$

or

$$p_1 d_1 + p_2 d_2 + p_3 d_3 + p_4 d_4 - (p_1 + p_2 + p_3 + p_4)\, d_{1234} = 0 \tag{A.4}$$

A.3 Numerical proportional loading

Suppose a linear multiple point constraint is applied to the original structural system where the proportional loads are applied:

$$\sum (p_i d_i) - \left(\sum p_i\right) d_0 = 0 \tag{A.5}$$

where p_i is proportion of load, d_i is displacement, at the i-th degree-of-freedom, and d_0 is the displacement at the new degree-of-freedom introduced by the multiple point constraint. Displacement d_0 can be considered as a weighted average displacement:

$$d_0 = \frac{\sum (p_i d_i)}{\sum p_i} \tag{A.6}$$

where the weight for d_i is the corresponding load proportion p_i. If this kinetic constraint is satisfied, application of principle-of-virtual-work to the *rigid* constraint will lead to

$$P_0 \ \delta d_0 + \sum (-P_i \ \delta d_i) = 0 \tag{A.7}$$

where P_i's are the proportional loads applied on the original structure by the constraint, and P_0 and $(-P_i)$'s are loads on the constraints corresponding to d_0 and d_i's. Because the constraint is rigid, the right hand side of Equation (A.7) — the internal virtual work — is zero. Because δd_0 and δd_i's are the corresponding virtual displacements, they are also required to satisfy the kinetics constraint in Equation (A.5), *i.e.,*

$$\sum (p_i \ \delta d_i) - \left(\sum p_i\right) \ \delta d_0 = 0 \tag{A.8}$$

Combining Equations (A.7) and (A.8) and eliminating d_0 leads to

$$\sum \left\{ \left[p_i P_0 - \left(\sum p_i\right) P_i \right] \ \delta d_i \right\} = 0 \tag{A.9}$$

The above derivation is true even if the additional degree-of-freedom d_0 is further constrained such that $\delta d_0 = 0$ (*e.g.,* d_0 is under displacement control as a

prescribed time history). As long as all d_i's are at *free* degrees-of-freedom, their variations δd_i's are arbitrary. Thus their coefficients must vanish:

$$p_i P_0 - \left(\sum p_i\right) P_i = 0 \qquad \forall i \tag{A.10}$$

or more usefully

$$(P_1 : P_2 : \cdots : P_n) = (p_1 : p_2 : \cdots : p_n) \qquad \text{if } \sum p_i \neq 0 \tag{A.11}$$

In other words, the constraint $\sum (p_i d_i) - (\sum p_i)\, d_0 = 0$ enforces load proportionality $(P_1 : P_2 : \cdots : P_n) = (p_1 : p_2 : \cdots : p_n)$. The application of the virtual work principle provides an alternative support for the relation found from displacement interpolation in the previous section, *i.e.,* Equation (A.4) for the case of four target degrees-of-freedom. The above derivation proves the validity of the proposed numerical method of applying proportional loads using multiple point constraints. Because the proof relies only on the linearity and rigidity of the constraint and principle of virtual work — but does not depend on the properties of the original system — it can be applied to all linear and nonlinear structures.

A.4 Linear example

Consider a structure consisting of two independent springs with stiffness 1 and 2, respectively. A load pattern of proportionality 2:1 is applied to the

springs. The goal is to evaluate the behavior of the structure. For this simple example, the loading can be directly applied because of linearity, *e.g.,* 4 and 2 (for proportionality $2:1$). When the displacements of 4 and 1 are obtained, the behavior can be evaluated (Figure A.4):

$$P_1 = 1d_1 \quad \text{and} \quad P_2 = 2d_2 \tag{A.12}$$

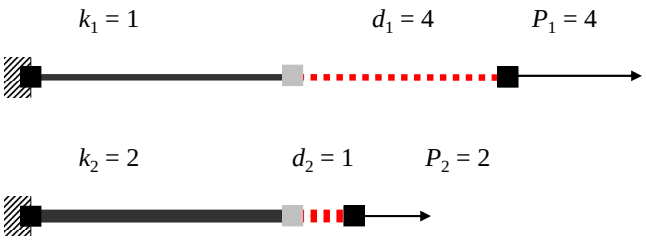

Figure A.4: A linear example

Next, the constraint method developed above is applied. In order to maintain the loading proportionality of $2:1$, or $p_1 = 2$ and $p_2 = 1$, the linear constraint would be:

$$2d_1 + 1d_2 - 3d_0 = 0 \tag{A.13}$$

where again d_0 is displacement at the additional degree-of-freedom introduced by this constraint. As shown in the previous section, application of principle of virtual work to the rigid constraint will lead to

$$P_0\ \delta d_0 - P_1\ \delta d_1 - P_2\ \delta d_2 = 0 \tag{A.14}$$

Virtual displacements δd_0, δd_1 and δd_2 are also required to satisfy the kinetics constraint in Equation (A.13), *i.e.,*

$$2\delta d_1 + 1\delta d_2 - 3\delta d_0 = 0 \tag{A.15}$$

Combining Equations (A.14) and (A.15) and eliminating d_0 leads to

$$(2P_0 - 3P_1)\ \delta d_1 + (P_0 - 3P_2)\ \delta d_2 = 0 \tag{A.16}$$

where d_1 and d_2 are free degrees-of-freedom, so their variation δd_1 and δd_2 are arbitrary. Thus their coefficients must vanish:

$$2P_0 - 3P_1 = P_0 - 3P_2 = 0 \quad \text{or} \quad P_1 : P_2 = 2 : 1 \tag{A.17}$$

The constraint $2d_1 + 1d_2 - 3d_0 = 0$ is rewritten as

$$g(\boldsymbol{d}) = \boldsymbol{Q}\boldsymbol{d} - \bar{\boldsymbol{d}}_g = 0 \tag{A.18}$$

where $\boldsymbol{Q} = \{2 \quad 1\}$, $\boldsymbol{d} = \{d_1 \quad d_2\}^T$, and $\bar{\boldsymbol{d}}_g = 3d_0$. If the Lagrange multiplier method is used, then the general equation to solve the constrained problem is

$$\begin{bmatrix} \boldsymbol{K} & \boldsymbol{Q}^T \\ \boldsymbol{Q} & \boldsymbol{0} \end{bmatrix} \begin{Bmatrix} \boldsymbol{d} \\ \boldsymbol{\lambda} \end{Bmatrix} = \begin{Bmatrix} \boldsymbol{P} \\ \bar{\boldsymbol{d}}_g \end{Bmatrix} \tag{A.19}$$

for the above linear example, this equation becomes

$$\begin{bmatrix} 1 & 0 & 2 \\ 0 & 2 & 1 \\ 2 & 1 & 0 \end{bmatrix} \begin{Bmatrix} d_1 \\ d_2 \\ \lambda \end{Bmatrix} = \begin{Bmatrix} 0 \\ 0 \\ 3d_0 \end{Bmatrix} \tag{A.20}$$

Solving this system of equations with weighted average displacement $d_0 = 3$ [d_0 is introduced in Equation (A.13)] will result in displacements $d_1 = 4$, $d_2 = 1$ and loads $P_1 = 4$, $P_2 = 2$. The loads satisfy proportionality of $2 : 1$.

A.5 Nonlinear softening examples

In this section the multiple point constraint method is demonstrated for two inelastic systems: one consists of nonlinear springs and the other is the biaxial tension of a shell element with nonlinear material response.

A.5.1 Nonlinear springs

Consider a system consisting of three springs, all with a stiffness of 1000 (Figure A.5). Spring 1 and Spring 2 are linear. Spring 3 yields at a strength of 50 and has a post-yield stiffness of -200.

Load proportionality at Springs 1, 2 and 3 are $1 : 2 : 3$. Therefore, the constraint is

$$d_1 + 2d_2 + 3d_3 - 6d_0 = 0 \tag{A.21}$$

where d_0 is time-varying weighted average displacement prescribed as

$$d_0 = t/100 \tag{A.22}$$

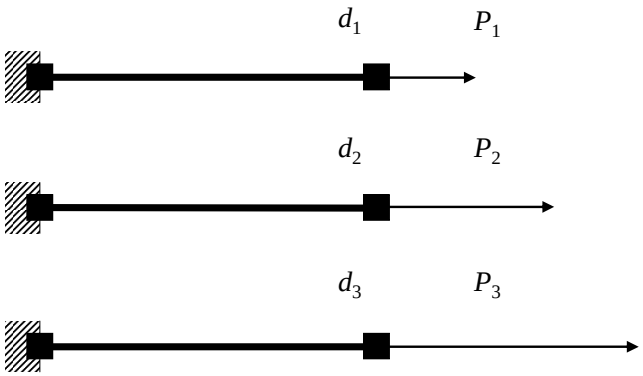

Figure A.5: Nonlinear springs

The system is solved by using LS-DYNA (LSTC, 2007), the constraint is applied using keyword CONSTRAINED_LINEAR_GLOBAL. The results are shown in Figures A.6 to A.8. Figure A.6 shows that Spring 3 yields and softens at about four second, but the other two springs unload elastically. Figure A.7 shows consistent results: d_3 increases and d_1 and d_2 decrease around the same time. The load proportionality $1:2:3$ is kept constant and shown in Figure A.8.

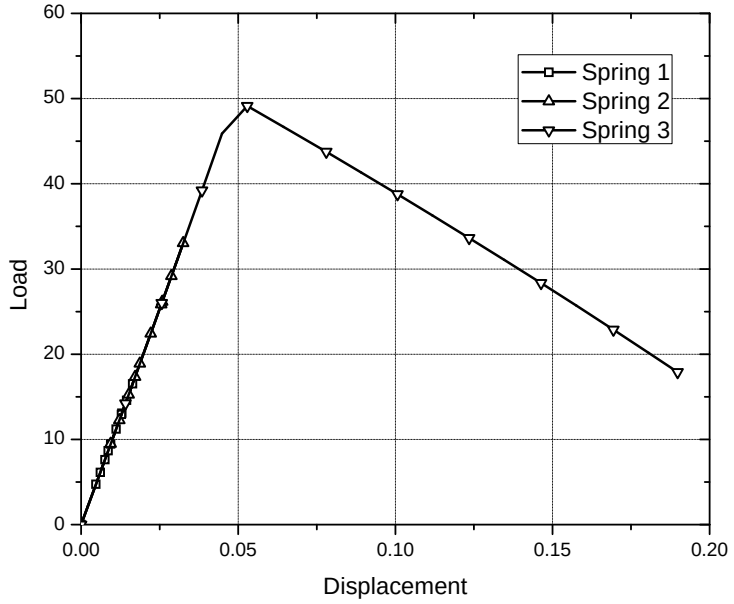

Figure A.6: Load versus displacement for nonlinear springs

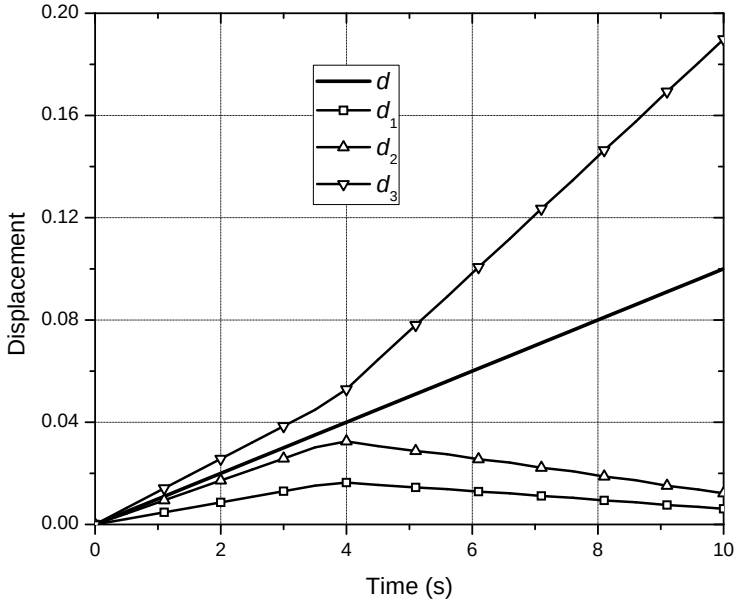

Figure A.7: Displacement histories of nonlinear springs

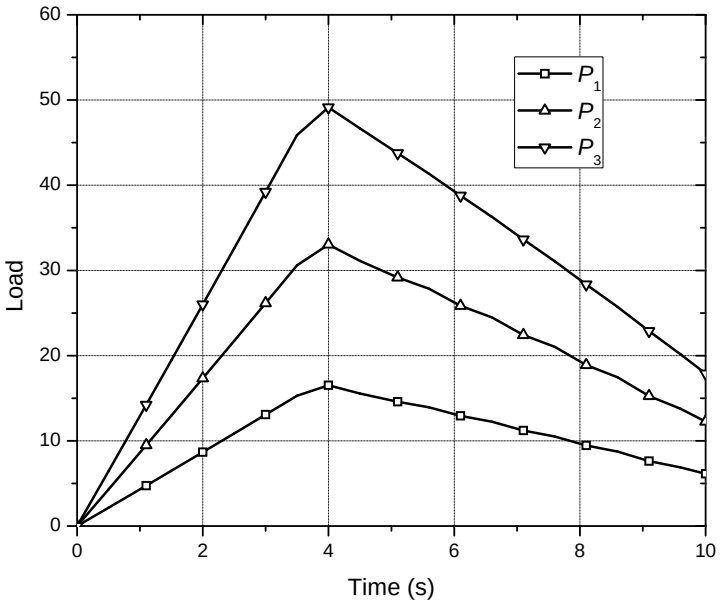

Figure A.8: Load histories of nonlinear springs

A.5.2 Biaxial tension of a shell element with nonlinear material

A single shell element system is subjected to biaxial tension (Figure A.9). The size of the shell element is 1×1, and the thickness is 1. The Young's modulus of the material is $10,000$, and the yield stress and post-yield modulus in uniaxial tension test is 50 and $-2,000$, respectively.

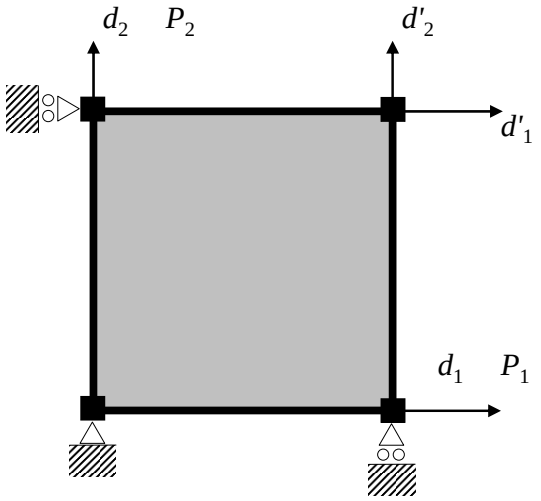

Figure A.9: Biaxial tension of a shell element

The load proportionality specified in the two directions is 2 : 1. When the displacements are small, the stress proportionality is approximately 2 : 1. The constraints are

$$2d_1 + d_2 - 3d_0 = 0 \quad \text{and} \quad d'_1 - d_1 = d'_2 - d_2 = 0 \tag{A.23}$$

or

$$2d_1 + 2d_1' + d_2 + d_2' - 6d_0 = 0 \tag{A.24}$$

where d_0 is the time-varying weighted average displacement prescribed as

$$d_0 = t/10000 \tag{A.25}$$

The system is again solved using LS-DYNA. The results are shown in Figures A.10 and A.11. Figure A.10 shows that ε_{11} increases and ε_{22} decreases after the material yields and softens at around 40 seconds. The approximate stress proportionality $2:1$ is kept constant, as shown in Figure A.11.

A.6 Practical example for pushover analysis

The proposed method applying proportional loads using multiple point constraints is further illustrated with a pushover analysis of a three-story steel braced frame. The prescribed first-mode load distribution is $0.32 : 0.71 : 1.00$ (Table 6.3, Figure A.12). The story shear-roof displacement response for each story solved in LS-DYNA is shown in Figure A.13. The story shear proportionality, $2.03 : 1.71 : 1.00$, is constant and consistent with the applied load distribution before and after the highly nonlinear responses, such as buckling and fracture of the brace, and fracture of the column.

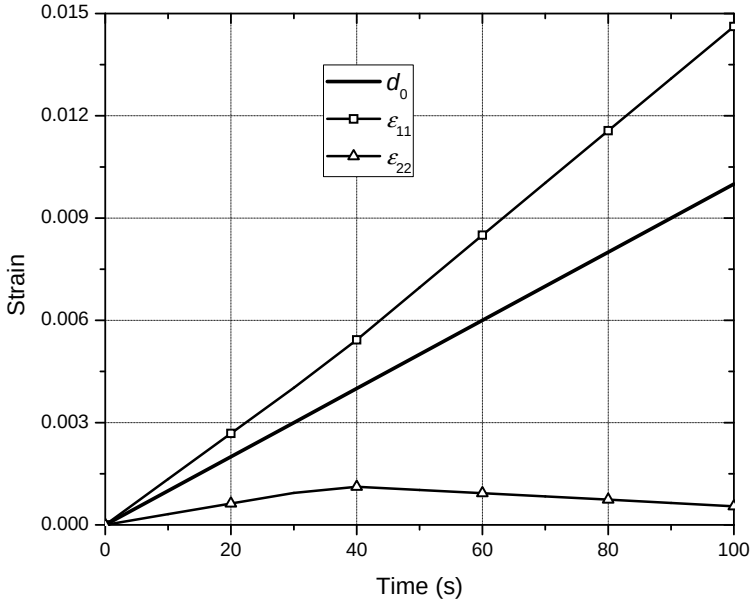

Figure A.10: Strain histories of nonlinear material

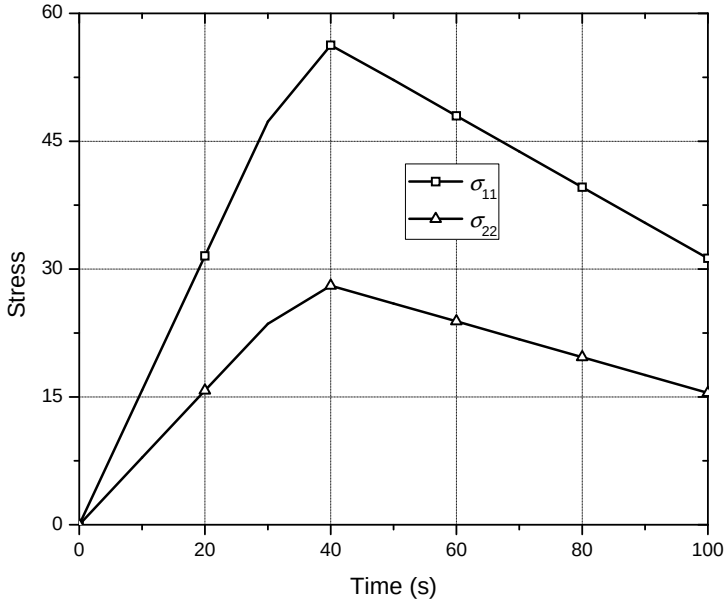

Figure A.11: Stress histories of nonlinear material

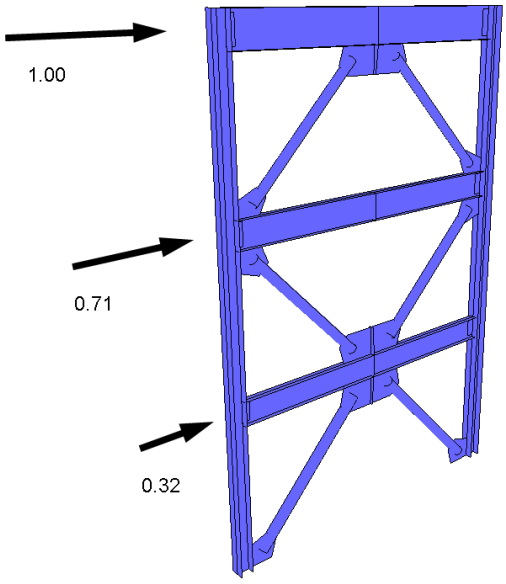

Figure A.12: Pushover analysis model of braced frame

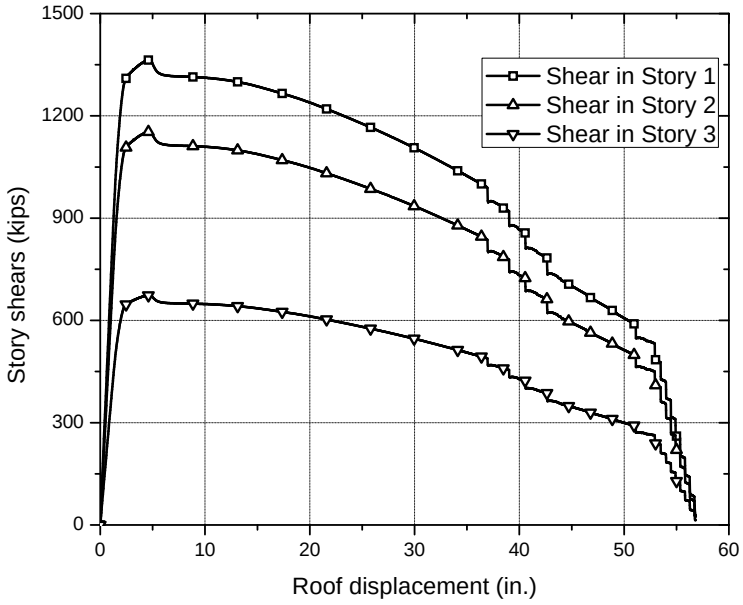

Figure A.13: Story shears versus roof displacement of braced frame

A.7 A special case

Consider the following constraint:

$$\sum (p_i d_i) - c d_0 = 0 \tag{A.26}$$

where c is a non-zero constant. If $\sum (p_i d_i) = 0$, specifically if $\sum p_i = 0$ and the d_i's are identical, then d_0 must be zero. Following the same procedure in Section A.3, it is still possible to prove that the specified load proportions are satisfied. It is valid to apply a load at the degree-of-freedom corresponding to d_0 and maintain load proportionality. However, it is not possible to prescribe a time-varying non-zero displacement at this degree-of-freedom as it will conflict with the constraint. Fortunately, the structural system can be extended by adding another "dummy" degree-of-freedom at which a non-zero stiffness pivot is provided, *e.g.,* a "dummy" linear spring connecting this degree-of-freedom and a fixed degree-of-freedom. The multiple point constraint is then extended to the additional degree-of-freedom such that $\sum (p_i d_i) \neq 0$.

For example, if loads are applied to the two identical springs (Figure A.14) with proportionality $1 : -1$, the linear constraint would be

$$d_1 - d_2 - c d_0 = 0 \tag{A.27}$$

To avoid the singular stiffness when prescribing the displacement at d_0, a "dummy" spring and a "dummy" degree-of-freedom are added at d_3, shown

in Figure A.14. For the new system, the revised constraint is

$$d_1 - d_2 + d_3 - d_0 = 0 \tag{A.28}$$

Then the constraint conflict can be solved.

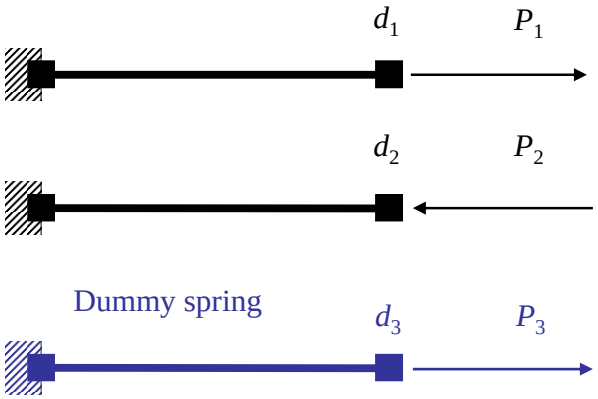

Figure A.14: A two-spring system and a 'dummy' spring

A.8 Concluding remarks

A numerical method for applying proportional loading using multiple point constraints is developed based on the principle of virtual work. It is applicable for an arbitrary number of loads, in arbitrary directions, and for an arbitrary type of structure. Some examples demonstrate the application and accuracy of the multiple point constraint method. This method provides a stable and efficient way to evaluate structures that may undergo softening.

Appendix B

Discussion on Instability of Newmark Integrator

B.1 Introduction

The Newmark integrator (Newmark, 1959) is one of the most popular classes of time integrators. It has been considered unconditionally stable if parameters $\gamma \geq 1/2$ and $\beta \geq \gamma/2$ are used (Hughes, 1987); $\beta = 1/4$ and $\gamma = 1/2$ are the most widely used combination of parameters. However, there is one situation that has been generally ignored: if the mass is zero, and parameters $\beta = 1/4$ and $\gamma = 1/2$ are used, the integrator becomes unstable.

Zero modal mass is not rare in structural dynamic analyses. It is common

to assign zero (distributed) mass density to finite elements but a lumped mass at the nodes. In this case, there is no rotary inertia at the nodes, and modal analysis shows a mode with zero mass. If the whole system is solved without static condensation, the zero-mass mode is excited when force is applied, and instability will occur.

In this chapter, the linear stability of Newmark integrator for zero mass is analyzed, and the instability is demonstrated with a numerical example.

B.2 Linear stability analysis

Consider a linear single-degree-of-freedom mass-damper-spring system, which can be described by equation

$$ma_{i+1} + cv_{i+1} + ku_{i+1} = 0 \tag{B.1}$$

at time t_{i+1}, where m is mass, c is damping coefficient, k is stiffness, a, v and u are acceleration, velocity and displacement, respectively. If a Newmark integrator with parameters $\beta = 1/4$ and $\gamma = 1/2$ is applied, then

$$\begin{cases} u_{i+1} = u_i + v_i h + \dfrac{h^2}{4}\left(a_i + a_{i+1}\right) \\ v_{i+1} = v_i + \dfrac{h}{2}\left(a_i + a_{i+1}\right) \end{cases} \tag{B.2}$$

where h is the integration time step. If a_{i+1} from Equation (B.1) is substituted into (B.2), then

$$\begin{cases} mu_{i+1} = mu_i + mv_i h - \dfrac{h^2}{4}\left(cv_i + ku_i + cv_{i+1} + ku_{i+1}\right) \\ mv_{i+1} = mv_i - \dfrac{h}{2}\left(cv_i + ku_i + cv_{i+1} + ku_{i+1}\right) \end{cases} \tag{B.3}$$

This system of equations can be rearranged into the recursion form

$$\boldsymbol{y}_{i+1} = \boldsymbol{A}\boldsymbol{y}_i \tag{B.4}$$

where vector $\boldsymbol{y} = [u, v]^T$ and $\boldsymbol{A}$ is the amplification matrix

$$\boldsymbol{A} = \frac{1}{4m + 2hc + h^2k} \begin{bmatrix} 4m + 2hc - h^2k & 4hm \\ -4hk & 4m - 2hc - h^2k \end{bmatrix} \tag{B.5}$$

The eigenvalues of the amplification matrix are

$$r = \frac{[4m - h^2k] \pm 2h\sqrt{c^2 - 4mk}}{4m + 2hc + h^2k} \tag{B.6}$$

Linear stability of recursion requires that these eigenvalues lie within the unit circle in the complex plane, and those on the circle have multiplicities of 1 (Iserles, 1996). In other words, if $\|r\| \leq 1$ and those roots with $\|r\| = 1$ are not repeated, then the integrator is stable. If mass is larger than zero $m > 0$ and parameters $\gamma \geq 1/2$ and $\beta \geq \gamma/2$ are used, the integrator is unconditionally stable (Hughes, 1987).

But if mass is zero ($m = 0$), the eigenvalues become

$$r_{1,2} = \frac{-hk \pm 2c}{2c + hk} \qquad \Rightarrow \quad r_1 = -1 \quad \text{and} \quad r_2 = 1 - \frac{2hk}{2c + hk} \tag{B.7}$$

If $c > 0$ and $h > 0$, then $r_2 \in (-1, 1)$, and there is only one eigenvalue $r_1 = -1$ lying on the unit circle. Numerical error will propagate from one step to the next constantly. If the damping coefficient is also zero, $c = 0$, then both eigenvalues become -1. They both lie on the unit circle and the multiplicity is 2. For this case, the Newmark's method becomes unstable. The numerical error will grow linearly (instead of exponentially).

B.3 Demonstration

Figure B.1 shows a system with three nodes connected by two truss elements. Node 1 is fixed. The mass at the Node 3 is 0.001. The stiffness of truss elements is 1. Loads are applied at Node 2 and 3, and $P_2 = P_3 = 0.0016t$, where t is time. The system stiffness and mass matrixes are

$$\boldsymbol{K} = \begin{bmatrix} 1.6 & -0.8 \\ -0.8 & 0.8 \end{bmatrix}, \quad \boldsymbol{M} = \begin{bmatrix} 0 & 0 \\ 0 & 0.001 \end{bmatrix} \tag{B.8}$$

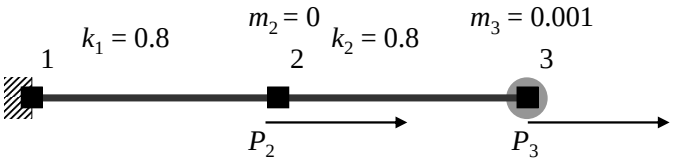

Figure B.1: System for demonstration

For the damped system, stiffness proportional damped is applied using Rayleigh damping $\boldsymbol{c} = a\boldsymbol{M} + b\boldsymbol{K}$, with $a = 0$ and $b = 0.005$. This results

in a damping ratio $\zeta_1 = 5\%$ for the first mode ($\omega_1 = 20$). Modes of the system are $\boldsymbol{\phi}_1 = [0.5, 1]^T$, and $\boldsymbol{\phi}_2 = [1, 0]^T$. Mode 1 has non-zero modal mass ($M_1 = 0.001$), whereas Mode 2 has zero modal mass ($M_2 = 0$). Based on the linear stability analysis in previous section, if the Newmark integrator is used to solve this dynamics system, Mode 1 is stable and Mode 2 is unstable. Because Mode 2 contributes only to the displacement of Node 2 ($\phi_{22} = 0$), Node 3 will be stable and Node 2 will be unstable.

The analytical solution of acceleration for system $m\ddot{q} + c\dot{q} + kq = \alpha t$ is

$$\ddot{q} = \begin{cases} \dfrac{\alpha}{k} \exp -\zeta\omega_n t \dfrac{\omega_n}{\sqrt{1-\zeta^2}} \sin \omega_d t & (m \neq 0) \\ 0 & (m = 0) \end{cases} \tag{B.9}$$

where $\omega_n = \sqrt{k/m}$, $\zeta = c/(2m\omega_n) < 1$ and $\omega_d = \omega_n\sqrt{1-\zeta^2}$. By superposition, the accelerations for undamped system in Figure 2 are

$$\begin{aligned} a_2 &= 0.06 \sin 20t \\ a_3 &= 0.12 \sin 20t \end{aligned} \tag{B.10}$$

and analytical solutions of accelerations for $\zeta = 5\%$ under-damped system are

$$\begin{aligned} a_2 &= \frac{0.06}{\sqrt{0.9975}} \exp(-t) \sin(20\sqrt{0.9975}t) \\ a_3 &= \frac{0.12}{\sqrt{0.9975}} \exp(-t) \sin(20\sqrt{0.9975}t) \end{aligned} \tag{B.11}$$

Figures B.2 and B.3 compare the results for the undamped system. Figures B.2a and B.3a are the analytical solutions; accelerations at Node 2 and 3 are both sinusoidal curve. If zero mass at Node 2 is specified, the error for Mode 2

will grow linearly, shown in Figure B.2b for a time step of 0.005. Figures B.2b and B.3b also show that the instability is at Node 2 only. This is because Mode 2 has no component at Node 3. If a small mass is assigned at Node 2, then as shown in Figure B.2c, the instability is diminished. The oscillation at Node 2 is expected because high-frequency vibration of Mode 2 is not damped out. Figures B.4 and B.5 compare the results for the damped system. Figures B.4a and B.5a show the analytical solution of ever-decreasing oscillation of acceleration at Node 2 and 3. If the mass at Node 2 is zero, the absolute error of Mode 2 will propagate constantly and the numerical solution oscillates about the analytical solution. The numerical result for this case is shown in Figure B.4b. The high-frequency part (Mode 2) of acceleration at Node 2 never decreases, even if its low-frequency part (Mode 1) at Node 2 does because of damping. If a small mass is assigned at Node 2, then the numerical result will quickly converge to the analytical one, as observed in Figure B.4c.

B.4 Discussion

B.4.1 Source of initial numerical error

The truncation error is small for a second order integrator and it decreases with decreasing step sizes. The round-off error is negligible for double precision evaluation. Therefore, they are not the major source of the initial numerical er-

ror that linearly grows, as observed in Figure B.2b, or propagates constantly, as observed in Figure B.4b. One possible source of the major initial numerical error comes from the discrepancy of zero initial velocity in the numerical solution and non-zero initial velocity in analytical solution. For a system with non-singular mass, zero initial velocity is commonly specified as the initial condition. This is compatible with the analytical result. For a mode with zero mass, however, the analytical solution of velocity may be non-zero. If zero initial velocities in numerical solution are still adopted, then there can be an initial numerical error. The error in velocity is amplified when differentiated into acceleration.

B.4.2 Other values of parameter β

If parameters $\gamma = 1/2$, $\beta > \gamma/2$ are used, the eigenvalues of the amplification matrix are

$$r = \frac{2m + (2\beta - 1)h^2k \pm \left[h\sqrt{c^2 - 4mk - (4\beta - 1)h^2k^2}\right]}{2m + hc + 2\beta h^2 k} \tag{B.12}$$

If mass is zero, $m = 0$, the eigenvalues become

$$r_{1,2} = \frac{(2\beta - 1)hk \pm \sqrt{c^2 - (4\beta - 1)h^2k^2}}{2 + 2\beta hk} \tag{B.13}$$

If $c > 0$ and $h > 0$, then the integrator is unconditionally stable, even when $m = 0$. But if $c = 0$, then

$$r_{1,2} = \frac{(2\beta - 1) \pm i\sqrt{4\beta - 1}}{2\beta} \tag{B.14}$$

where i is the imaginary unit. It can be calculated that $\|r\| = 1$, therefore a numerical error will propagate from one step to the next constantly. It is interesting to find that if $\gamma = 1/2$, $\beta > 1/4$, the Newmark integrator is stable even if the mass is zero. The most commonly used parameter set — $\gamma = 1/2$, $\beta = 1/4$ — is, in fact, the worse case if mass is zero. Numerical results for parameters $\gamma = 1/2$, $\beta = 1/4 + 0.01$ are shown in Figures B.6 and B.7. One can observe from the figures that even if the mass is zero at Node 2, the results are stable provided β is strictly larger than $\gamma/2$.

B.5 Concluding remarks

If the mass is zero, the second order equation is infinitely stiff (in fact, it is a first order equation, but is solved as a second order one). Previously it was commonly believed that an implicit numerical integrator was adequate to address this situation and that Newmark integrator is unconditionally stable if parameters $\gamma \geq 1/2$ and $\beta \geq \gamma/2$ are used. This chapter analyzed the linear numerical stability of Newmark integrator, and demonstrated that even if Newmark integrator is implicit, it can be unstable for the case of zero mass. It is better to apply a small amount of mass and/or a small amount of damping to all degrees-of-freedom in a structural system to avoid this instability.

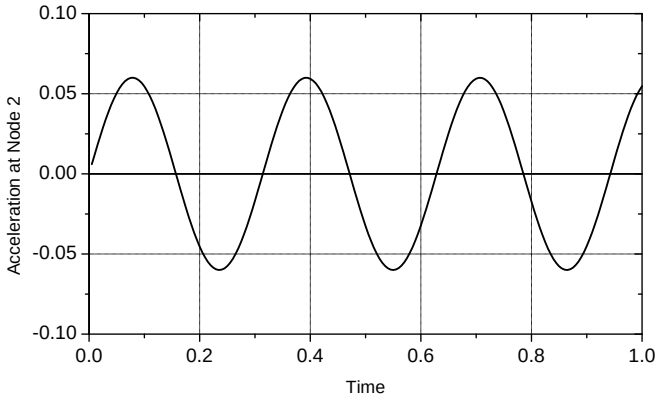

(a) Analytical result

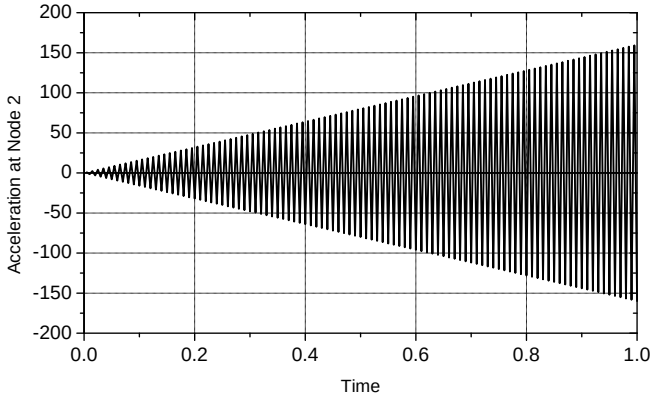

(b) Numerical result, zero mass $m_2 = 0$

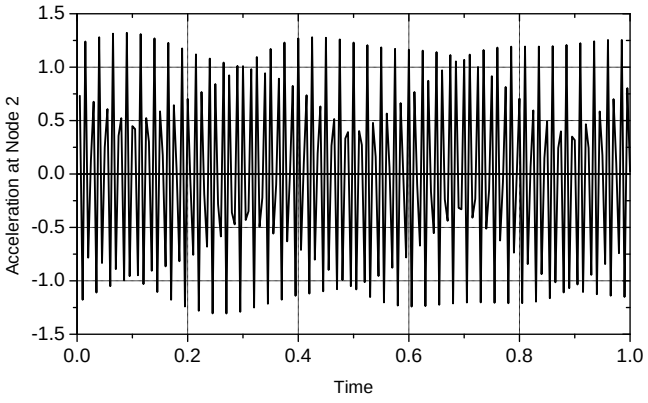

(c) Numerical result, small mass $m_2 = 1 \times 10^{-4}$

Figure B.2: Accelerations at Node 2 (undamped, $\gamma = 1/2$, $\beta = 1/4$)

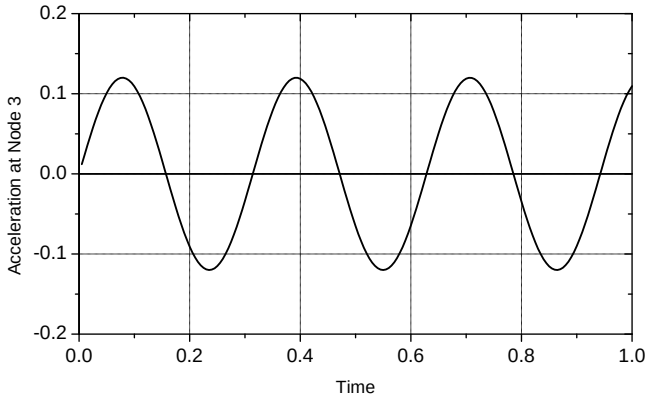

(a) Analytical result

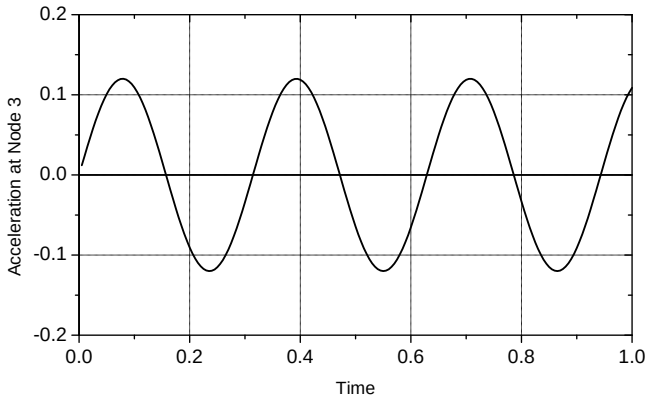

(b) Numerical result, zero mass $m_2 = 0$

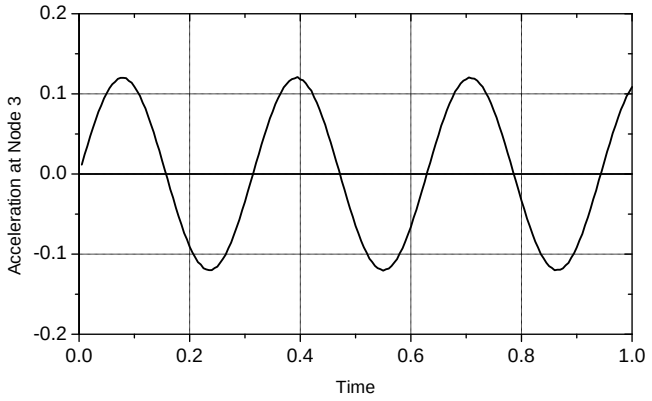

(c) Numerical result, small mass $m_2 = 1 \times 10^{-4}$

Figure B.3: Accelerations at Node 3 (undamped, $\gamma = 1/2$, $\beta = 1/4$)

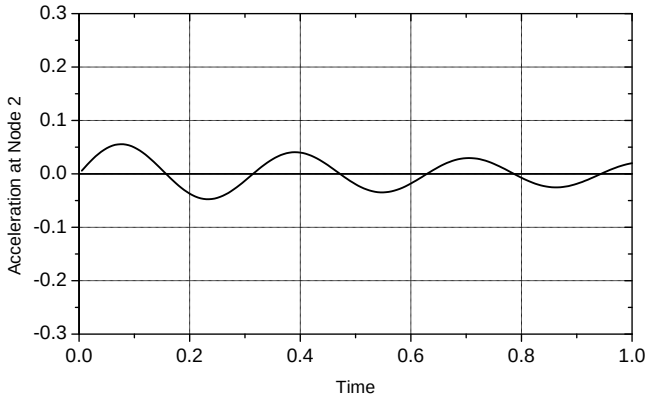

(a) Analytical result

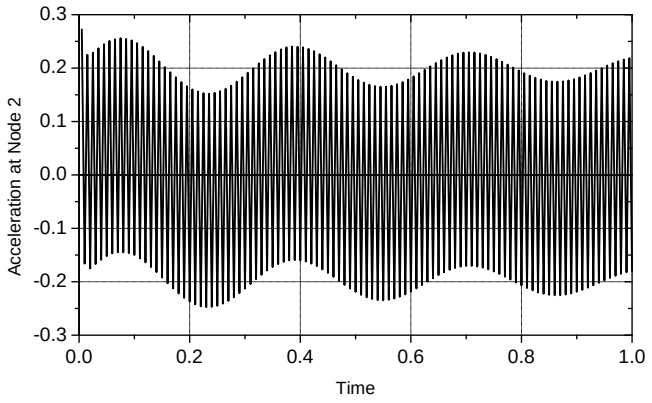

(b) Numerical result, zero mass $m_2 = 0$

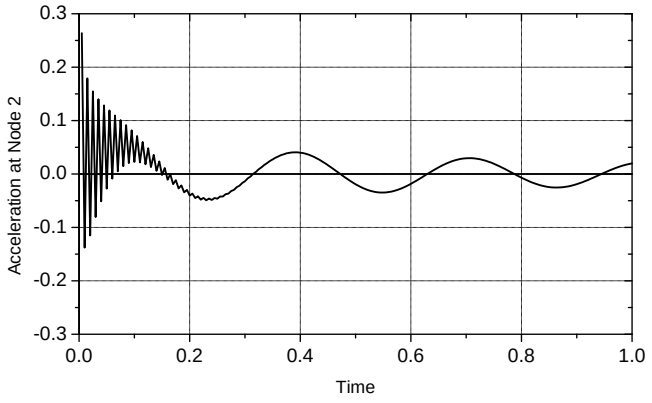

(c) Numerical result, small mass $m_2 = 1 \times 10^{-4}$

Figure B.4: Accelerations at Node 2 (damped, $\gamma = 1/2$, $\beta = 1/4$)

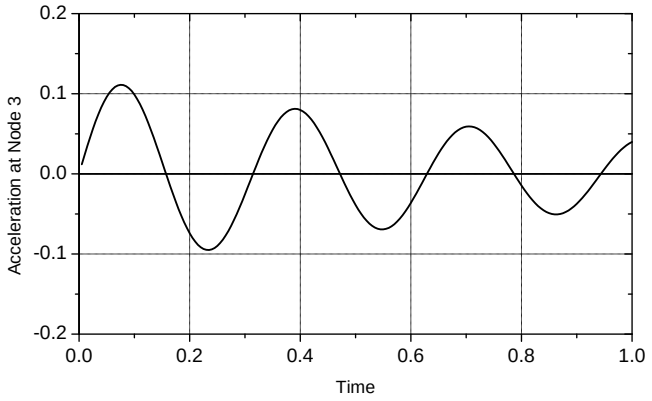

(a) Analytical result

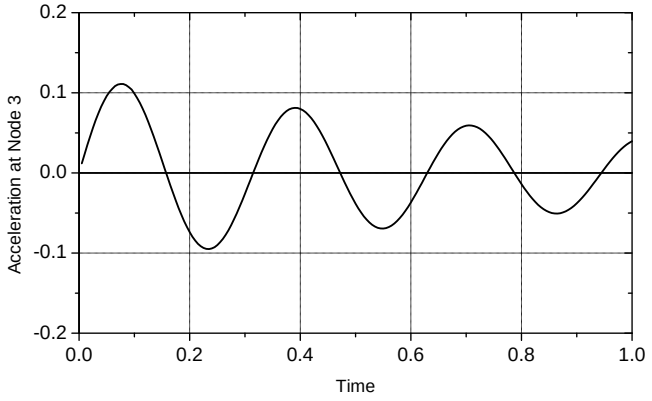

(b) Numerical result, zero mass $m_2 = 0$

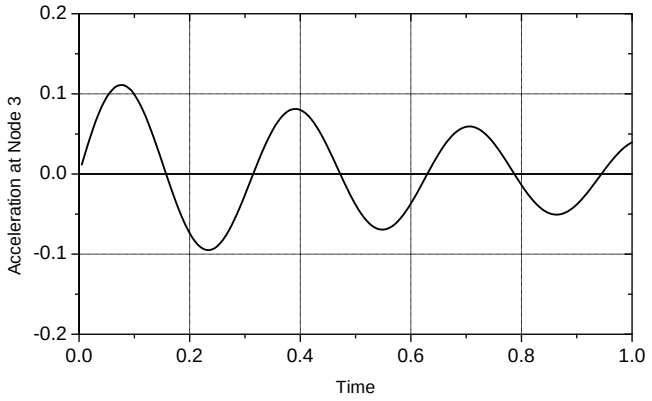

(c) Numerical result, small mass $m_2 = 1 \times 10^{-4}$

Figure B.5: Accelerations at Node 3 (damped, $\gamma = 1/2$, $\beta = 1/4$)

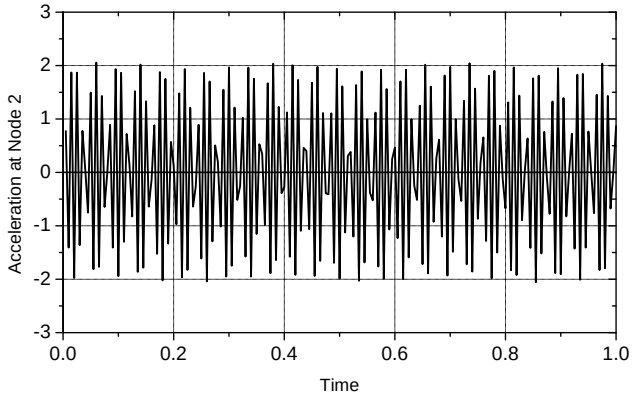

(a) Numerical result, undamped, zero mass $m_2 = 0$

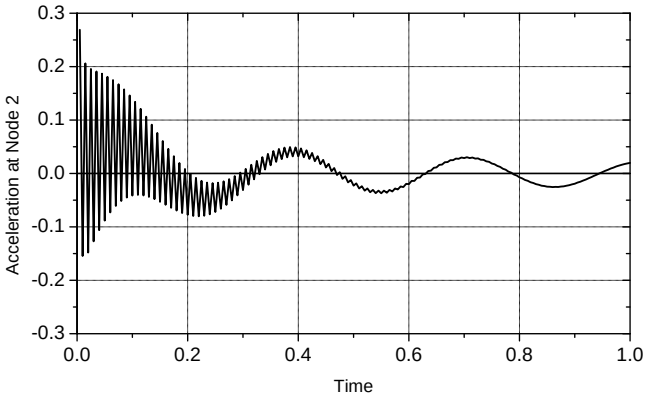

(b) Numerical result, damped, zero mass $m_2 = 0$

Figure B.6: Accelerations at Node 2 ($\gamma = 1/2$, $\beta = 1/4 + 0.01$)

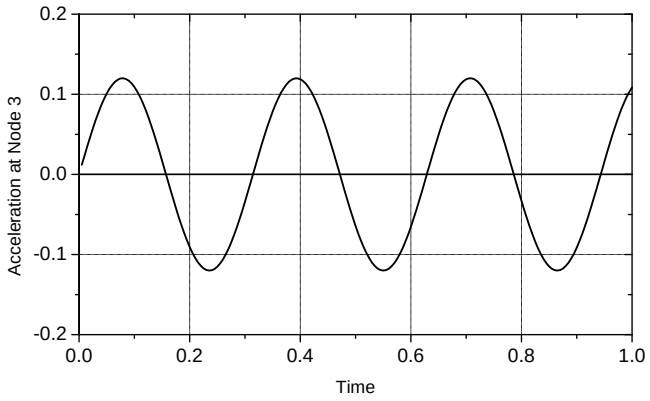

(a) Numerical result, undamped, zero mass $m_2 = 0$

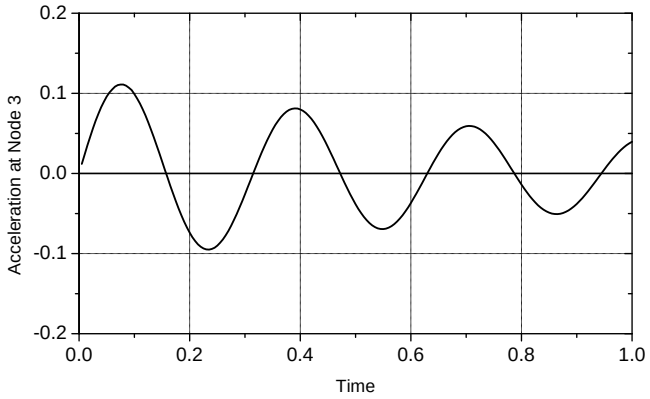

(b) Numerical result, damped, zero mass $m_2 = 0$

Figure B.7: Accelerations at Node 3 ($\gamma = 1/2$, $\beta = 1/4 + 0.01$)